Copyright
by
Anum Ali
2019

The Dissertation Committee for Anum Ali
certifies that this is the approved version of the following dissertation:

Millimeter Wave Link Configuration Using Out-Of-Band Information

Committee:

Nuria González-Prelcic, Supervisor

Robert W. Heath Jr., Co-Supervisor

Elisabeth de Carvalho

Gustavo de Veciana

Haris Vikalo

Millimeter Wave Link Configuration Using Out-Of-Band Information

by

Anum Ali

DISSERTATION

Presented to the Faculty of the Graduate School of

The University of Texas at Austin

in Partial Fulfillment

of the Requirements

for the Degree of

DOCTOR OF PHILOSOPHY

THE UNIVERSITY OF TEXAS AT AUSTIN

December 2019

Dedicated to my parents Chaudry Ghulam Ali and Gulzar Begum.

Acknowledgments

I am truly grateful to Allah subhanahu-wa-taala for enabling me to complete this work.

I am grateful to the faculty of COMSATS University Islamabad (CUI) and King Fahd University of Petroleum and Minerals (KFUPM) for providing me a strong education. I am particularly thankful to Prof. Shafayat Abrar (at CUI) for starting my research journey. At KFUPM, I was lucky to work with Prof. Tareq Y. Al-Naffouri. My learnings from Prof. Al-Naffouri have played a decisive role in my success as a Ph.D. student.

During my Ph.D. studies, I was co-supervised by Prof. Nuria González-Prelcic and Prof. Robert W. Heath Jr. I am thankful to my advisors for accepting me in WSIL, supporting my Ph.D., and providing insightful feedback on the drafts of research articles. I am also thankful to my advisors for trusting me as a mentor for junior students in WSIL. The unrelenting pursuit of excellence by Prof. González-Prelcic and Prof. Heath in all areas pertaining to academic research is exemplary. I am also thankful to my dissertation committee members Prof. Gustavo de Veciana, Prof. Haris Vikalo, and Prof. Elisabeth de Carvalho for providing valuable feedback on my work.

I am thankful to the council I received (and continue to receive) from former WSIL members Ahmed Alkhateeb, Jianhua Mo, Kiran Venugopal, Mo-

hammed Eltayeb, Amine Mezghani, Sungwoo Park, Dalin Zhu, Talha Ahmed Khan, and Vutha Va. Some WSIL members thought it possible to put up with me outside the lab. Among these are Preeti Kumari, Rebal Jurdi, Yuyang Wang, Megha Parhi, Khurram Mazher, and Nitin Myers. The non-WSIL folk who considered my company bearable include Isfar Tariq, Srilakshmi Pattabiraman, Ahmad AlAmmouri, Rahi Kalantari, Manan Gupta, and Roohollah Amiri. My Ph.D. journey was also colored by the internships that I had at Intel, Qualcomm, Nokia Bell Labs, and Aalborg University. I found admirable mentors and memorable friendships in these internships. I am thankful to all that I learned from and shared a laugh with.

Finally, I am thankful to my family for their sacrifices and unconditional love. Specifically, I am thankful to my father Chaudry Ghulam Ali and mother Gulzar Begum for showing me a simple way of life by their contentment with few things and few deeds. I am thankful to my sisters Benish and Farzana for our lighthearted weekly discussions on inconsequential matters.

Millimeter Wave Link Configuration Using Out-Of-Band Information

Publication No. _____

Anum Ali, Ph.D.
The University of Texas at Austin, 2019

Supervisor: Nuria González-Prelcic
Co-Supervisor: Robert W. Heath Jr.

Millimeter wave (mmWave) communication is one feasible solution for high data-rate applications like vehicular-to-everything (V2X) communication and next-generation cellular communication. Configuring mmWave links, which can be done through channel estimation or beam-selection, however, is a source of significant overhead. Typically some structure in the channel is exploited (for beam-selection or channel estimation) to reduce training overhead. In this dissertation, we use side-information coming from some frequency band other than the mmWave communication band to reduce the mmWave training overhead. We call such side-information *out-of-band* information. We use the out-of-band information coming from (i) lower frequency (i.e., sub-6 GHz) communication channels, and (ii) mmWave radar. Sub-6 GHz frequencies are a feasible out-of-band information source as mmWave systems are deployed with low-frequency systems (for control signaling or multi-band communication). Similarly, radar is a feasible out-of-band information source as future

vehicles and road-side units (RSUs) will likely have automotive radars. We outline strategies to incorporate sub-6 GHz information in mmWave systems - through beam-selection and covariance estimation - while considering the practical constraints on the hardware of mmWave systems (e.g., analog-only or hybrid analog/digital architecture). We also use a passive radar receiver at the RSU to reduce the training overhead of establishing an mmWave communication link. Specifically, the passive radar taps the transmissions from the automotive radars of the vehicles on road. The spatial covariance of the received radar signals is, in turn, used to establish the communication link. The results show that out-of-band information from sub-6 GHz channels and radar reduces the training overhead of mmWave link configuration considerably, and makes mmWave communication feasible in highly dynamic environments.

Table of Contents

Acknowledgments **v**

Abstract **vii**

List of Tables **xiii**

List of Figures **xiv**

Chapter 1. Introduction **1**

1.1 Applications of millimeter wave communication 1
1.2 Challenges in millimeter wave link configuration 3
1.3 Out-of-band information for millimeter wave link configuration 4
1.4 Thesis statement and summary of contributions 6
1.5 Organization 12
1.6 Abbreviations 13
1.7 Notation 15

Chapter 2. Millimeter Wave Beam-Selection Using Sub-6 GHz Information **17**

2.1 Motivation and prior work 18
2.2 Contributions 23
2.3 System and channel model 24
2.3.1 Millimeter wave system and channel model 25
2.3.2 Sub-6 GHz system and channel model 28
2.4 Problem Formulation 28
2.4.1 Beam codebook design 29
2.4.2 Exhaustive beam-selection 31
2.4.3 Sparsity in beam-selection 33
2.4.4 Compressed beam-selection 34

2.4.5 Leveraging data from all active subcarriers 36
2.5 Out-of-band aided compressed beam-selection 37
2.5.1 First stage (spatial information retrieval from sub-6 GHz) 37
2.5.2 Second stage (out-of-band aided compressed beam-selection) 40
2.6 Multi-band channel characteristics and simulation 43
2.6.1 Review of multi-band channel characteristics 44
2.6.2 Simulation of multi-band frequency dependent channels 46
2.6.2.1 First Stage 48
2.6.2.2 Second Stage 51
2.7 Simulation Results 52
2.7.1 Channel simulation 52
2.7.2 Out-of-band aided compressed beam-selection 53
2.8 Conclusion 64

Chapter 3. Millimeter Wave Covariance Estimation Using Sub-6 GHz Information 66

3.1 Motivation and prior work 67
3.2 Contributions 70
3.3 System, channel and, covariance models 72
3.3.1 Millimeter wave system model 72
3.3.2 Sub-6 GHz system model 74
3.3.3 Channel model 74
3.3.4 Covariance model 76
3.4 Out-of-band covariance translation 77
3.4.0.1 Estimating the number of clusters 80
3.4.0.2 Estimating angle-of-arrival and angle spread . . 81
3.4.0.3 Estimating the power contribution of each cluster 81
3.4.0.4 Obtaining the mmWave covariance 82
3.5 Out-of-band aided compressed covariance estimation 83
3.5.1 Problem formulation 84
3.5.2 Weighted compressed covariance estimation 88
3.6 SNR degradation due to covariance mismatch 90
3.7 Simulation results 94

3.8 Comparison of proposed covariance estimation strategies . . . 106
3.8.1 Computational complexity . . . 106
3.8.2 Overhead . . . 107
3.8.3 Robustness to erroneous information . . . 107
3.8.4 Inherent limitations . . . 108
3.8.5 Favorable operating conditions . . . 108
3.9 Conclusion . . . 109

Chapter 4. Millimeter Wave Link Configuration Using Radar Information 110
4.1 Motivation and prior work . . . 111
4.2 Contributions . . . 114
4.3 V2I communication setup . . . 116
4.4 Communication system model . . . 116
4.4.1 Channel model . . . 119
4.4.2 Covariance model . . . 120
4.5 Radar system model . . . 120
4.6 Proposed radar receiver . . . 124
4.7 Radar bias correction . . . 126
4.8 Similarity metric to measure spatial congruence . . . 130
4.9 Simulation results . . . 135
4.10 Conclusion . . . 147

Chapter 5. Conclusion 150
5.1 Summary . . . 151
5.2 Future Research Directions . . . 153
5.2.1 Experimental verification of the proposed strategies . . . 153
5.2.2 Extension to low resolution ADC based architectures . . . 155
5.2.3 Extension to multiuser scenario . . . 156
5.2.4 Extension to other array geometries . . . 156
5.2.5 Extension to other frameworks . . . 157

Appendix 159

Bibliography **166**

Vita **191**

List of Tables

3.1 Theoretical expressions for covariance $[\mathbf{R}]_{i,j}$ 79
3.2 Simulation Parameters 96

List of Figures

2.1 An elementary use case for sub-6 GHz information in mmWave beam-selection. 20

2.2 A multi-band MIMO system with co-located sub-6 GHz and mmWave antenna arrays. The sub-6 GHz channel is $\underline{\mathbf{H}}$ and the mmWave channel is $\mathbf{H}$. 25

2.3 A mmWave system with phase-shifters based analog beamforming. 25

2.4 A sub-6 GHz system with digital precoding. 28

2.5 The codebook based on sampled array response vectors and its approximation using 2-bit phase-shifters. 30

2.6 The metric $\frac{\|\mathbf{W}\mathbf{W}^{*}-\mathbf{I}\|_{\mathrm{F}}^{2}}{\|\mathbf{W}\mathbf{W}^{*}\|_{\mathrm{F}}^{2}}$ for different phase-shifter bit-resolution and number of antennas M_{TX}. 32

2.7 The matrix $|\mathbf{E}[k]|$ for a 64×16 MIMO system and a single cluster channel with angles $\theta = \phi = 0$ and arrival and departure spread of 2° 34

2.8 The 64x16 matrix $|\hat{\underline{\mathbf{E}}}|$ for an 8x2 MIMO channel. The channel has a single cluster channel with angles $\theta = \phi = 0$ and arrival and departure spread of 2°. 39

2.9 The mutual coherence χ of sensing matrices based on random codebooks and structured-random codebooks. 43

2.10 An example realization generated using the proposed channel generation strategy. 54

2.11 Effective rate of the structured LW-OMP approach versus the number of measurements $N_{\mathrm{RX}} \times N_{\mathrm{TX}}$ with 60 m TX-RX separation and $T_{\mathrm{c}} = 128(M_{\mathrm{RX}} \times M_{\mathrm{TX}})$ blocks. 57

2.12 Effective rate of the structured LW-OMP approach versus the number of measurements $N_{\mathrm{RX}} \times N_{\mathrm{TX}}$ with 60 m TX-RX separation and three different channel coherence times T_{c}. 59

2.13 Success percentage of the structured LW-OMP approach versus the number of measurements $N_{\mathrm{RX}} \times N_{\mathrm{TX}}$ with 60 m TX-RX separation. 60

2.14 Modification of the proposed channel generating strategy to generate a time evolution of the mmWave channel. The main idea is to generate two independent channels and considering them to be independent realizations of the mmWave channel at time t_0 and time t_1. Then the channels between t_0 and t_1 are generated via linear interpolation of the channels at time t_0 and t_1. 62

2.15 The effective rate of the structured LW-SOMP approach versus the time t. The time t here represents the time at which the channel state was observed and used as side information. The TX-RX separation is 60 m. 62

2.16 Effective rate of the structured LW-SOMP approach versus the number of measurements $N_{\mathrm{RX}} \times N_{\mathrm{TX}}$ with 60 m TX-RX separation and $T_{\mathrm{c}} = 32(M_{\mathrm{RX}} \times M_{\mathrm{TX}})$ blocks. 63

2.17 Delay of the proposed strategy in comparison with exhaustive search assuming 4 µs symbol duration for the mmWave symbol and 66 µs symbol duration for the sub-6 GHz symbol. 64

3.1 The multi-band MIMO system with co-located sub-6 GHz and mmWave antenna arrays. The sub-6 GHz channel is denoted $\underline{\mathbf{H}}$ and the mmWave channel is denoted $\mathbf{H}$. 72

3.2 The mmWave system with hybrid analog-digital precoding. . . 74

3.3 The sub-6 GHz system with digital precoding. 75

3.4 The estimated number of clusters $\hat{C}$ (in a two-cluster channel) versus the mean AoA separation (°) of the proposed covariance translation strategy. The mean AoA of the first cluster is 5° and the mean AoA of the second cluster is varied from 5° to 20°. The TX-RX distance is 90 m. The algorithm successfully estimates 2 clusters when the mean AoA separation is greater than 7°. 98

3.5 The efficiency metric η (in a two-cluster channel) versus the mean AoA separation (°) of the proposed covariance translation strategy. The mean AoA of the first cluster is 5° and the mean AoA of the second cluster is varied from 5° to 20°. The TX-RX distance is 90 m. The efficiency is high when the algorithm at low (high) mean AoA separations as the algorithm successfully estimates 1 (2) clusters. 98

3.6 The efficiency metric η (in a two-cluster channel) of the the proposed LW-DCOMP algorithm versus the TX-RX distance (m). First cluster has mean AoA 5° and the second cluster has a mean AoA 45°. The number of snapshots T is 30. The out-of-band aided LW-DCOMP approach performs better at large TX-RX distances. 99

3.7 The effective achievable rate of the proposed covariance estimation strategies versus the TX-RX distance. The rate calculations are based on $T_{\text{stat}} = 2048$ blocks and $T_{\text{train}} = 120$ blocks. The benefit of out-of-band information becomes more pronounced at high TX-RX distances. 101

3.8 The effective achievable rate of LW-DCOMP and DCOMP versus the number of snapshots T (at the transmitter and the receiver). The effective rate is plotted for three values of T_{stat}. The TX-RX distance is fixed at 70 m. The LW-DCOMP reduces the training overhead of DCOMP by over 3x. 102

3.9 The comparative rate of (i) Full instantaneous CSI, (ii) Full statistical CSI and partial instantaneous CSI, and (iii) Statistical CSI only. The number of RF-chains is $M_{\text{RX}} = 8$ and $M_{\text{TX}} = 4$ and the number of streams is $N_{\text{s}} = 4$. The number of subcarriers is $K = 16$, and the TX-RX distance is fixed at 70 m. . 105

3.10 The upper bound on the SNR loss γ with complex Normal perturbation. The number of RF-chains is $M_{\text{TX}} = M_{\text{RX}} = \sqrt{N_{\text{TX}}} = \sqrt{N_{\text{RX}}}$ and $\text{SNR}_{\text{k}} = \frac{\text{P}}{\sigma^2_{\mathbf{n}}\text{K}}$. The upper-bound derived in the analysis holds for both the tested scenarios. 106

4.1 The V2I communication setup with the RSU equipped with a communication and a radar array. 117

4.2 The ego-vehicle with multiple communication arrays and multiple radars. 117

4.3 The mmWave communication system with hybrid analog-digital precoding and combining. 118

4.4 The FMCW radar system with multiple antennas at the receiver. 122

4.5 The covariance correction strategy that (i) resamples the covariance vector magnitude, (ii) unwraps and resamples the phase of the covariance vector, and (iii) uses Toeplitz completion of the resampled covariance vector to obtain the corrected covariance. 129

4.6 Over the air azimuth power spectra and observed power spectra through arrays of 4 antenna elements and 32 antenna elements. 130

4.7 Intuitive explanation of the similarity metric (4.21). The denominator is the sum of a few strongest component of APS2, whereas the numerator is the sum of a few components of APS2, corresponding to the strongest components of APS1. 133

4.8 The ray-tracing setup simulation in Wireless Insite with buildings of various heights, the RSU, and vehicles dropped in four lanes on the road. 139

4.9 The similarity metric S and RPE as a function of the number of antennas N for $N_{\mathrm{s}} = 1$. The results are for a simplified case where the radar and communication arrays are collocated at the RSU and the vehicle and both systems operate on the same frequency. 141

4.10 The similarity metric S and RPE as a function of the number of antennas N for $N_{\mathrm{s}} = 4$. The results are for a simplified case where the radar and communication arrays are collocated at the RSU and the vehicle and both systems operate on the same frequency. 141

4.11 The similarity metric S and RPE as a function of the number of antennas N for $N_{\mathrm{s}} = 1$ and $N_{\mathrm{s}} = 4$. The results show that the similarity decreases with N and increases with N_{s}, and further similarity and RPE follow the same trend. 142

4.12 Rate versus the number of beams for $T_{\mathrm{coh.}} \to \infty$. The proposed radar-assisted strategy achieves the rate of exhaustive-search with fewer measurements, whereas the location-assisted strategy fails to reach the rate of exhaustive search. 146

4.13 Rate versus the number of beams for $T_{\mathrm{coh.}} = 4N_{\mathrm{RSU}}N_{\mathrm{V}}$. The low training overhead radar-assisted and location-assisted strategies have a better rate than the exhaustive-search strategy. 146

4.14 Rate versus the number of beams for $T_{\mathrm{coh.}} \to \infty$ in NLOS channel. The proposed radar-assisted strategy achieves the rate of exhaustive-search with fewer measurements, whereas the location-assisted strategy fails to reach the rate of exhaustive search. 148

4.15 Rate versus the number of beams for $T_{\mathrm{coh.}} = 4N_{\mathrm{RSU}}N_{\mathrm{V}}$. The radar-assisted strategy achieves a rate better than the location-assisted strategy and exhaustive-search with only 30 measurements, implying a 77% overhead reduction. 148

Chapter 1

Introduction

In this chapter, we provide the background and motivation of this dissertation. Specifically, we start by highlighting the applications of millimeter wave (mmWave) communication in Section 1.1 and the challenges in mmWave link configuration in Section 1.2. Then we highlight the potential of using out-of-band information for mmWave link configuration in Section 1.3. We follow this with the thesis statement and a summary of contributions in Section 1.4. Then, we outline the organization of this dissertation in Section 1.5. Finally, we provide the abbreviations (and notations) used throughout the dissertation in Section 1.6 (and Section 1.7).

1.1 Applications of millimeter wave communication

Owing to the large bandwidth, mmWave specturm (i.e., 30-300 GHz) is suitable for gigabit-per-second data-rate communication [1, 2, 3, 4, 5]. Therefore mmWave spectrum has been used for developing gigabit-per-second Wi-Fi through IEEE802.11ad [6]. Furthermore, operation at mmWaves has been a key feature in the development of the fifth generation of cellular communication i.e., 5G new radio (NR).

MmWave communication systems use large antenna arrays and directional beamforming/precoding to provide sufficient link margin [1, 2]. Large arrays are feasible at mmWave as antennas can be packed into small form factors. This enables mmWaves to be used in applications where the size and weight of the radio frequency stage is a limiting factor, e.g., wearable networks [7], mobile devices, and virtual reality devices [8]. Large arrays enable highly directional transmission and reception, which reduces the amount of interference in the mmWave communication systems. This results in an additional gain in data rate. Further, better spectrum sharing between cellular operators is possible using mmWave communications. It has been shown that by using narrow beams and sharing mmWave spectrum the per-user data rate increases, even without coordination between operators [9].

In the context of vehicle-to-everything (V2X) communication, next-generation vehicles will be equipped with several sensors including radars, lidars, cameras, and ultrasonic sensors [10]. The data generated by these sensors may be shared among vehicles and infrastructure, e.g., for cooperative perception [11]. Current communication mechanisms based on sub-6 GHz frequencies (i.e., DSRC [12, 13, 14] or LTE-V2X [15, 16]) do not support the rate required for this data exchange. MmWave V2X communication systems can potentially support the required data-rate owing to the large bandwidth.

1.2 Challenges in millimeter wave link configuration

The large antenna arrays at mmWave need to be properly configured (i.e., link configuration) to provide sufficient link margin [17]. Analog architecture (where a single RF-chain is connected to all antenna elements and the phases of the elements are controlled using phase-shifters) is one suitable architecture for large antenna systems. For such analog systems, link configuration entails the process of finding the best transmit and receive beam. The best transmit and receive beams are decided by following a closed-loop beam-training strategy based on searching over a codebook at the transmitter and receiver. For hybrid analog/digital systems, link configuration is the process of finding the MIMO precoder/combiner based on either instantaneous channel state information (CSI) [18] or statistical CSI [19]. Obtaining channel information at mmWave is, however, challenging due to: (i) the large dimension of the arrays used at mmWave, (ii) the hardware constraints (e.g., a limited number of RF-chains [18, 19]), and (iii) low pre-beamforming signal-to-noise ratio (SNR). The reasons for low pre-beamforming SNR at mmWave are twofold: (i) the antenna size is small which in turn means less received power, and (ii) the thermal noise is high due to large bandwidth. Several approaches have been proposed to rapidly establish mmWave links [20, 21, 22, 23, 24]. The usual strategy is to exploit some sort of structure in the unknown channel that aids in link establishment, e.g., sparsity [20, 21, 25, 26, 27, 28] or channel dynamics [22].

1.3 Out-of-band information for millimeter wave link configuration

One way to reduce the array configuration overhead is to exploit side-information about the mmWave channel. In this dissertation, we use the side-information coming from a frequency band outside the communication band, and call such side-information out-of-band information. Using out-of-band information can positively impact several applications of mmWave communications.

The use of sub-6 GHz information for mmWave is enticing as mmWave systems will likely be used in conjunction with sub-6 GHz systems for multi-band communications and/or to provide wide area control signals [29, 30, 31]. In mmWave cellular [1, 4], the base-station user-equipment separation can be large (e.g., on cell edges). In such scenarios, link configuration is challenging due to poor pre-beamforming SNR and user mobility. The pre-beamforming SNR is more favorable at sub-6 GHz due to lower bandwidth. Therefore, reliable out-of-band information from sub-6 GHz can be used to aid the mmWave link establishment. Similarly, frequent reconfiguration will be required in highly dynamic channels experienced in mmWave vehicular communications (see e.g., [10] and the references therein). The out-of-band information (coming e.g., from dedicated short-range communication (DSRC) channels [13]) can play an important role in unlocking the potential of mmWave vehicular communications.

The are, however, multiple challenges with using sub-6 GHz informa-

tion for mmWave. First sub-6 GHz systems typically have a small number of antennas, whereas mmWave systems have a large number of antennas. This implies that the resolution of the spatial information retrieved from sub-6 GHz is lower compared to the spatial resolution of the mmWave channel. Second, due to a large frequency separation between sub-6 GHz and mmWave, sub-6 GHz and mmWave channels do not have exactly the same spatial characteristics (i.e., some clusters may appear at sub-6 GHz and not and mmWave and vice versa).

Radar is another potential out-of-band information source for mmWave link configuration. Using radar information in mmWave V2I links is feasible, as the future vehicles and road-side-units (RSUs) are likely to be equipped with automotive radars [10]. The radar could provide location information of the vehicle. In line-of-sight (LOS) V2I communication links, the location of the vehicle can be used to reduce the beam training overhead [32, 33]. Raw radar information about the environment is also useful. As the communication channel also stems from the same environment, radar information can be used in mmWave communication link configuration. The main idea of using radar information for mmWave link configuration hinges on the assumption that the azimuth power spectrum (APS) of the communication channel and the radar angular information is correlated. This was initially verified using ray-tracing simulations in [34]. Further, note that blockage is a serious issue in mmWave links [35]. In [36], it was shown that radar information can be used for blockage prediction in LOS mmWave links.

There are also challenges in using radar information for mmWave. First, the mmWave radar band (e.g., 76 GHz) is different from the mmWave communication band (e.g., 73 GHz). Therefore some difference is expected in the spatial properties of radar and communication channel. Second, if the spatial information is to be estimated using a passive radar, the main challenge is the lack of waveform knowledge at the radar receiver. Third, angle estimation using frequency modulated continuous wave (FMCW) radar has a bias [37]. This implies that the spatial information retrieved from radar may not be directly usable for mmWave communication without correcting the bias.

1.4 Thesis statement and summary of contributions

The thesis statement of this dissertation is

> *Out-of-band aided mmWave link configuration has a low training overhead in comparison with in-band only link configuration.*

In this dissertation, we use the out-of-band information to reduce the overhead of establishing a mmWave link.

First, we consider the problem of finding the optimal transmit/receive beam-pair for analog mmWave systems using sub-6 GHz information. We formulate the compressed beam-selection problem, outline a strategy to extract spatial information from sub-6 GHz channel, and use weighted sparse signal recovery [38] to leverage sub-6 GHz information in compressed beam-selection. We also propose a structured random codebook design for compressed beam-

selection based on sub-6 GHz information. The proposed design enforces the training precoder/combiner patterns to have high gains in the strong channel directions. We also outline a multi-frequency channel model to generate channels that are consistent with frequency-dependent channel behavior observed in prior work. Using this channel model for simulations, we show that the proposed approach can reduce the training overhead of beam-selection considerably.

Second, we propose a two mmWave covariance estimation strategies for hybrid analog/digital mmWave system. One, we propose a sub-6 GHz covariance translation strategy to obtain mmWave channel covariance directly from sub-6 GHz. Two, we formulate the problem of covariance estimation for hybrid MIMO systems as a compressed signal recovery problem. To incorporate sub-6 GHz information in the proposed formulation, we introduce the concept of weighted compressed covariance estimation (similar to weighted sparse signal recovery [38]). The weights in the proposed approach are chosen based on the sub-6 GHz information. Finally, we quantify the loss in received post-processing SNR due to the use of imperfect covariance estimates.

Third, we propose to use a passive radar receiver at the roadside unit to reduce the training overhead of establishing a millimeter wave communication link. Specifically, the passive radar taps the transmissions from the automotive radars of the vehicles on road. The spatial covariance of the received radar signals is, in turn, used to establish the communication link. To this end, we propose a simplified radar receiver that does not require the transmitted

waveform as a reference. We also propose a covariance correction strategy to improve the similarity of the radar data and communication channel. We present the simulation results based on ray-tracing data to demonstrate the benefit of proposed radar covariance correction strategy and to show the potential of using passive radar for establishing the communication links. The results show that (i) covariance correction improves the similarity of radar and communication APS, and (ii) the proposed radar-assisted strategy reduces the training overhead significantly and is particularly useful in non-line-of-sight scenarios.

We summarize our contributions as follows:

- Chapter 2: Millimeter Wave Beam-Selection Using Sub-6 GHz Information

    1. Exploiting the limited scattering nature of mmWave channels and using the training on one OFDM subcarrier, we formulate the compressed beam-selection problem.
    2. We outline a strategy to extract spatial information from sub-6 GHz channel. The proposed strategy takes the mmWave beam-codebook design into consideration.
    3. We use weighted sparse signal recovery [38] to leverage out-of-band information in compressed beam-selection. The weights are chosen based on out-of-band information.

4. We propose a structured random codebook design for compressed beam-selection based on out-of-band information. The proposed design enforces the training precoder/combiner patterns to have high gains in the strong channel directions based on out-of-band information.

5. We formulate the compressed beam-selection as a multiple measurement vector (MMV) sparse recovery problem [39] to leverage training from all active subcarriers. The MMV based sparse recovery improves the beam-selection by a simultaneous recovery of multiple sparse signals with common support. We extend the weighted sparse recovery and structured codebook design to the MMV case.

6. Based on prior work, we draw conclusions about the expected degree of spatial congruence between sub-6 GHz and mmWave channels. Subsequently, we outline a multi-frequency channel model to generate channels that are consistent with frequency-dependent channel behavior observed in prior work. Using this model, we show that the proposed approach can reduce the training overhead of beam-selection considerably.

□ This work was published in [40] and [41].

- Chapter 3: Millimeter Wave Covariance Estimation Using Sub-6 GHz Information

  1. We propose an out-of-band covariance translation strategy for

MIMO systems. The proposed translation approach is based on a parametric estimation of the mean angle and angle spread (AS) of all clusters at sub-6 GHz. The estimated parameters are then used in the theoretical expressions of the spatial covariance at mmWave to complete the translation.

2. We formulate the problem of covariance estimation for mmWave hybrid MIMO systems as a compressed signal recovery problem. To incorporate out-of-band information in the proposed formulation, we introduce the concept of weighted compressed covariance estimation (similar to weighted sparse signal recovery [38]). The weights in the proposed approach are chosen based on the out-of-band information.

3. We use tools from singular vector perturbation theory [42] to quantify the loss in received post-processing SNR due to the use of imperfect covariance estimates. The singular vector perturbation theory has been used for robust bit-allocation [43] and robust block-diagonalization [44] in MIMO systems. For SNR degradation analysis, we consider a single path channel and find an upper and lower bound on the loss in SNR. The resulting expressions permit a simple and intuitive explanation of the loss in terms of the mismatch between the true and estimated covariance.

□ This work was published in [45] and [46].

- Chapter 4: Millimeter Wave Link Configuration Using Radar Information

    1. We propose to use a passive radar at the RSU. The passive radar at the RSU will tap the radar signals transmitted by the automotive radars mounted on the ego-vehicle. The spatial covariance of the radar signals received at the RSU is in turn used to configure the mmWave link.

    2. We propose a simplified radar receiver architecture that does not require the transmitted waveform as a reference. We show that the spatial covariance of the signals in the simplified architecture is the same as the spatial covariance with perfect waveform knowledge. Due to the lack of waveform knowledge, however, the range and Doppler cannot be recovered using the proposed architecture.

    3. In [37], it was shown that the angle estimation in frequency modulated continuous wave (FMCW) radar is biased. We note that a similar bias appears in frequency division duplex (FDD) systems, where the uplink (UL) covariance is used to configure the downlink (DL). After establishing this connection, we use a strategy initially proposed for FDD covariance correction [47], to correct the bias in FMCW radars.

    4. To use the radar information for configuring the mmWave links, it is necessary to understand the congruence (or similarity) of the

spatial information provided by radar and the spatial characteristic of the mmWave channel. Intuitively, by congruence, we mean the similarity in the azimuth power spectrum (APS) of radar and communication. To quantify this similarity, we propose a similarity metric to compare two power spectra. We show that in certain cases the proposed similarity metric is identical to relative precoding efficiency (RPE), i.e., a commonly used metric to measure the accuracy of covariance estimation in literature [48, 49, 50]. Further, [48], the RPE was related to the rate. As such, establishing a connection between the proposed metric and RPE also implies a connection between the proposed similarity metric and rate.

- □ Part of this work was published in [51] and a part is under preparation for submission.

1.5 Organization

The rest of this dissertation is organized as follows. In Chapter 2, we propose a strategy to perform mmWave analog beam-selection using sub-6 GHz information. In addition, we propose a strategy to generate multi-frequency channels. In Chapter 3, we propose two strategies for mmWave covariance estimation using sub-6 GHz information. The estimated covariance is used to configure hybrid analog/digital precoders at mmWave. In Chapter 4, we propose to use a passive radar to configure the mmWave link. Finally, we conclude the dissertation and describe future research directions in Chapter 5.

1.6 Abbreviations

ADC Analog-to-Digital Converter

AIC Akaike information criterion

AoA Angle-of-Arrival

AoD Angle-of-Departure

APS azimuth power spectrum

AS Angle Spread

COMP Covariance Orthogonal Matching Pursuit

CP Cyclic Prefix

CSI Channel State Information

DL Downlink

DCOMP Dynamic Covariance Orthogonal Matching Pursuit

DSRC Dedicated Short-Range Communication

FCC Federal Communications Commission

FDD Frequency Division Duplex

FMCW Frequency Modulated Continuous Wave

LIDAR Light Detection and Ranging

LOS Line-Of-Sight

LPF Low Pass Filter

LTE Long-Term Evolution

LW-DCOMP Logit Weighted - Dynamic Covariance Orthogonal Matching Pursuit

LW-OMP Logit Weighted - Orthogonal Matching Pursuit

LW-SOMP Logit Weighted - Simultaneous Orthogonal Matching Pursuit

MDL Minimum Description Length

MMV Multiple Measurement Vector

MRR Medium Range Radar

NR New Radio

NLOS Non-Line-Of-Sight

OMP Orthogonal Matching Pursuit

PDP Power Delay Profile

PPM Parts-Per-Million

RMS Root Mean Squared

RPE Relative Precoding Efficiency

RSU Road-Side-Unit

RX Receiver

SOMP Simultaneous Orthogonal Matching Pursuit

SNR Signal-to-Noise Ratio

TX Transmitter

UL Uplink

ULA Uniform Linear Array

V2I Vehicle-to-Infrastructure

V2V Vehicle-to-Vehicle

V2X Vehicle-to-Everything

1.7 Notation

We use the following notation throughout this dissertation. Bold lowercase $\mathbf{x}$ is used for column vectors, bold uppercase $\mathbf{X}$ is used for matrices, non-bold letters x, X are used for scalars. $[\mathbf{x}]_i$, $[\mathbf{X}]_{i,j}$, $[\mathbf{X}]_{i,:}$, and $[\mathbf{X}]_{:,j}$, denote ith entry of $\mathbf{x}$, entry at the ith row and jth column of $\mathbf{X}$, ith row of $\mathbf{X}$, and jth column of $\mathbf{X}$, respectively. We use the serif font, e.g., x, for the frequency-domain variables (the vectors (matrices) in frequency domain are represented

using bold serif font like x (X)). Superscript T, $*$ and $\dagger$ represent the transpose, conjugate transpose, and pseudo inverse, respectively. $\mathbf{0}$ and $\mathbf{I}$ denote the zero vector and identity matrix respectively. $\mathcal{CN}(\mathbf{x}, \mathbf{X})$ denotes a complex circularly symmetric Gaussian random vector with mean $\mathbf{x}$ and covariance $\mathbf{X}$. Further, $\mathcal{U}[a, b]$ is a Uniform random variable with support $[a, b]$. We use $\mathbb{E}[\cdot]$, $\|\cdot\|_p$, and $\|\cdot\|_{\mathrm{F}}$ to denote expectation, p norm and Frobenius norm, respectively. $\mathbf{X} \otimes \mathbf{Y}$ is the Kronecker product of $\mathbf{X}$ and $\mathbf{Y}$. Calligraphic letter $\mathcal{X}$ denotes a set and $[X]$ represents the set $\{1, 2, \cdots, X\}$. Finally, $|\cdot|$ is the absolute value of its argument or the cardinality of a set, and $\mathrm{vec}(\cdot)$ yields a vector for a matrix argument. The sub-6 GHz variables are underlined, as $\underline{\mathbf{x}}$, to distinguish them from mmWave.

Chapter 2

Millimeter Wave Beam-Selection Using Sub-6 GHz Information

In this chapter, we consider the problem of finding the optimal transmit/receive beam-pair for analog mmWave systems using sub-6 GHz information. We formulate the compressed beam-selection problem, outline a strategy to extract spatial information from sub-6 GHz channel, and use weighted sparse signal recovery [38] to leverage sub-6 GHz information in compressed beam-selection. We also propose a structured random codebook design for compressed beam-selection based on sub-6 GHz information. The proposed design enforces the training precoder/combiner patterns to have high gains in the strong channel directions. We also outline a multi-frequency channel model to generate channels that are consistent with frequency-dependent channel behavior observed in prior work. Using this channel model for simulations, we show that the proposed approach can reduce the training overhead of beam-selection considerably. This work was published in [40] and [41][1] (©IEEE).

[1]This chapter is based on A. Ali, N. González-Prelcic, and R. W. Heath Jr., "Millimeter wave beam-selection using out-of-band spatial information," *IEEE Trans. Wireless Commun.*, vol. 17, no. 2, pp. 1038-1052, 2018. A. Ali formulated the problem, conducted the numerical experiments, and wrote the initial draft of the manuscript. N. González-Prelcic and R. W. Heath Jr. provided critical feedback and helped shape the research and manuscript.

2.1 Motivation and prior work

MmWave communication systems use large antenna arrays and directional beamforming/precoding to provide sufficient link margin [1, 2]. Large arrays are feasible at mmWave as antennas can be packed into small form factors. Configuring these arrays, however, is not without challenges. First, the high power consumption of RF components makes fully digital baseband precoding difficult [1]. Second, the precoder design usually relies on channel state information, which is difficult to acquire at mmWave due to large antenna arrays and low pre-beamforming signal-to-noise ratio (SNR). Therefore, several approaches have been proposed to rapidly establish mmWave links [20, 21, 22, 23, 24]. The usual strategy is to exploit some sort of structure in the unknown channel that aids in link establishment, e.g., sparsity [20, 21] or channel dynamics [22].

MmWaves have applications in cellular systems [52, 1, 4], including fixed wireless access [53], backhaul [24], mobile access [1, 4], and even vehicle-to-everything (V2X) communications [10, 54]. The V2X application is of interest as the sensors on next generation intelligent vehicles may generate up to hundreds of Mbps [55], and the current vehicular communication mechanisms do not support such data-rates. MmWave communication has the potential to provide the required data-rates owing to the large bandwidth. Unfortunately, configuring mmWave links in high mobility is challenging as the link configuration could consume a significant fraction of the channel coherence interval, leaving little time for utilization.

We propose to leverage out-of-band information extracted from lower frequency channels to reduce the overhead of establishing a mmWave link. This is relevant as mmWave systems will likely be deployed in conjunction with lower frequency systems: (i) to provide wide area control signals; and/or (ii) for multi-band communications [29, 30]. The use of low-frequency information is feasible as the spatial characteristics of sub-6 GHz and mmWave channels are similar [56]. To motivate this idea, consider the hypothetical azimuth power spectrum (APS) of sub-6 GHz and mmWave shown in Fig. 2.1 (a). The APSs are substantially similar and we refer to this similarity as "*spatial congruence*". We can obtain a coarse estimate of the dominant directions from sub-6 GHz and use it at mmWave. Consider an elementary use case where the aim is to choose a suitable directional beam at mmWave from the candidate beams shown in Fig. 2.1 (b). The directional beams of the sub-6 GHz system in the strong directions of the channel are shown in Fig. 2.1 (c). The sub-6 GHz system has wider beams due to a small number of antennas. Given the sub-6 GHz spatial lobes, the candidate beams at mmWave can now be restricted only to those beams that overlap with sub-6 GHz spatial lobes as shown in Fig. 2.1 (d).

In this work, we use the sub-6 GHz *spatial information* to establish the mmWave link. Specifically, we consider the problem of finding the optimal transmit/receive beam-pair for analog mmWave systems. We assume wide-band frequency selective MIMO channels and OFDM signaling for both sub-6 GHz and mmWave systems. The mmWave system uses analog beamforming

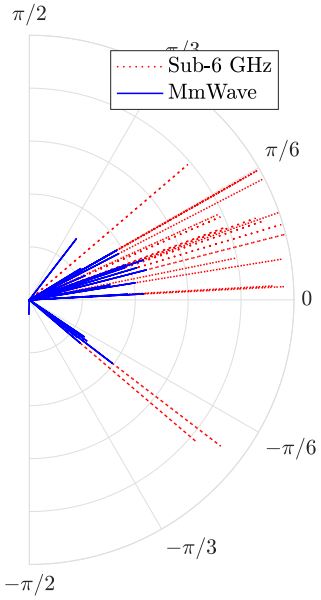

(a) Dominant paths at sub-6 GHz and mmWave

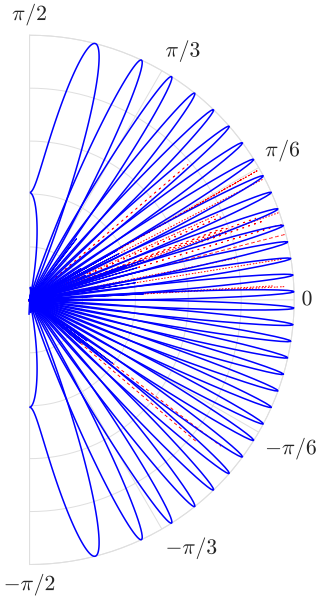

(b) Candidate beams at mmWave

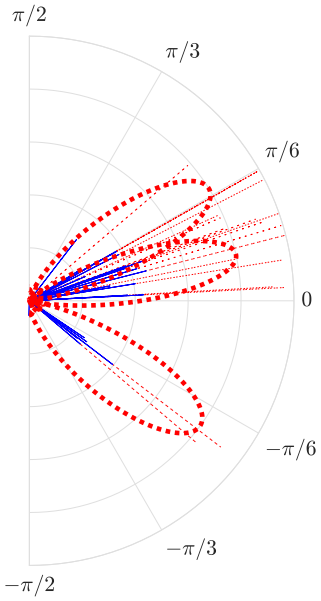

(c) Beams of sub-6 GHz system in strong channel directions

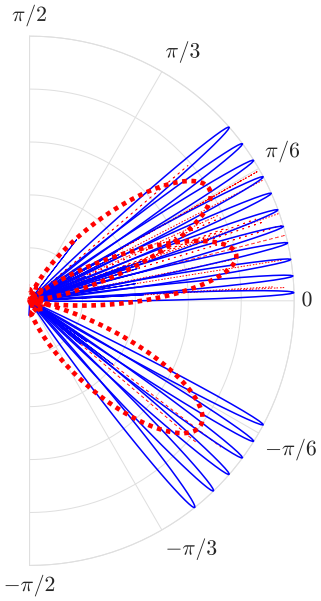

(d) Candidate beams at mmWave using sub-6 GHz information

Figure 2.1: An elementary use case for sub-6 GHz information in mmWave beam-selection.

with quantized phase-shifters, whereas the sub-6 GHz system is fully digital. Both sub-6 GHz and mmWave systems use uniform linear arrays (ULAs) at the transmitter (TX) and the receiver (RX).

Prior work on using out-of-band information in communication systems primarily targets beamforming reciprocity in frequency division duplex (FDD) systems. Based on the observation that the spatial information in the uplink (UL) and downlink (DL) is congruent [57, 58], several strategies were proposed to estimate DL correlation from UL measurements (see e.g., [47, 59, 60] and references therein). The estimated correlation was in turn used for DL beamforming. Along similar lines, in [61] the multi-paths in the UL channel were estimated and subsequently the DL channel was constructed using the estimated multi-paths. In [62], the UL measurements were used as partial support information in compressed sensing based DL channel estimation. The frequency separation between UL and DL is typically small. As an example, there is 9.82% frequency separation between 1935 MHz UL and 2125 MHz DL [58]. In essence, the aforementioned strategies were tailored for the case when the percent frequency separation of the channels under consideration is small and spatial information is congruent. We consider channels that can have frequency separation of several hundred percents, and hence some degree of spatial disagreement is expected.

There is some prior work on leveraging out-of-band information for mmWave communications. In [63], the directional information from legacy WiFi was used to reduce the beam-steering overhead of 60 GHz WiFi. The

measurement results presented in [63] confirm the value of out-of-band information for mmWave link establishment. Our work is distinguished from [63] as the techniques developed in this work are applicable to non-line-of-sight (NLOS) channels, whereas [63] primarily considered LOS channels. In [31], the authors study a joint sub-6 GHz-mmWave communication system and solve a scheduling problem over sub-6 GHz and mmWave interfaces to maximize the delay constrained throughput of the mmWave system. Our work, however, focuses on compressed beam-selection in analog mmWave systems using sub-6 GHz information. In [64], the coarse angle estimation at sub-6 GHz followed by refinement at mmWave was pitched. The implementation details and results, however, were not provided. The concept of radar aided mmWave communication was introduced in [34]. The information extracted from a mmWave radar was used to configure the mmWave communication link. Unlike [34], we use sub-6 GHz communication system's information for mmWave link establishment.

Compressed beam-selection was considered for a narrowband system in [21]. The problem was formulated using codebooks based on sampled array response vectors (i.e., with high-resolution phase-shifters) and did not consider out-of-band information. In contrast, we formulate the compressed beam-selection problem using codebooks based on low-resolution phase-shifters and aid the beam-selection with out-of-band information.

2.2 Contributions

The main contributions of this work are:

- Exploiting the limited scattering nature of mmWave channels and using the training on one OFDM subcarrier, we formulate the compressed beam-selection problem.
- We outline a strategy to extract spatial information from sub-6 GHz channel. The proposed strategy takes the mmWave beam-codebook design in consideration.
- We use weighted sparse signal recovery [38] to leverage out-of-band information in compressed beam-selection. The weights are chosen based on out-of-band information.
- We propose a structured random codebook design for compressed beam-selection based on out-of-band information. The proposed design enforces the training precoder/combiner patterns to have high gains in the strong channel directions based on out-of-band information.
- We formulate the compressed beam-selection as a multiple measurement vector (MMV) sparse recovery problem [39] to leverage training from all active subcarriers. The MMV based sparse recovery improves the beam-selection by a simultaneous recovery of multiple sparse signals with common support. We extend the weighted sparse recovery and structured codebook design to the MMV case.

- Based on prior work, we draw conclusions about the expected degree of spatial congruence between sub-6 GHz and mmWave channels. Subsequently, we outline a multi-frequency channel model to generate channels that are consistent with frequency-dependent channel behavior observed in prior work. Using this model, we show that the proposed approach can reduce the training overhead of beam-selection considerably.

The rest of the chapter is organized as follows: The system and channel models for mmWave and sub-6 GHz are outlined in Section 2.3. In Section 2.4, we formulate the compressed beam-selection problem. We outline the proposed out-of-band aided compressed beam-selection approach in Section 2.5. In Section 2.6, we review the prior work on frequency dependent channel behavior and outline a simulation strategy to generate multi-band frequency dependent channels. The simulation results are presented in Section 2.7, and Section 2.8 concludes the chapter.

2.3 System and channel model

We consider a multi-band MIMO system shown in Fig. 2.2, where ULAs of isotropic point sources are used at the TX and the RX. The ULAs are considered for ease of exposition, whereas, the proposed strategies can be extended to other array geometries with suitable modifications. We assume that the sub-6 GHz and mmWave arrays are co-located, aligned, and have comparable apertures. Both sub-6 GHz and mmWave systems operate simultaneously.

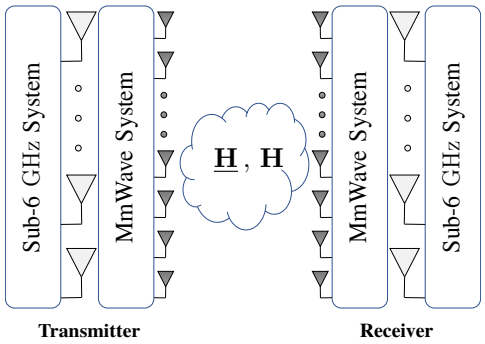

Figure 2.2: A multi-band MIMO system with co-located sub-6 GHz and mmWave antenna arrays. The sub-6 GHz channel is $\underline{\mathbf{H}}$ and the mmWave channel is $\mathbf{H}$.

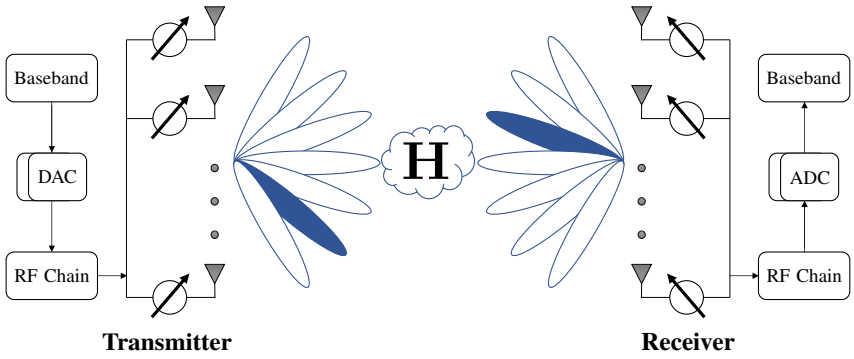

Figure 2.3: A mmWave system with phase-shifters based analog beamforming.

2.3.1 Millimeter wave system and channel model

The mmWave system is shown in Fig. 2.3. The TX has M_{TX} antennas and the RX has M_{RX} antennas. Both the TX and the RX are equipped with a single RF chain, hence only analog beamforming is possible. The idea of using out-of-band information can also be applied to hybrid analog/digital and fully digital low-resolution mmWave architectures, an interesting direction for future work. The mmWave system uses OFDM signaling with K

subcarriers. The data symbols $\mathsf{s}[k]$ are transformed to the time-domain using a K-point IDFT. A cyclic prefix (CP) of length L_{c} is then prepended to the time-domain samples before applying the analog precoder $\mathbf{f}$. The length L_{c} CP followed by the K time-domain samples constitute one OFDM block. The effective transmitted signal on subcarrier k is $\mathbf{f}\mathsf{s}[k]$. The data symbols follow $\mathbb{E}[\mathsf{s}[k]\mathsf{s}^*[k]] = \dfrac{P_{\mathrm{t}}}{K}$, where P_{t} is the total average power in the useful part, i.e., ignoring the CP, per OFDM block. Since $\mathbf{f}$ is implemented using analog phase-shifters, it has constant modulus entries i.e., $|[\mathbf{f}]_m|^2 = \frac{1}{M_{\mathrm{TX}}}$. Further, we assume that the angles of the analog phase-shifters are quantized and have a finite set of possible values. With these assumptions, $[\mathbf{f}]_m = \frac{1}{\sqrt{M_{\mathrm{TX}}}} e^{\mathrm{j}\zeta_m}$, where ζ_m is the quantized angle.

We assume perfect time and frequency synchronization at the receiver. The received signal is first combined using an analog combiner $\mathbf{q}$. The CP is then removed and the time-domain samples are converted back to the frequency-domain using a K-point DFT. If the $M_{\mathrm{RX}} \times M_{\mathrm{TX}}$ MIMO channel at the subcarrier k is denoted as $\mathbf{H}[k]$, the received signal on subcarrier $[k]$ after processing can be expressed as

$$\check{\mathsf{y}}[k] = \mathbf{q}^* \mathbf{H}[k] \mathbf{f} \mathsf{s}[k] + \mathbf{q}^* \check{\mathbf{v}}[k], \tag{2.1}$$

where $\check{\mathbf{v}}[k] \sim \mathcal{CN}(\mathbf{0}, \sigma^2_{\check{\mathbf{v}}} \mathbf{I})$.

We adopt a wideband geometric channel model with C clusters. Each cluster has a mean time delay $\tau_c \in \mathbb{R}$ and mean physical AoA/AoD $\{\theta_c, \phi_c\} \in [0, 2\pi)$. Each cluster is further assumed to contribute R_c rays/paths between

the TX and the RX. Each ray $r_c \in [R_c]$ has a relative time delay τ_{r_c}, relative AoA/AoD shift $\{\vartheta_{r_c}, \varphi_{r_c}\}$, and complex path gain α_{r_c}. Further, ρ_{pl} denotes the large-scale pathloss and $p(\tau)$ denotes the pulse shaping filter evaluated at point τ. Under this model, the delay-ℓ MIMO channel matrix $\mathbf{H}[\ell]$ can be written as [65]

$$\mathbf{H}[\ell] = \sqrt{\frac{M_{\text{RX}} M_{\text{TX}}}{\rho_{\text{pl}}}} \sum_{c=1}^{C} \sum_{r_c=1}^{R_c} \alpha_{r_c} p(\ell T_{\text{s}} - \tau_c - \tau_{r_c}) \times \mathbf{a}_{\text{RX}}(\theta_c + \vartheta_{r_c}) \mathbf{a}_{\text{TX}}^{*}(\phi_c + \varphi_{r_c}), \tag{2.2}$$

where T_{s} is the signaling interval and $\mathbf{a}_{\text{RX}}(\theta)$ and $\mathbf{a}_{\text{TX}}(\phi)$ are the antenna array response vectors of the RX and the TX, respectively. The array response vector of the RX is

$$\mathbf{a}_{\text{RX}}(\theta) = \frac{1}{\sqrt{M_{\text{RX}}}} [1, e^{\text{j}2\pi d \sin(\theta)}, \cdots, e^{\text{j}2\pi (M_{\text{RX}}-1) d \sin(\theta)}]^{\mathsf{T}}, \tag{2.3}$$

where d is the inter-element spacing in wavelength. The array response vector of the TX is defined in a similar manner. We normalize the array response vectors to have a unit norm and take out the effect of this normalization from the channel (2.2) by pre-multiplying with $\sqrt{M_{\text{RX}} M_{\text{TX}}}$. This practice ensures that (i) the precoders and combiners based on the array response vector do not need further normalization to be unit norm, and (ii) the channel is normalized irrespective of the number of antennas.

With the delay-ℓ MIMO channel matrix given in (2.2), the channel at subcarrier k, $\mathbf{H}[k]$ can be expressed as [65]

$$\mathbf{H}[k] = \sum_{\ell=0}^{L-1} \mathbf{H}[\ell] e^{-\text{j}\frac{2\pi k}{K}\ell}, \tag{2.4}$$

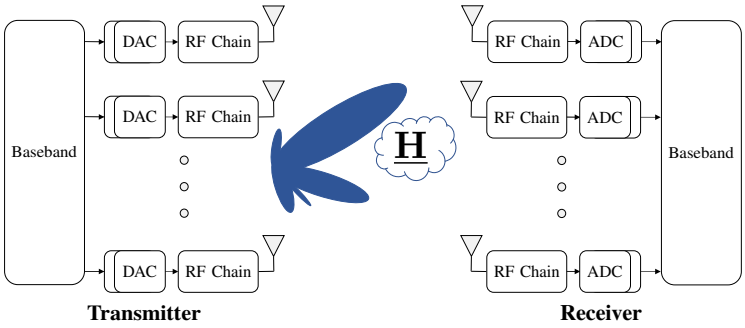

Figure 2.4: A sub-6 GHz system with digital precoding.

where $L \leq L_{\mathrm{c}} + 1$ is the number of taps in the mmWave channel.

2.3.2 Sub-6 GHz system and channel model

The sub-6 GHz system is shown in Fig. 2.4. Note that we underline all sub-6 GHz variables to distinguish them from the mmWave variables. The sub-6 GHz system has one RF chain per antenna and as such, fully digital precoding is possible. The channel model of sub-6 GHz is analogous to mmWave. The sub-6 GHz OFDM system has $\underline{K}$ subcarriers and a CP of length $\underline{L}_{\mathrm{c}}$. The time domain sub-6 GHz channel is thus restricted to have $\underline{L} \leq \underline{L}_{\mathrm{c}} + 1$ taps.

2.4 Problem Formulation

In this section, we formulate the compressed beam-selection problem. We discuss the beam codebook design for ULAs using low-resolution phase-shifters. We then present exhaustive beam-selection and the application of sparsity in the beam-selection problem. Subsequently, we formulate the compressed beam-selection problem for the analog mmWave system using training

from a single subcarrier. Finally, we extend the proposed formulation to leverage training data from all active subcarriers.

2.4.1 Beam codebook design

The beam-selection problem for analog mmWave systems is to select the best precoder (and combiner) from the candidate precoders (and combiners). Collectively the candidate precoders are called the precoding codebook. Here we discuss the design of the precoding codebook, but the same design applies to the combining codebook as well. Generating the precoding codebook by sampling the array response vector of the TX array at a few (carefully chosen) directions within the region of interest is a viable choice. Since ULAs produce unequal beamwidth according to the direction - i.e., narrower beams towards broadside and wider beams towards endfire - separating the sample directions according to the inverse sine is preferable, as it guarantees almost equal gain losses among the adjacent beams [66, 67]. Synthesizing the resulting precoders exactly, however, requires high-resolution phase-shifters. An approximation using D_{TX}-bit phase-shifters can be achieved by quantizing the phase of each element in the precoder to the nearest phase in the set $\{0, \frac{2\pi}{2^{D_{\mathrm{TX}}}}, \cdots, \frac{2\pi(2^{D_{\mathrm{TX}}}-1)}{2^{D_{\mathrm{TX}}}}\}$. Fig. 2.5 shows the codebook generated using the aforementioned method for a 32 element ULA. The region of interest is a 120° sector spanning the angles $[-\frac{\pi}{3}, \frac{\pi}{3})$ as in [67]. The number of codewords in the codebook is also 32.

Here onwards, we will assume that there are G_{TX} precoders in the TX

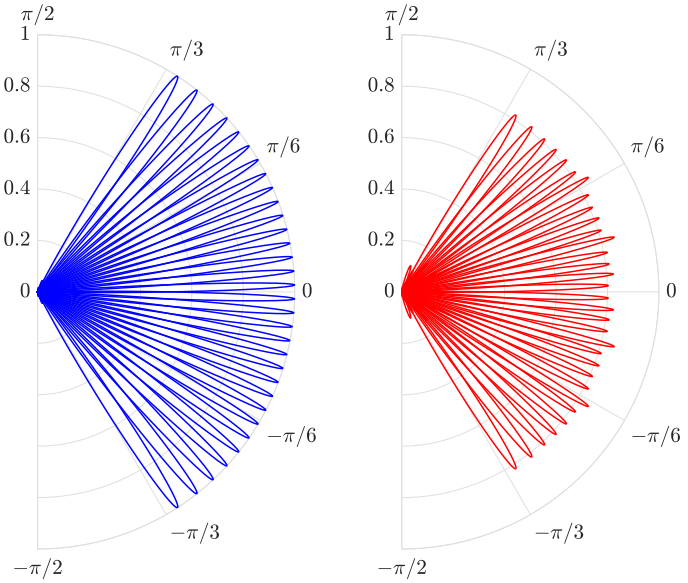

(a) Sampled array response vector based codebook

(b) 2-bit phase-shifter based approximation

Figure 2.5: The codebook based on sampled array response vectors and its approximation using 2-bit phase-shifters.

codebook and G_{RX} combiners in the RX codebook. We reserve the notation $\mathbf{w}_n$ for the nth precoder and $\mathbf{z}_m$ for the mth combiner. The $M_{\mathrm{TX}} \times G_{\mathrm{TX}}$ matrix $\mathbf{W} = [\mathbf{w}_1, \mathbf{w}_2, \cdots, \mathbf{w}_{G_{\mathrm{TX}}}]$ collects all the precoders. Similarly, the $M_{\mathrm{RX}} \times G_{\mathrm{RX}}$ matrix $\mathbf{Z} = [\mathbf{z}_1, \mathbf{z}_2, \cdots, \mathbf{z}_{G_{\mathrm{RX}}}]$ collects all the combiners. This notational choice for the precoders and combiners is intentionally different from the random precoders and combiners used later in compressed beam-selection.

In the compressed beam-selection problem formulation we will suppose that $\mathbf{W}\mathbf{W}^* \approx \mathbf{I}$, which is true for orthonormal precoders. In Fig. 2.6 we evaluate this approximation as a function of the number of antennas N_{TX} and the the number of phase-shifter bits D_{TX}, assuming $G_{\mathrm{TX}} = N_{\mathrm{TX}}$. The region of interest is 120° sector spanning the angles $[-\frac{\pi}{3}, \frac{\pi}{3})$. The accuracy of the approximation is tested using the metric $\frac{\|\mathbf{W}\mathbf{W}^* - \mathbf{I}\|_{\mathrm{F}}^2}{\|\mathbf{W}\mathbf{W}^*\|_{\mathrm{F}}^2}$. We can see that the approximation become accurate as D_{TX} increases. The achievable rate results presented in Section 2.7, however, show good performance even for $D_{\mathrm{TX}} = 2$.

2.4.2 Exhaustive beam-selection

In the training phase, the TX uses a precoding vector $\mathbf{w}_m$ and the RX uses a combining vector $\mathbf{q}_n$. Using the mmWave system model (2.1), the received signal on the kth subcarrier is

$$\check{\mathsf{y}}_{n,m}^{(\mathrm{E})}[k] = \mathbf{z}_n^* \mathbf{H}[k] \mathbf{w}_m \mathsf{s}_m[k] + \mathbf{z}_n^* \check{\mathbf{v}}_{n,m}^{(E)}[k], \tag{2.5}$$

where $\mathbf{w}_m \mathsf{s}_m[k]$ is the precoded training symbol on subcarrier k. The superscript (E) on a variable signifies its association to exhaustive beam-selection.

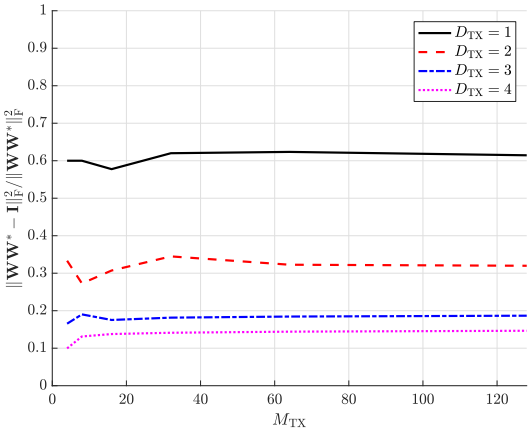

Figure 2.6: The metric $\frac{\|\mathbf{WW}^* - \mathbf{I}\|_{\mathrm{F}}^2}{\|\mathbf{WW}^*\|_{\mathrm{F}}^2}$ for different phase-shifter bit-resolution and number of antennas M_{TX}.

The receiver divides through by the training symbol $\mathsf{s}_m[k]$ to get

$$\mathsf{y}_{n,m}^{(\mathrm{E})}[k] = \mathbf{z}_n^* \mathbf{H}[k] \mathbf{w}_m + \mathbf{v}_{n,m}^{(E)}[k], \tag{2.6}$$

where $\mathbf{v}_{n,m}^{(\mathrm{E})}[k]$ is the post-processing noise after combining and division by the training. The TX transmits the training OFDM blocks on G_{TX} precoding vectors. For each precoding vector, the RX uses G_{RX} distinct combining vectors. The number of total training blocks is $G_{\mathrm{RX}} \times G_{\mathrm{TX}}$. Collecting the signals (2.6), we get an $G_{\mathrm{RX}} \times G_{\mathrm{TX}}$ matrix

$$\mathbf{Y}^{(\mathrm{E})}[k] = \mathbf{Z}^* \mathbf{H}[k] \mathbf{W} + \mathbf{V}^{(\mathrm{E})}[k]. \tag{2.7}$$

The largest absolute entry in $\mathbf{Y}^{(\mathrm{E})}[k]$ determines best beam-pair. If we denote $\mathbf{y}^{(\mathrm{E})}[k] = \mathrm{vec}(\mathbf{Y}^{(\mathrm{E})}[k])$, then $r^\star = \underset{1 \le r \le G_{\mathrm{RX}} \times G_{\mathrm{TX}}}{\arg\max} |[\mathbf{y}^{(\mathrm{E})}[k]]_r|$, determines the best beam-pair. Specifically, the best precoder index is $j^\star = \lceil \frac{r^\star}{G_{\mathrm{RX}}} \rceil$, and the best combiner index is $i^\star = r^\star - (j^\star - 1) G_{\mathrm{RX}}$. The receiver needs to feedback

the best precoder index to the transmitter, which can be achieved using the active sub-6 GHz link. Note that we did not keep the index $[k]$ with r as the analog precoder and combiner are independent of the subcarrier. Constructing $\mathbf{Y}^{(\mathrm{E})}[k]$ (or $\mathbf{y}^{(\mathrm{E})}[k]$) by exhaustive-search as in (2.7) incurs a training overhead of $G_{\mathrm{RX}} \times G_{\mathrm{TX}}$ blocks.

2.4.3 Sparsity in beam-selection

The crux of compressed beam-selection is to reduce the training overhead of beam-selection by exploiting the spatial clustering of multi-paths in the channel. To this end, let us re-write the noise free version of (2.7) as

$$\mathbf{E}[k] = \mathbf{Z}^{*}\mathbf{H}[k]\mathbf{W}. \tag{2.8}$$

Due to the spatial clustering in the mmWave channel, the matrix $\mathbf{E}[k]$ is sparse. We show an example for a 64×16 MIMO system in Fig. 2.7. The channel has a single cluster at $\theta = \phi = 0$ with arrival and departure spread of 2°.

Note that depending on the AoA and AoD, even a single path channel will not yield $\mathbf{E}[k]$ with a single non-zero coefficient. This is because any ray illuminates multiple consecutive beams, albeit with reduced power moving from the closest beam to the farthest. With large enough antenna arrays at the transmitter and receiver and a few clusters with small AS in the mmWave channel, the matrix $\mathbf{E}[k]$ can be considered approximately sparse. As such, we can proceed by assuming that $\mathbf{E}[k]$ is a sparse matrix. Note that, in this work, we do not exploit the sparsity in delay-domain, as in e.g., [68]. As such, the time-offset of the incoming rays is irrelevant.

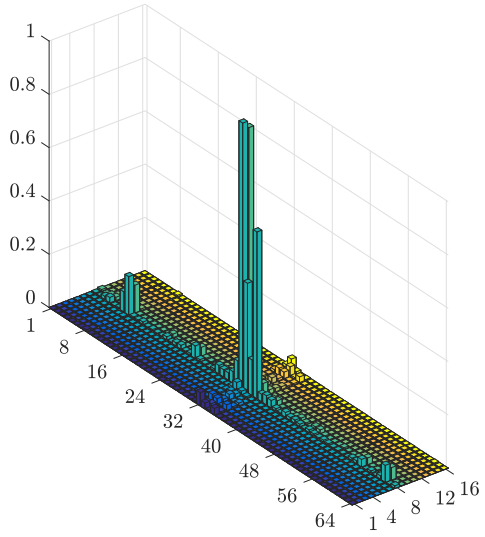

Figure 2.7: The matrix $|\mathbf{E}[k]|$ for a 64×16 MIMO system and a single cluster channel with angles $\theta = \phi = 0$ and arrival and departure spread of 2°

2.4.4 Compressed beam-selection

The training burden of beam-selection can be reduced by exploiting the sparsity of $\mathbf{E}[k]$. The resulting framework, called compressed beam-selection, uses a few random measurements to estimate $r^\star$. The random training codebooks that respect the analog beamforming constraints were reported in [69], where TX designs its $M_{\mathrm{TX}} \times N_{\mathrm{TX}}$ training codebook such that $[\mathbf{F}]_{n,m} = \frac{1}{\sqrt{M_{\mathrm{TX}}}} e^{\mathrm{j}\zeta_{n,m}}$, where $\zeta_{n,m}$ is randomly and uniformly selected from the set of quantized angles $\{0, \frac{2\pi}{2^{D_{\mathrm{TX}}}}, \cdots, \frac{2\pi(2^{D_{\mathrm{TX}}}-1)}{2^{D_{\mathrm{TX}}}}\}$. The RX similarly designs its $M_{\mathrm{RX}} \times N_{\mathrm{RX}}$ training codebook $\mathbf{Q}$. Similar to (2.7), we collect all measurements in a $N_{\mathrm{RX}} \times N_{\mathrm{TX}}$ training matrix $\mathbf{Y}[k]$ to get

$$\mathbf{Y}[k] = \mathbf{Q}^* \mathbf{H}[k] \mathbf{F} + \mathbf{V}[k], \tag{2.9}$$

which is further vectorized to set up the following system

$$\mathbf{y}[k] = \text{vec}(\mathbf{Y}[k]) = (\mathbf{F}^{\mathsf{T}} \otimes \mathbf{Q}^*)\text{vec}(\mathbf{H}[k]) + \text{vec}(\mathbf{V}[k]). \tag{2.10}$$

At this stage, using the relation $\mathbf{E}[k] = \mathbf{Z}^*\mathbf{H}[k]\mathbf{W}$ from (2.8), and the approximations $\mathbf{Z}\mathbf{Z}^* \approx \mathbf{I}$ and $\mathbf{W}^*\mathbf{W} \approx \mathbf{I}$, we get $\mathbf{H}[k] \approx \mathbf{Z}\mathbf{E}[k]\mathbf{W}^*$. We plug this approximation in (2.10) to get

$$\begin{aligned}
\mathbf{y}[k] &\approx (\mathbf{F}^{\mathsf{T}} \otimes \mathbf{Q}^*)(\mathbf{W}^{\text{c}} \otimes \mathbf{Z})\text{vec}(\mathbf{E}[k]) + \text{vec}(\mathbf{V}[k]), \\
&\overset{(a)}{=} (\mathbf{F}^{\mathsf{T}} \otimes \mathbf{Q}^*)(\mathbf{W}^{\text{c}} \otimes \mathbf{Z})\mathbf{e}[k] + \text{vec}(\mathbf{V}[k]) \\
&\overset{(b)}{=} \mathbf{\Psi}\mathbf{e}[k] + \text{vec}(\mathbf{V}[k]).
\end{aligned} \tag{2.11}$$

In (2.11), (a) follows from the notational choice $\mathbf{e}[k] = \text{vec}(\mathbf{E}[k])$ and (b) follows by introducing the sensing matrix $\mathbf{\Psi} = (\mathbf{F}^{\mathsf{T}} \otimes \mathbf{Q}^*)(\mathbf{W}^{\text{c}} \otimes \mathbf{Z})$. Exploiting the sparsity of $\mathbf{e}$, $r^\star$ can be estimated reliably, even when $N_{\text{TX}} \ll G_{\text{TX}}$ and $N_{\text{RX}} \ll G_{\text{RX}}$. The system (2.11) can be solved for sparse $\mathbf{e}[k]$ using any of the sparse signal recovery techniques. In this work, we use the orthogonal matching pursuit (OMP) algorithm [70]. We outline the working principle of OMP here and refer the interested readers to [70] for details. The OMP algorithm uses a greedy approach in which the support is constructed in an incremental manner. At each iteration, the OMP algorithm adds to the support estimate the column of $\mathbf{\Psi}$ that is most highly correlated with the residual. The measurement vector $\mathbf{y}[k]$ is used as the first residual vector, and subsequent residual vectors are calculated as $\tilde{\mathbf{y}}[k] = \mathbf{y}[k] - \mathbf{\Psi}\hat{\mathbf{e}}[k]$, where $\hat{\mathbf{e}}[k]$ is the least squares estimate of $\mathbf{e}[k]$ on the support estimated so far. As we are interested only in $r^\star$, we can

find the approximate solution in a single step using the OMP framework, i.e.,

$$r^\star = \underset{1\leq r\leq G_{\mathrm{RX}}G_{\mathrm{TX}}}{\arg\max} \; |[\mathbf{\Psi}]^*_{:,r}\mathbf{y}[k]|. \tag{2.12}$$

A single step solution implies low computational complexity of the proposed approach, and makes it suitable for practical implementations.

2.4.5 Leveraging data from all active subcarriers

If the unknowns $\mathbf{e}[k]$ were recovered on all subcarriers, a suitable criterion for choosing $r^\star$ could be $r^\star = \underset{1\leq r\leq G_{\mathrm{RX}}G_{\mathrm{TX}}}{\arg\max} \sum_{k\in[K]} |[\mathbf{e}[k]]_r|$. One can recover the vectors $\mathbf{e}[k]$ individually on each subcarrier and then find $r^\star$. Instead, we note that the unknown sparse vectors have a similar sparsity pattern i.e., they share an approximately common support [71]. To exploit the common support property, we formulate a joint recovery problem using measurements from all subcarriers. Formally, we collect all vectors $\mathbf{y}[k]$ in a matrix $\bar{\mathbf{Y}}$, which can be written as

$$\begin{aligned}
\bar{\mathbf{Y}} &= [\mathbf{y}[1]\ \mathbf{y}[2]\ \cdots\ \mathbf{y}[K]]\,, \\
&= \mathbf{\Psi}\,[\mathbf{e}[1]\ \mathbf{e}[2]\ \cdots\ \mathbf{e}[K]] + [\mathbf{v}[1]\ \mathbf{v}[2]\ \cdots\ \mathbf{v}[K]], \\
&= \mathbf{\Psi}\bar{\mathbf{E}} + \bar{\mathbf{V}}.
\end{aligned} \tag{2.13}$$

The columns of $\bar{\mathbf{E}}$ are approximately jointly sparse, i.e., $\bar{\mathbf{E}}$ has only a few non-zero rows. The sparse recovery problems of the form (2.13) are referred to as MMV problems. The simultaneous OMP (SOMP) algorithm [39] is an

OMP variant tailored for MMV problems. Using SOMP, $r^\star$ can be found as

$$r^\star = \underset{1\leq r\leq G_{\mathrm{RX}}G_{\mathrm{TX}}}{\arg\max} \sum_{k\in[K]} |[\mathbf{\Psi}]^*_{:,r}\mathbf{y}[k]|. \tag{2.14}$$

The summation over k (i.e., subcarriers) ensures that the measurements from all subcarriers contribute in deciding the best beam-pair.

2.5 Out-of-band aided compressed beam-selection

The proposed out-of-band aided compressed beam-selection is a two-stage procedure. In the first stage, the spatial information is extracted from sub-6 GHz channel. In the second stage, the extracted information is used for compressed beam-selection.

2.5.1 First stage (spatial information retrieval from sub-6 GHz)

The spatial information sought from sub-6 GHz is the dominant spatial directions i.e., AoAs/AoDs. Prior work has considered the specific problem of estimating both the AoAs/AoDs (see e.g.,[72]) and the AoAs/AS (see e.g., [73]) from an empirically estimated spatial correlation matrix. The generalization of these strategies to joint AoA/AoD/AS estimation, however, is not straightforward. Further, angle estimation algorithms typically rely on channel correlation knowledge which is difficult to acquire for rapidly varying channels. Therefore, we seek a methodology that can provide reliable spatial information for rapidly varying channels with minimal overhead. For the application at hand, the demand on the accuracy of the direction estimates,

however, is not particularly high. Due to the inherent differences between sub-6 GHz and mmWave channels, the extracted spatial information will have an unavoidable mismatch. Consequently, we only need a coarse estimate of the angular information from sub-6 GHz.

We assume that the estimate of the MIMO channel taps $\underline{\hat{\mathbf{H}}}[\ell]$ or equivalently $\underline{\mathbf{H}}[k]$ is available (see e.g., [74] for OFDM channel estimation techniques). The estimate of MIMO channel $\underline{\hat{\mathbf{H}}}[\ell]$ is required for the operation of sub-6 GHz system itself. Hence, the spatial information extraction from the sub-6 GHz channel does not incur any additional training overhead from out-of-band information retrieval point of view. The directional estimate from sub-6 GHz to be used with mmWave beam-selection can be constructed as

$$\underline{\hat{\mathbf{E}}}[k] = \underline{\mathbf{Z}}^{*} \underline{\mathbf{H}}[k] \, \underline{\mathbf{W}}, \tag{2.15}$$

where $\underline{\mathbf{W}}$ comprises of sub-6 GHz TX array response vector sampled at the same spatial points as used for mmWave codebook generation. We refer to $|\underline{\hat{\mathbf{E}}}[k]| \in \mathbb{R}^{G_{\mathrm{RX}} \times G_{\mathrm{TX}}}$ as the spatial spectrum. The same procedure is used for constructing $\underline{\mathbf{Z}}$. The spatial spectrum averaged over all sub-6 GHz subcarriers $|\underline{\hat{\mathbf{E}}}|$ is used as out-of-band information in compressed beam-selection. We show the spatial spectrum $|\underline{\hat{\mathbf{E}}}|$ of an 8×2 sub-6 GHz MIMO system for the example considered in Section 2.4.3 in Fig. 2.8.

The spatial spectrum $|\underline{\hat{\mathbf{E}}}|$ is directly used in weighted sparse signal recovery. The structured random codebook design, however, requires the indices of the dominant sub-6 GHz precoders and combiners. These indices can be

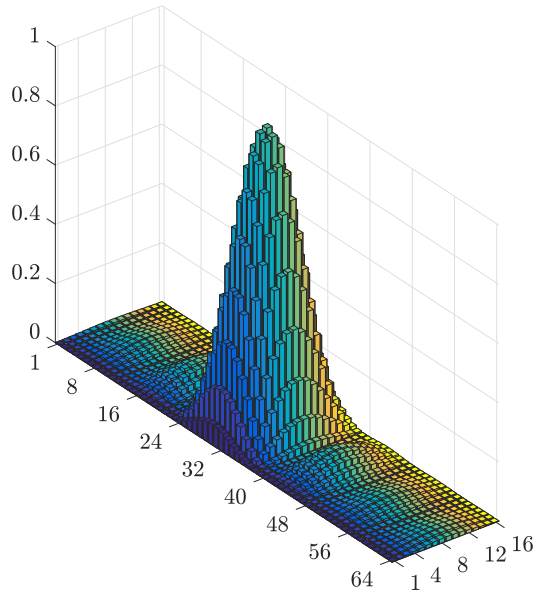

Figure 2.8: The 64x16 matrix $|\underline{\hat{\mathbf{E}}}|$ for an 8x2 MIMO channel. The channel has a single cluster channel with angles $\theta = \phi = 0$ and arrival and departure spread of 2°.

easily found by inspecting the spatial spectrum. We collect the indices of the O dominant precoders in the set $\mathcal{J}$ and the set of dominant combiners in the set $\mathcal{I}$.

2.5.2 Second stage (out-of-band aided compressed beam-selection)

We explain the out-of-band aided compressed beam-selection in two parts. The first part is the weighted sparse recovery and the second is the structured random codebook design.

Weighted sparse recovery: Weighted sparse recovery is not limited to OMP and several strategies exist, see e.g., [75, 76, 77, 78, 79, 80, 81]. We, however, focus on weighted sparse recovery using OMP. The OMP based sparse recovery assumes that the prior probability of the support is uniform, i.e., all elements of the unknown can be active with the same probability p. If some prior information about the non-uniformity in the support is available, the OMP algorithm can be modified to incorporate this prior information. In [38] a modified OMP algorithm called logit weighted - OMP (LW-OMP) was proposed for non-uniform prior probabilities. Assume that $\mathbf{p} \in \mathbb{R}^{G_{\mathrm{TX}}G_{\mathrm{RX}}}$ is the vector of prior probabilities. Specifically, the rth element of $\mathbf{e}[k]$ can be active with prior probability $0 \leq [\mathbf{p}]_r \leq 1$. Then $r^\star$ can be found using LW-OMP as

$$r^\star = \underset{1\leq r\leq M_{\mathrm{RX}}M_{\mathrm{TX}}}{\arg\max} \; |[\mathbf{\Psi}]^*_{:,r}\mathbf{y}[k]| + w([\mathbf{p}]_r), \tag{2.16}$$

where $w([\mathbf{p}]_r)$ is an additive weighting function. The authors refer the interested reader to [38] for the details of LW-OMP and the selection of $w([\mathbf{p}]_r)$.

The general form of $w([\mathbf{p}]_r)$ can be given as $w([\mathbf{p}]_r) = J_{\mathrm{w}} \log \dfrac{[\mathbf{p}]_r}{1-[\mathbf{p}]_r}$, where J_{w} is a constant that depends on sparsity level, the amplitude of the unknown coefficients, and the noise level. In the absence of prior information, (2.16) can be solved using uniform probability $\mathbf{p} = \delta \mathbf{1}$, where $0 < \delta <= 1$, which is equivalent to solving (2.12).

The spatial information from sub-6 GHz can be used to obtain a proxy for $\mathbf{p}$. The probability vector $\mathbf{p} \in \mathbb{R}^{G_{\mathrm{RX}} G_{\mathrm{TX}}}$ is obtained using $|\hat{\underline{\mathbf{E}}}| \in \mathbb{R}^{G_{\mathrm{RX}} \times G_{\mathrm{TX}}}$. Let $\hat{\underline{\mathbf{e}}} = \mathrm{vec}(\hat{\underline{\mathbf{E}}})$, then a simple proxy of the probability vector based on the spatial spectrum can be

$$\mathbf{p} = J_{\mathrm{p}} \frac{|\hat{\underline{\mathbf{e}}} - \min(\hat{\underline{\mathbf{e}}})|}{\max(\hat{\underline{\mathbf{e}}}) - \min(\hat{\underline{\mathbf{e}}})}. \tag{2.17}$$

Initially the spectrum is scaled to meet the probability constraint $0 \leq [\mathbf{p}]_r \leq 1$. The subsequent scaling by$J_{\mathbf{p}} \in (0, 1]$ captures the reliability of out-of-band-information. The reliability is a function of the sub-6 GHz and mmWave spatial congruence, and operating SNR. For highly reliable information, a higher value can be used for J_{p}.

Structured random codebooks: So far we have considered random codebooks that respect the analog hardware constraints, i.e., constant modulus and quantized phase-shifts. The random codebooks used for training, however, can be tailored to out-of-band information. We describe the design of structured codebooks for precoders, but it also applies to the combiners.

Recall that $\mathcal{J}$ is the index set associated with the dominant precoders. Hence $[\mathbf{W}]_{:,\mathcal{J}}$ are the dominant precoders. We construct a super random code-

book $\bar{\mathbf{F}}$ containing $\bar{N}_{\mathrm{TX}} \gg N_{\mathrm{TX}}$ codewords according to [69]. The desired random codebook then consists of the N_{TX} codewords from the super codebook that have the highest correlation with the precoder $[\mathbf{W}]_{:,\mathcal{J}}$. The procedure to generate structured precoding codebooks is summarized in Algorithm 1. The LW-OMP algorithm with structured codebooks is referred to as structured LW-OMP.

Algorithm 1 Structured random codebook design

Input: $\mathcal{J}$, $\mathbf{W}$

Output: $\mathbf{F}$

1: Construct a super-codebook $\bar{\mathbf{F}}$ using $\bar{N}_{\mathrm{TX}}$ random codewords generated according to [69].
2: Let $\mathbf{N} = \bar{\mathbf{F}}^{*}[\mathbf{W}]_{:,\mathcal{J}}$. Populate the index set $\mathcal{M}$ with the indices of N_{TX} rows of $\mathbf{N}$ that have the largest 2-norms.
3: Create the precoding matrix $\mathbf{F} = [\bar{\mathbf{F}}]_{:,\mathcal{M}}$.

The sensing matrices constructed from structured random codebooks and purely random codebooks are expected to have different mutual coherence. Formally, we define mutual coherence of the sensing matrix as $\chi(\mathbf{\Psi}) = \max_{m<n} \frac{|[\mathbf{\Psi}]^{*}_{:,m}[\mathbf{\Psi}]_{:,n}|}{\|[\mathbf{\Psi}]_{:,m}\|^2 \|[\mathbf{\Psi}]_{:,n}\|^2}$ [82]. We show the mutual coherence as a function of the number of measurements for sensing matrices based on random dictionaries and structured random dictionaries in Fig. 2.9. We can observe that the mutual coherence of a sensing matrix based on structured random codebooks is higher. From application point of view, however, the structured random codebooks take more meaningful random measurements in the directions that are more likely to be active, and hence can provide gains in compressed beam-selection.

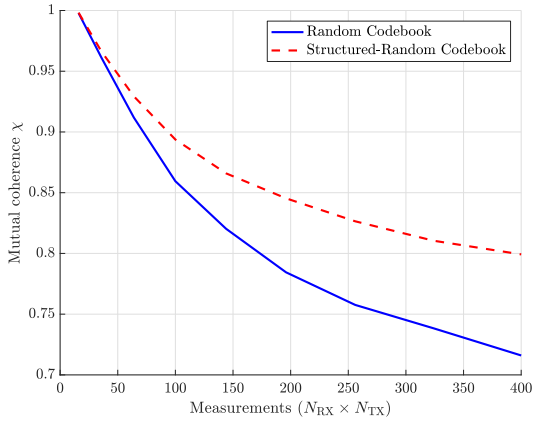

Figure 2.9: The mutual coherence χ of sensing matrices based on random codebooks and structured-random codebooks.

Finally, if all active subcarriers are used for the training, out-of-band information can be incorporated in SOMP algorithm via logit weighting and structured codebooks. Specifically, the logit weighted - SOMP (LW-SOMP) algorithm [83] finds $r^\star$ by

$$r^\star = \underset{1\leq r\leq G_{\mathrm{RX}}G_{\mathrm{TX}}}{\arg\max} \sum_{k\in[K]} |[\mathbf{\Psi}]^*_{:,r}\mathbf{y}[k]| + w([\mathbf{p}]_r). \tag{2.18}$$

The LW-SOMP algorithm used with structured random codebooks is termed structured LW-SOMP.

2.6 Multi-band channel characteristics and simulation

The out-of-band aided mmWave beam-selection strategies proposed in this work rely on the information extracted at sub-6 GHz. Therefore, it is essential to understand the similarities and differences between sub-6 GHz and mmWave channels. Furthermore, to assess the performance of proposed out-

of-band aided mmWave link establishment strategies, a simulation strategy is required to generate multi-band frequency dependent channels. In this section, we review a representative subset of prior work to draw conclusions about the expected degree of spatial congruence between sub-6 GHz and mmWave channels. Based on these results, we outline a strategy to simulate multi-band frequency dependent channels.

2.6.1 Review of multi-band channel characteristics

The material properties change with frequency, e.g., the relative conductivity and the average reflection increase with frequency [84, 85]. Hence, some characteristics of the channel are expected to vary with frequency. It was reported that the delay spread decreases [86, 87, 88, 89, 90], the number of angle-of-arrival (AoA) clusters increase [91], the shadow fading increases [88], and the angle spread (AS) of clusters decreases [89, 87] with frequency. Further, it was observed that the late arriving multi-paths have more frequency dependence due to higher interactions with the environment [92, 93].

Not all channel characteristics vary greatly with frequency. As an example, the existence of spatial congruence between the UL and DL channels is well established [57, 58]. In [57], it was noted that though the propagation channels in UL and DL are not reciprocal, the spatial information is congruent. It was observed in measurements (for 1935 MHz UL and 2125 MHz DL) that the deviation in AoAs of dominant paths of UL and DL is small with high probability [58]. Prior work has exploited the spatial congruence between UL

and DL channels to reduce/eliminate the feedback in FDD systems, see e.g., [47, 59, 61, 62].

Some channel characteristics are congruent for larger frequency separations. In [56], the directional power distribution of 5.8 GHz, 14.8 GHz, and 58.7 GHz LOS indoor channels were reported to be almost identical. The number of resolvable paths, the decay constants of the clusters, the decay constants of the subpaths within the clusters, and the number of angle-of-departure (AoD) clusters were found to be similar in 28 and 73 GHz channels [91] in an outdoor scenario. In [94], similar power delay profiles (PDPs) were reported for 10 GHz and 30 GHz indoor channels. The received power as a function of distance was found to be similar for 5.8 GHz and 14.8 GHz in [56]. Only minor differences were observed in the CDFs of delay spread, azimuth AoA/AoD spread, and elevation AoA/AoD spread of six different frequencies between 2 GHz and 60 GHz in the outdoor environments studied in [95].

To the best of authors' knowledge there is no prior work on simultaneous measurements of sub-6 GHz and mmWave vehicular channels. As such, the spatial congruence (or lack of it) for such channels is yet to be established. The existing studies in indoor [56, 94] and outdoor [91, 95], however, confirm that there can be substantial similarity between channels at different frequencies, even with large separations. Hence, it is likely that there is significant, albeit not perfect, congruence between sub-6 GHz and mmWave channels. This observation is leveraged by prior work that used legacy WiFi measurements to configure 60 GHz WiFi links [63].

Due to the differences in the wavelength of sub-6 GHz and mmWave frequencies, it is possible that the Fresnel zone clarity criterion for LOS - e.g., first Fresnel zone 80% obstruction free - is satisfied at sub-6 GHz but, not for mmWave. This would imply that the sub-6 GHz channel is LOS and the mmWave channel is NLOS. It is expected that the out-of-band aided link establishment will not perform well in such scenarios as the spatial information in a LOS sub-6 GHz and NLOS mmWave may be different. In this case, one option is to detect such scenarios and revert to in-band only link establishment. Another option is use machine learning based methods e.g., [96].

2.6.2 Simulation of multi-band frequency dependent channels

The following observations are made about the frequency dependent channel behavior from the review of the prior work:

- The channel characteristics differ with frequency, and the differences increase as the percent separation between center frequencies of the channels increase.
- The late arriving multi-paths have more frequency dependence [92, 93].
- Some paths may be present at one frequency but not at the other [97].

The proposed multi-band frequency dependent channel simulation algorithm takes the aforementioned observations into consideration. It takes the parameters of the channels at two frequencies as input and outputs a

random realization for each of the two channels. The input parameters include the number of clusters, the number of paths within a cluster, root mean squared (RMS) delay spread, RMS delay spread of the paths within clusters, center frequency, and the RMS AS of the paths within clusters. The output random realizations of the two channels are consistent in the sense that one of the channels is a perturbed version of the other, where the perturbation model respects the frequency dependent channel behavior. Before discussing the proposed simulation algorithm, we present the required preliminaries.

The following exposition is applicable to the channels at two frequencies f_1 and f_2 (not necessarily sub-6 GHz and mmWave). Therefore, we use subscript index $i \in [I]$, where $I = 2$, to distinguish the parameters of the channel at center frequency f_1 from the parameters of the channel at center frequency f_2. We assume that there are C_i clusters in the channel i. Each cluster has a mean time delay $\tau_{c,i}$ and mean physical AoA/AoD $\{\theta_{c,i}, \phi_{c,i}\} \in [0, 2\pi)$. Each cluster c_i is further assumed to contribute $R_{c,i}$ rays/paths between the TX and the RX. Each ray $r_{c,i} \in [R_{c,i}]$ has a relative time delay $\tau_{r_{c,i}}$, relative AoA/AoD shift $\{\vartheta_{r_{c,i}}, \varphi_{r_{c,i}}\}$, and complex path gain $\alpha_{r_{c,i}}$. If $\rho_{\text{pl},i}$ represents the path-loss, then the omni-directional impulse response of the channel i can be written as

$$h_{\text{omni},i}(t, \theta, \phi) = \frac{1}{\sqrt{\rho_{\text{pl},i}}} \sum_{c_i=1}^{C_i} \sum_{r_{c,i}=1}^{R_{c,i}} \alpha_{r_{c,i}} \delta(t - \tau_{c,i} - \tau_{r_{c,i}}) \times \\ \delta(\theta - \theta_{c,i} - \vartheta_{r_{c,i}}) \times \delta(\phi - \phi_{c,i} - \varphi_{r_{c,i}}). \tag{2.19}$$

The continuous time channel impulse response given in (2.19) is not band-limited. The impulse response convolved with the pulse shaping filter, how-

ever, is band-limited and can be sampled to obtain the discrete time channel as in Section 2.3. Further, in (2.19) we have only considered the azimuth AoAs/AoDs for simplicity. The general formulation with both azimuth and elevation angles is a straightforward extension, see [91]. A detailed discussion on the choice of the channel parameters is beyond the scope of this dissertation. The reader is directed to prior work e.g., [98] for discussions on suitable channel parameters. A cursory guideline can be established, however, based on the literature review presented earlier. Assuming $f_1 \leq f_2$ it is expected that $C_1 \geq C_2$ [91], $R_{c,1} \geq R_{c,2}$ [91], $\tau_{\max,1} \geq \tau_{\max,2}$ [86, 87, 88, 89], $\sigma_{\vartheta_{c,1}} \geq \sigma_{\vartheta_{c,2}}$, and $\sigma_{\varphi_{c,1}} \geq \sigma_{\varphi_{c,2}}$ [89, 87]. Furthermore, the parameters used for numerical evaluations in Section 2.7 are an example of the parameters that comply with the observations of the prior work.

The proposed channel simulation strategy is based on a two-stage algorithm. In the first stage, the mean time delays $\tau_{c,i}$ and mean AoAs/AoDs $\{\theta_{c,i}, \phi_{c,i}\}$ of the clusters are generated together for both frequencies, while respecting the frequency dependent behavior. In the second stage, the paths within the clusters are generated independently for both frequencies. The first stage of the proposed channel simulation algorithm is outlined in Algorithm 2.

2.6.2.1 First Stage

The number of clusters C_i, the RMS delay spreads $\tau_{\mathrm{RMS},i}$, and the center frequencies f_i for channels $i \in [I]$ are fed to the first-stage of the proposed algorithm as inputs. The first stage has three parts. In the first part, the

clusters for both the channels are generated independently. In the second part, we replace several clusters in one of the channels by the clusters of the other channel. The first two parts ensure that there are a few correlated as well as a few independent clusters in the channels. Finally, in the third part frequency dependent perturbations are added to the clusters of one of the channels. This is to imitate the effect that the correlated clusters in the two channels may have a time/angle offset.

Part 1: (Generation) The algorithm initially generates the mean time delays and mean AoAs/AoDs for all the clusters in both channels i.e., $\{\tau_{c,i}, \theta_{c,i}, \phi_{c,i}\}$. The set of the three parameters $\{\tau_{c,i}, \theta_{c,i}, \phi_{c,i}\}$ corresponding to a cluster is referred to as the cluster parameter set. The clusters for both channels are generated independently.

Part 2: (Replacement) We replace several clusters in one channel with the clusters of the other to ensure correlated clusters in the channels. The exact number of replaced clusters varies in each realization. The replacement step is to be carried in accordance with the following observations: (i) the late arriving clustered paths are more likely to fade independently across the two channels [92, 93]; and (ii) independent clustered paths are more likely as the percent frequency separation increases. In other words, for fixed percent frequency separation, the early arriving clustered paths are correlated across the channels with a higher likelihood. We store the indices of correlated clusters in sets $\mathcal{R}_i$, henceforth called the replacement index sets. As an example, the index sets can be created by sorting the cluster parameter sets in an ascending

order with respect to $\tau_{c,i}$ and populating $\mathcal{R}_i = \{i : \xi > \frac{|f_i - f_{[[I]\setminus i]}|}{\max(f_i, f[[I]\setminus i])} \frac{\tau_{c,i}}{\tau_{\mathrm{DS},i}}\}$, where $\tau_{\mathrm{DS},i} = \max_c(\tau_{c,i})$ is the delay spread of the channel. Here ξ is a standard Uniform random variable, i.e., $\xi \sim U[0,1]$. For the candidate indices that appear in $\mathcal{R}_1$ and $\mathcal{R}_2$, we replace the corresponding clusters in one channel with those of the other. To be specific, we replace the clusters of the channel with larger delay spread. Hence, we update the cluster parameters sets $\{\tau_{c,b}, \theta_{c,b}, \phi_{c,b}\}$ for all $c_b \in \mathcal{R}_b \cap \mathcal{R}_{[I]\setminus b}$ with $\{\tau_{c,[I]\setminus b}, \theta_{c,[I]\setminus b}, \phi_{c,[I]\setminus b}\}$ for all $c_{[I]\setminus b} \in \mathcal{R}_b \cap \mathcal{R}_{[I]\setminus b}$, where $b = \arg\max_i \tau_{\mathrm{DS},i}$.

Part 3: (Perturbation) So far we have simulated the effect that there will be correlated as well as independent clusters in the channels at two frequencies. Now we need to add frequency dependent perturbation in the clusters of one of the channels to simulate the behavior that correlated clusters can have some time/angle offset. The perturbation should be: (i) proportional to the mean time delay of the cluster [92, 93]; and (ii) proportional to percent center frequency separation. We continue by assuming that the clusters of the channel b are perturbed. A scalar perturbation $\Delta_{c,b}$ is generated for all $c_b \in [C_b]$. The perturbation $\Delta_{c,b}$ is then modified for delays and AoAs/AoDs using deterministic modifiers $g_\tau(\cdot)$, $g_\theta(\cdot)$ and $g_\phi(\cdot)$, respectively. The rationale of using deterministic modifications of the same perturbation for delays and angles is the coupling of these parameters in the physical channels. This is to say that the amount of variation in the mean delay of the cluster, from one frequency to another, is not expected to be independent of the variation in

AoA/AoD. Let us define the function

$$q(x,w,y,z) = \begin{cases} 1 & \text{if } x - w < y, \\ -1 & \text{if } x + w > z, \\ \pm 1 \text{ with equal probability} & \text{otherwise.} \end{cases} \tag{2.20}$$

With this definition, an example perturbation model could be $\Delta_{c,b} \sim U[0,1]$, $g_\tau(\Delta_{c,b}) = q(\tau_{c,b}, \Delta_{c,b}, 0, \tau_{\mathrm{DS},b}) \frac{|f_b - f_{[I]\setminus b}|}{\max(f_b, f_{[I]\setminus b})} \tau_{c,b} \Delta_{c,b}$ and $g_\theta(\Delta_{c,b}) = q(\theta_{c,b}, \Delta_{c,b}, 0, 2\pi) \frac{|f_b - f_{[I]\setminus b}|}{\max(f_b, f_{[I]\setminus b})} \frac{\tau_{c,b}}{\tau_{\mathrm{DS},b}} \Delta_{c,b}$. The modifier g_ϕ can be chosen similar to g_θ. The modified perturbations $g_\tau(\Delta_{c,b})$, $g_\theta(\Delta_{c,b})$, and $g_\phi(\Delta_{c,b})$ are added in $\tau_{c,b}$, $\theta_{c,b}$, and $\phi_{c,b}$, respectively, to obtain the cluster parameters for channel b. Finally, the cluster parameter sets for both channels are returned.

Algorithm 2 Mean time delays $\tau_{c,i}$ and mean AoAs/AoDs $\{\theta_{c,i}, \phi_{c,i}\}$ generation

Input: $C_i, \tau_{\mathrm{RMS},i}, f_i$ for all $i \in [I]$
Output: $\{\tau_{c,i}, \theta_{c,i}, \phi_{c,i}\}$ for all $c_i \in [C_i]$ and $i \in [I]$

1: Draw $\bar{\tau}_{c,i} \sim \tau_{\mathrm{RMS},i} \ln(\mathcal{N}(0,1)), \{\theta_{c,i}, \phi_{c,i}\} \sim U[0, 2\pi)$ for all $c_i \in [C_i]$ and $i \in [I]$. Get $\tau_{c,i} \leftarrow \bar{\tau}_{c,i} - \min_c(\bar{\tau}_{c,i})$. Generate the cluster parameter sets $\{\tau_{c,i}, \theta_{c,i}, \phi_{c,i}\}$ for all $c_i \in [C_i]$ and $i \in [I]$.
2: Populate replacement index sets $\mathcal{R}_i$ for all $i \in [I]$ using a suitable replacement model, and update $\{\tau_{c,b}, \theta_{c,b}, \phi_{c,b}\}$ for all $c_b \in \mathcal{R}_b \cap \mathcal{R}_{[I]\setminus b} \leftarrow \{\tau_{c,[I]\setminus b}, \theta_{c,[I]\setminus b}, \phi_{c,[I]\setminus b}\}$ for all $c_{[I]\setminus b} \in \mathcal{R}_b \cap \mathcal{R}_{[I]\setminus b}$, where $b = \arg\max_i \tau_{\mathrm{DS},i}$.
3: Generate C_b perturbations $\Delta_{c,b}$ and update $\tau_{c,b} \leftarrow \tau_{c,b} + g_\tau(\Delta_{c,b})$, $\theta_{c,b} \leftarrow \theta_{c,b} + g_\theta(\Delta_{c,b})$, and $\phi_{c,b} \leftarrow \phi_{c,b} + g_\phi(\Delta_{c,b})$.

2.6.2.2 Second Stage

Once the parameters $\{\tau_{c,i}, \theta_{c,i}, \phi_{c,i}\}$ for all $c_i \in [C_i]$ and $i \in [I]$ are available, the paths/rays within the clusters are generated independently for both channels in the second stage of the proposed algorithm. The second

stage requires the number of paths per cluster $R_{c,i}$, the RMS time spread of the paths within clusters $\sigma_{\tau_{r_{c,i}}}$, and the RMS AS of the relative arrival and departure angle offsets $\{\sigma_{\vartheta_{c,i}}, \sigma_{\varphi_{c,i}}\}$, as input. The output of the second stage are the sets $\{\alpha_{r_{c,i}}, \tau_{r_{c,i}}, \vartheta_{r_{c,i}}, \varphi_{r_{c,i}}\}$ for all $r_{c,i} \in R_{c,i}$ and $i \in [I]$. The relative time delays $\tau_{r_{c,i}}$ are generated according to a suitable intra-cluster PDP (e.g., Exponential or Uniform), the relative angle shifts $\{\vartheta_{r_{c,i}}, \varphi_{r_{c,i}}\}$ according to a suitable APS (e.g., uniform, truncated Gaussian or truncated Laplacian), and the complex coefficients $\alpha_{r_{c,i}}$ according to a suitable fading model (e.g., Rayleigh or Ricean).

2.7 Simulation Results

In this section, we present simulation results for the proposed channel simulation strategy and performance of the proposed out-of-band aided mmWave beam-selection strategies. We start by presenting the channel parameters and results, and subsequently present the system parameters and the results for the proposed out-of-band aided mmWave beam-selection strategies.

2.7.1 Channel simulation

The sub-6 GHz channel is centered at $\underline{f} = 3.5$ GHz with 150 MHz bandwidth, and the mmWave channel is centered at $f = 28$ GHz with 850 MHz bandwidth. The bandwidths are maximum available bandwidths in the respective bands [99, 100]. The sub-6 GHz and mmWave channels have $\underline{C} = 10$ and $C = 5$ clusters respectively, each contributing $\underline{R}_{\mathrm{c}} = R_{\mathrm{c}} = 20$ rays.

The mean AoAs/AoDs of the clusters are limited to $[-\frac{\pi}{3}, \frac{\pi}{3})$. The relative AoA/AoD shifts come from a wrapped Gaussian distribution with with AS $\{\underline{\sigma}_{\underline{\vartheta}_{\underline{c}}}, \underline{\sigma}_{\underline{\varphi}_{\underline{c}}}\} = 4^\circ$ and $\{\sigma_{\vartheta_c}, \sigma_{\varphi_c}\} = 2^\circ$. As the delay spread of sub-6 GHz channel is expected to be larger than the delay spread of mmWave [86, 87, 88, 89], we choose $\underline{\tau}_{\mathrm{RMS}} \approx 3.8$ ns and $\tau_{\mathrm{RMS}} \approx 2.7$ ns. The relative time delays of the paths within the clusters are drawn from zero mean normal distributions with RMS AS $\underline{\sigma}_{\underline{\tau}_{r_{\underline{c}}}} = \frac{\underline{\tau}_{\mathrm{RMS}}}{10}$ and $\sigma_{\tau_{r_c}} = \frac{\tau_{\mathrm{RMS}}}{10}$. The powers of the clusters are drawn from exponential distributions. Specifically, the exponential distribution with parameter μ is defined as $f(x|\mu) = \frac{1}{\mu} e^{-\frac{x}{\mu}}$. The parameter for sub-6 GHz was chosen as $\underline{\mu} = 0.2$ and for mmWave $\mu = 0.1$. This implies that the power in late arriving multi-paths for mmWave will decline more rapidly than sub-6 GHz. We use the replacement and perturbation models described in Section 2.6 with the angle modifier adjusted to limit the angles in $[-\frac{\pi}{3}, \frac{\pi}{3})$. An example realization of the channel with this configuration is shown in Fig. 2.10.

2.7.2 Out-of-band aided compressed beam-selection

In this subsection, we present simulation results to test the performance of the proposed out-of-band aided mmWave beam-selection strategies. The sub-6 GHz system has $\underline{M}_{\mathrm{RX}} = 8$ and $\underline{M}_{\mathrm{TX}} = 2$ antennas and the mmWave system has $M_{\mathrm{RX}} = 64$ and $M_{\mathrm{TX}} = 16$ antennas. Both systems use ULAs with half wavelength spacing $\underline{d} = d = 1/2$. The number of sub-6 GHz OFDM subcarriers is $\underline{K} = 32$ and mmWave OFDM subcarriers is $K = 128$. The CP length is quarter quarter the symbol duration for both sub-6 GHz and

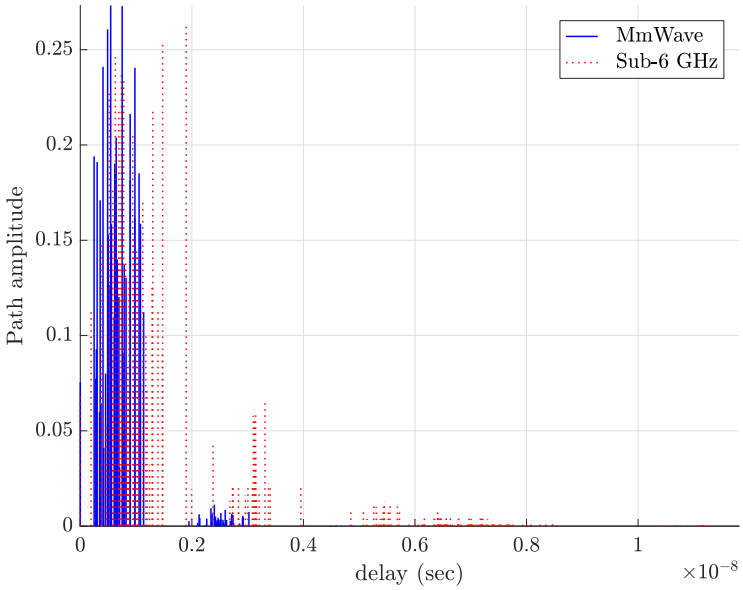

(a) Delayed paths at sub-6 GHz and mmWave

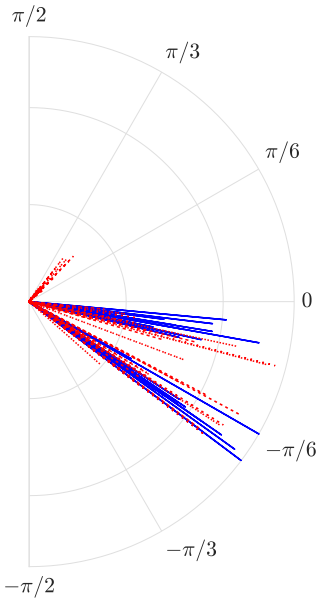

(b) AoAs at sub-6 GHz and mmWave

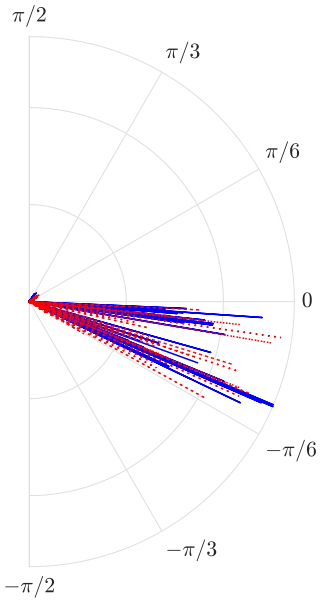

(c) AoDs at sub-6 GHz and mmWave

Figure 2.10: An example realization generated using the proposed channel generation strategy.

mmWave. With the chosen operating frequencies, the number of antennas, and the inter-element spacing, the array aperture for sub-6 GHz and mmWave arrays is the same. The transmission power for sub-6 GHz system was set to $\underline{P}_{\mathrm{t}} = 30 - 10\log_{10}(\underline{M}_{\mathrm{TX}})$ dBm per 25 MHz of bandwidth [101]. The subtraction of $10\log_{10}(\underline{M}_{\mathrm{TX}})$ takes care of antenna array gain. The transmission power for mmWave system was set to $P_{\mathrm{t}} = 43 - 10\log_{10}(M_{\mathrm{TX}})$ dBm [102]. These power values are based on Federal Communications Commission (FCC) proposals [101, 102]. The path-loss coefficient at sub-6 GHz and mmWave is 3. The number of taps in sub-6 GHz and mmWave is one more than the length of CP, i.e., $\underline{L} = 9$ and $L = 33$ taps. The raised cosine filter with a roll off factor of 1 is used as a pulse shaping filter.

The metric used for performance comparison is the effective achievable rate R_{eff} defined as

$$R_{\mathrm{eff}} = \frac{\eta}{EK}\sum_{e=1}^{E}\sum_{k=1}^{K}\log_2\left(1 + \frac{P_{\mathrm{t}}}{K\sigma_{\hat{\mathbf{v}}}^2}|\mathbf{z}_{\hat{i}}^{*}\mathbf{H}[k]\mathbf{w}_{\hat{j}}|^2\right), \tag{2.21}$$

where $\{\hat{i}, \hat{j}\}$ are the estimated transmit and receive codeword indices, E is the number of independent trials for ensemble averaging, $\eta \triangleq \max(0, 1 - \frac{N_{\mathrm{RX}} \times N_{\mathrm{TX}}}{T_{\mathrm{c}}})$, and T_{c} is the channel coherence time in OFDM blocks. Note that, the coherence time can be defined in the units of time, as well as in the units of OFDM blocks as in [103]. With the channel coherence of T_{c} blocks and a training of $N_{\mathrm{RX}} \times N_{\mathrm{TX}}$ blocks, $1 - \frac{N_{\mathrm{RX}} \times N_{\mathrm{TX}}}{T_{\mathrm{c}}}$ is the fraction of time/blocks that are used for data transmission. Thus, η captures the loss in achievable rate due to the training.

In the first experiment, we test the performance of out-of-band aided compressed beam-selection in comparison with in-band only compressed beam-selection. The TX-RX separation for this experiment is fixed at 60 m. The compressed beam-selection is performed using information on a single subcarrier, chosen uniformly at random from the K subcarriers. The number of independent trials is $E = 2000$. The number of measurements for exhaustive-search are fixed at $64 \times 16 = 1024$. The rate results as a function of the number of measurements $N_{\mathrm{RX}} \times N_{\mathrm{TX}}$ are shown in Fig. 2.11. It can be observed that throughout the range of interest the out-of-band aided compressed beam-selection using structured LW-OMP has a better effective rate in comparison with OMP. Note that the results are presented for a specific coherence time $T_{\mathrm{c}} = 128(M_{\mathrm{RX}} \times M_{\mathrm{TX}})$ given in OFDM blocks. The beam coherence time (i.e., the time in which the beams do not need to be updated) of the mmWave channels could be from tens of milliseconds to hundreds of milliseconds depending on several parameters. Further, note that the OFDM symbol time at mmWave can be as low as a few microseconds. Considering 4 µs symbol duration, (i.e., possible in 5G NR [104]), we get $128(M_{\mathrm{RX}} \times M_{\mathrm{TX}}) \times 4\,\mu\mathrm{s} \approx 0.5\,\mathrm{s}$. So a coherence time of $T_{\mathrm{c}} = 128(M_{\mathrm{RX}} \times M_{\mathrm{TX}})$ blocks implies a channel that is relatively less dynamic.

It is observed from Fig. 2.11 that the effective rate of structured LW-OMP only reaches the rate of exhaustive-search. This, however, is true for large channel coherence T_{c} values. We plot the effective rate of the proposed structured LW-OMP based compressed beam-selection for three chan-

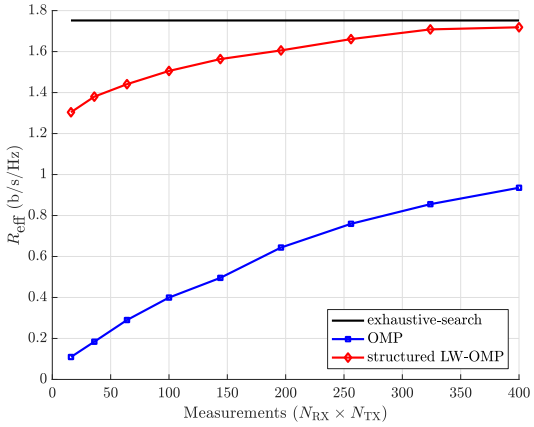

Figure 2.11: Effective rate of the structured LW-OMP approach versus the number of measurements $N_{\text{RX}} \times N_{\text{TX}}$ with 60 m TX-RX separation and $T_{\text{c}} = 128(M_{\text{RX}} \times M_{\text{TX}})$ blocks.

nel coherence values in Fig. 2.12. These values are $128(M_{\text{RX}} \times M_{\text{TX}}) \approx 0.5\,\text{s}$, $32(M_{\text{RX}} \times M_{\text{TX}}) \approx 0.13\,\text{s}$, and $4(M_{\text{RX}} \times M_{\text{TX}}) \approx 16\,\text{ms}$. So these coherence times represent channels that are less-dynamic to highly-dynamic. As the coherence time of the channel decreases, the advantage of the proposed approach becomes significant. As an example, for a medium channel coherence time i.e., $32(M_{\text{RX}} \times M_{\text{TX}})$, the proposed structured LW-OMP based compressed beam-selection can reduce the training overhead of exhaustive-search by over 4x. The gains for smaller channel coherence times are more pronounced. Therefore, the proposed approach is suitable for applications with rapidly varying channels e.g., V2X communications.

To study the fraction of times the proposed approach recovers the best beam-pair, we define and evaluate the success percentage of the proposed

approach. The success percentage is defined as

$$\text{SP} = \frac{1}{E}\sum_{e=1}^{E} |\hat{r}^{\star} \cap \mathcal{B}_N|, \tag{2.22}$$

where $\hat{r}^{\star}$ is the index estimated by the proposed approach and $\mathcal{B}_N$ is the set containing the actual indices corresponding to the N best TX/RX beam-pairs. When $N = 1$, the set $\mathcal{B}_1$ has only one element and that is the index corresponding to the beam-pair with the highest receive power. For $N > 1$, the set has N entries that are indices corresponding to the N beam-pairs with the highest receive power. Using a set of indices, instead of the index corresponding to the best beam-pair, generalizes the study and reveals an interesting behavior about selecting one of the better beam-pairs in comparison with selecting the best beam-pair. For now, note that due to the spread of each cluster and the presence of multiple clusters in the mmWave channel, it is possible that the proposed approach does not recover the best beam-pair and still manages to provide a decent effective rate. We populate the set $\mathcal{B}_N$ by performing exhaustive-search in a noiseless channel. We do so as the exhaustive-search in a noisy channel is itself subject to errors. This behavior is revealed in Fig. 2.13, where the exhaustive-search succeeds $\approx 42\%$ of the times for $\mathcal{B}_1$ and $\approx 58\%$ of the times for $\mathcal{B}_5$. The success percentage of the proposed structured LW-OMP algorithm is $\approx 57\%$ for $\mathcal{B}_1$ and $\approx 30\%$ for $\mathcal{B}_5$. The high success percentage for $\mathcal{B}_5$ is a ramification of having several strong candidate beam-pairs due to cluster spread and the presence of multiple clusters. Note that even though the proposed approach has a (slightly) inferior success percentage for $\mathcal{B}_5$ compared with the exhaustive-search, the training overhead of the proposed approach is

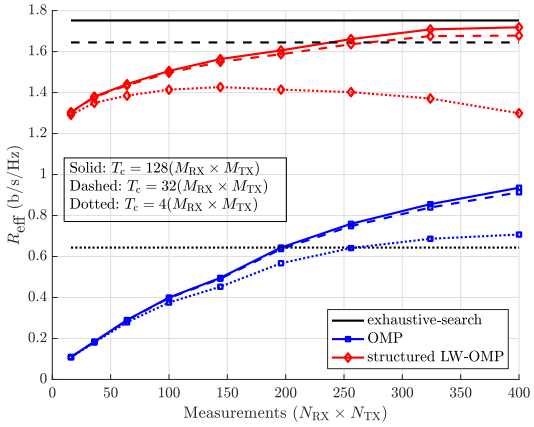

Figure 2.12: Effective rate of the structured LW-OMP approach versus the number of measurements $N_{\mathrm{RX}} \times N_{\mathrm{TX}}$ with 60 m TX-RX separation and three different channel coherence times T_{c}.

significantly lower. With the overhead factored in, the proposed approach is advantageous compared to exhaustive-search as evidenced by the effective rate results in Fig. 2.12.

Outdated channel information as side-information: The proposed out-of-band aided strategies can be used to reduce the overhead of beam-selection in the initial access. If, however, the link is already established, it may be possible to use the past channel information as a side-information about the mmWave channel. To this end, we study the use of past channels as side-information in mmWave beam-selection. Note that, the channel generation strategy proposed earlier does not incorporate time-evolution of the channel. This is to say that, the proposed strategy generates a pair of mmWave and a sub-6 GHz channel. When recalled, the strategy generates another pair that is completely independent of the first pair. As the new channel

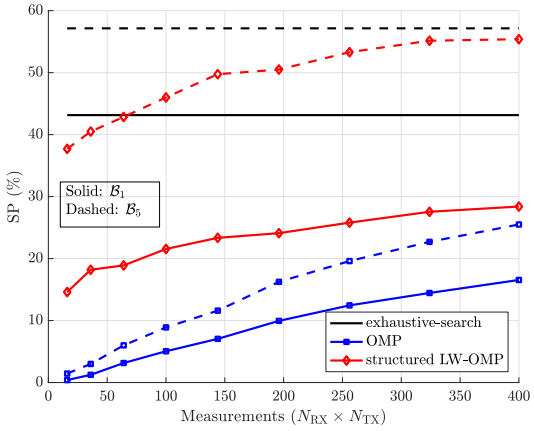

Figure 2.13: Success percentage of the structured LW-OMP approach versus the number of measurements $N_{\mathrm{RX}} \times N_{\mathrm{TX}}$ with 60 m TX-RX separation.

is completely independent of the previous channel, it does not contain any information about the previous channel. To introduce some sort of continuity in time-evolution of the channels, we use the strategy explained in Fig. 2.14. The main idea is to generate two independent channels, and assume that they represent independent states of the mmWave channel at time t_0 and t_1. Then the channels at time instances between t_0 and t_1 are generated by linearly interpolating the channel at time t_0 and t_1. Specifically, let the channel at time 0 be $\mathbf{H}_0$ and the channel at time t_1 be $\mathbf{H}_1$, then the channel at time t is

$$\mathbf{H}_t = (1-t)\mathbf{H}_0 + t\mathbf{H}_1, \text{ for } t \in [0,1]. \tag{2.23}$$

It is expected that if the channel $\mathbf{H}_t$ is known, then side-information is more relevant when t is close to 1 and less relevant if t is close to 0. Therefore we study the performance of structured LW-OMP as a function of t i.e., the age

of channel information that is available. To this end, we use the perfect knowledge case, where $\mathbf{H}_t$ is known perfectly and is used in structured LW-OMP. This case, however, is not practical. Note that in an mmWave system the older channels will also be observed/recovered under the hardware constraints that make accurate channel acquisition difficult. For the in-band mmWave training, compressed sensing based beam-selection is used to acquire the dominant direction. Thus, only the dominant direction of $\mathbf{H}_t$ recovered through OMP algorithm will be available in practice. Therefore, we also study this practical case. The results of this experiment are shown in Fig. 2.15. We can see that as t increases, the performance of outdated information assisted strategies improve. It is, however, only with perfect CSI knowledge that outdated channel information can clearly outperform the out-of-band assisted strategies. For the practical case where only angle information is available, the outdated information assisted strategy does not perform better than the inband only strategy.

Next, we evaluate the performance of structured LW-SOMP based compressed beam-selection using information from all active subcarriers. The TX-RX separation is 60 m. The results of this experiment are shown in Fig. 2.16. The structured LW-SOMP achieves a better effective rate in comparison with LW-SOMP. Due to the use of training information from all subcarriers, both structured LW-SOMP and LW-SOMP reach the effective rate of exhaustive-search with a handful of measurements. For low channel coherence times T_{c}, the compressed beam-selection approaches, especially out-of-band aided com-

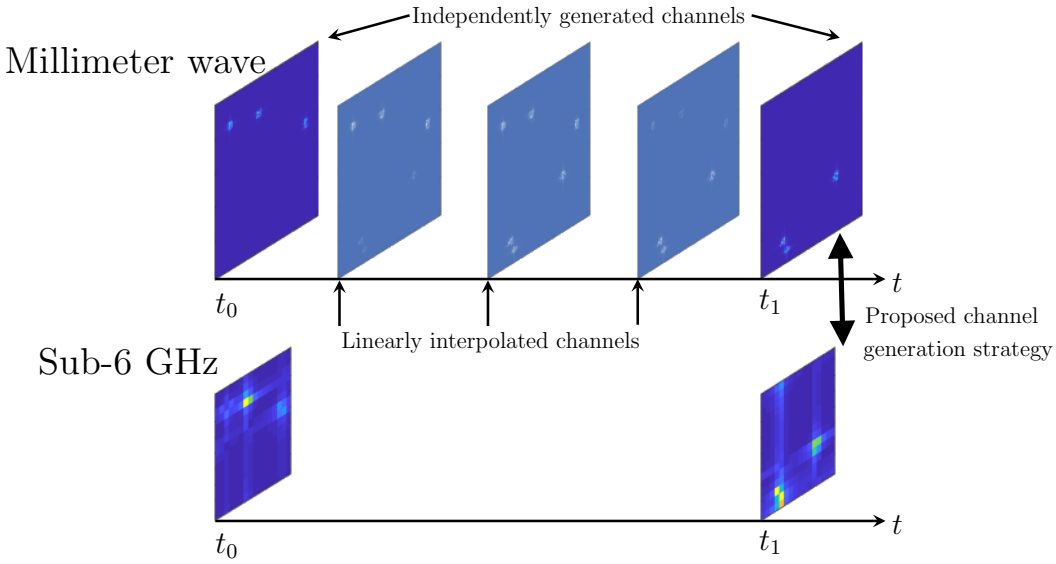

Figure 2.14: Modification of the proposed channel generating strategy to generate a time evolution of the mmWave channel. The main idea is to generate two independent channels and considering them to be independent realizations of the mmWave channel at time t_0 and time t_1. Then the channels between t_0 and t_1 are generated via linear interpolation of the channels at time t_0 and t_1.

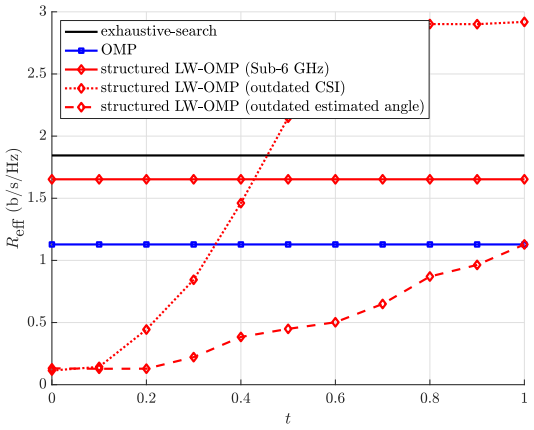

Figure 2.15: The effective rate of the structured LW-SOMP approach versus the time t. The time t here represents the time at which the channel state was observed and used as side information. The TX-RX separation is 60 m.

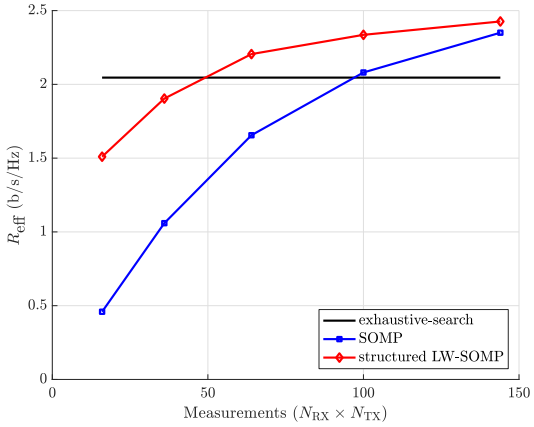

Figure 2.16: Effective rate of the structured LW-SOMP approach versus the number of measurements $N_{\text{RX}} \times N_{\text{TX}}$ with 60 m TX-RX separation and $T_{\text{c}} = 32(M_{\text{RX}} \times M_{\text{TX}})$ blocks.

pressed beam-selection, will outperform exhaustive-search.

Finally, note that if the proposed strategy is used in the initial access, we can only start training the mmWave system, once the sub-6 GHz channel has been observed. As such, there is some delay in the starting point of the proposed strategy compared to in-band only training e.g., exhaustive search. Furthermore, the sub-6 GHz symbols are longer than the mmWave symbols. Therefore it is important to understand the total delay incurred by the proposed strategy in comparison with in-band only training. We perform this comparison in Fig. 2.17. Note that there are 2 transmit and 8 receive antennas in sub-6 GHz system. Further, there are 16 transmit and 64 receive antennas in the mmWave system. We assume that the sub-6 GHz symbol duration is 66 µs, and the mmWave symbol duration is 4 µs [104]. At sub-6 GHz, the channel from a transmit antenna to all the receive antennas can be

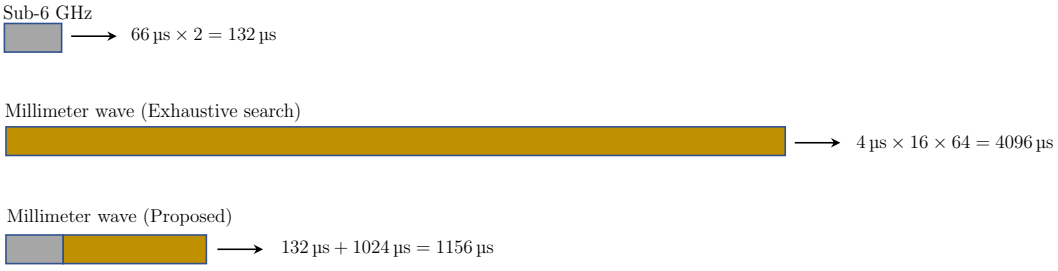

Figure 2.17: Delay of the proposed strategy in comparison with exhaustive search assuming 4 µs symbol duration for the mmWave symbol and 66 µs symbol duration for the sub-6 GHz symbol.

estimated in a single transmission. As transmissions from two transmit antennas can be completed in two symbol durations, the total training time for sub-6 GHz system is $66\,\mu s \times 2 = 132\,\mu s$. For exhaustive search at mmWave, 64×16 symbols are required, and each has duration $4\,\mu s$, so the total time is $4\,\mu s \times 16 \times 64 = 4096\,\mu s$. In comparison, for the proposed strategy, first there is $132\,\mu s$ delay for sub-6 GHz channel estimation and then there is approximately $1024\,\mu s$ training time for compressed beam-selection at mmWave. We got this approximate training time from an earlier experiment, where we noted that the proposed strategy has one-fourth the training overhead of the exhaustive-search. This implies that the total training time for the proposed strategy is $132\,\mu s + 1024\,\mu s = 1156\,\mu s$, which is substantially less than the training time of in-band only exhaustive search.

2.8 Conclusion

In this chapter, we used the sub-6 GHz spatial information to reduce the training overhead of beam-selection in an analog mmWave system. We

formulated the compressed beam-selection problem with the codebooks generated from low-resolution phase-shifters. We used a weighted sparse recovery approach with structured random codebooks to incorporate out-of-band information. We proposed a method to generate multi-band frequency dependent channels according to the frequency dependent channel behavior observed in the prior work. We used the proposed multi-band frequency dependent channels to evaluate the achievable rate of the proposed approach. From the rate results, we concluded that the training overhead of in-band only compressed beam-selection can be reduced substantially if out-of-band information is used.

Chapter 3

Millimeter Wave Covariance Estimation Using Sub-6 GHz Information

In this chapter, we propose two mmWave covariance estimation strategies. First, we propose a sub-6 GHz covariance translation strategy to obtain mmWave channel covariance directly from sub-6 GHz. Second, we formulate the problem of covariance estimation for hybrid MIMO systems as a compressed signal recovery problem. To incorporate sub-6 GHz information in the proposed formulation, we introduce the concept of weighted compressed covariance estimation (similar to weighted sparse signal recovery [38]). The weights in the proposed approach are chosen based on the sub-6 GHz information. Finally, we quantify the loss in received post-processing SNR due to the use of imperfect covariance estimates. This work was published in [45] and [46][1] (©IEEE).

[1]This chapter is based on A. Ali, N. González-Prelcic, and R. W. Heath Jr., "Spatial Covariance Estimation for Millimeter Wave Hybrid Systems using Out-of-Band Information," *IEEE Trans. Wireless Commun.*, 2019, (early access). A. Ali formulated the problem, conducted the numerical experiments, and wrote the initial draft of the manuscript. N. González-Prelcic and R. W. Heath Jr. provided critical feedback and helped shape the research and manuscript.

3.1 Motivation and prior work

The hybrid precoders/combiners for millimeter wave (mmWave) MIMO systems are typically designed based on either instantaneous channel state information (CSI) [18] or statistical CSI [19]. Obtaining channel information at mmWave is, however, challenging due to: (i) the large dimension of the arrays used at mmWave, (ii) the hardware constraints (e.g., a limited number of RF-chains [18, 19], and/or low-resolution analog-to-digital converters (ADCs) [105]), and (iii) low pre-beamforming signal-to-noise ratio (SNR). The reasons for low pre-beamforming SNR at mmWave are twofold: (i) the antenna size is small which in turn means less received power, and (ii) the thermal noise is high due to large bandwidth. We exploit out-of-band information extracted from sub-6 GHz channels to configure the mmWave links. The use of sub-6 GHz information for mmWave is enticing as mmWave systems will likely be used in conjunction with sub-6 GHz systems for multi-band communications and/or to provide wide area control signals [29, 30, 31].

Using out-of-band information can positively impact several applications of mmWave communications. In mmWave cellular [1, 4], the base-station user-equipment separation can be large (e.g., on cell edges). In such scenarios, link configuration is challenging due to poor pre-beamforming SNR and user mobility. The pre-beamforming SNR is more favorable at sub-6 GHz due to lower bandwidth. Therefore, reliable out-of-band information from sub-6 GHz can be used to aid the mmWave link establishment. Similarly, frequent reconfiguration will be required in highly dynamic channels experienced in

mmWave vehicular communications (see e.g., [10] and the references therein). The out-of-band information (coming e.g., from dedicated short-range communication (DSRC) channels [13]) can play an important role in unlocking the potential of mmWave vehicular communications.

We propose two mmWave covariance estimation strategies. The first strategy is covariance translation from sub-6 GHz to mmWave, while the second strategy is out-of-band aided compressed covariance estimation. In this section, we review the prior work relevant to each approach.

Most of the prior work on covariance translation was tailored towards frequency division duplex (FDD) systems [106, 107, 47, 59, 108]. The prior work includes least-squares based [106], minimum variance distortionless response based [107], and [108] projection based strategies. In [47], a spatio-temporal covariance translation strategy was proposed based on two-dimensional interpolation. In [59], a training based covariance translation approach was presented. Unlike [106, 107, 47], the translation approach in [59] requires training specifically for translation but does not assume any knowledge of the array geometry. The uplink (UL) information has also been used in estimating the instantaneous downlink (DL) channel [61, 62]. In [61], the multi-paths in the UL channel were separated and subsequently used in the estimation of the DL channel. The UL measurements were used to obtain weights for the compressed sensing based DL channel estimation in [62].

In FDD systems, the number of antennas in the UL and DL array is typically the same, and simple correction for the differences in array response

due to slightly different wavelengths can translate the UL covariance to DL. MmWave systems, however, will use a larger number of antennas in comparison with sub-6 GHz, and conventional translation strategies (as in [106, 107, 47, 59, 108, 61, 62]) are not applicable. Further, the frequency separation between UL and DL is typically small (e.g., there is 9.82% frequency separation between 1935 MHz UL and 2125 MHz DL [58]) and spatial information is congruent. We consider channels that can have frequency separation of several hundred percents, and hence some degree of spatial disagreement is expected.

To our knowledge, there is no prior work that uses the out-of-band information to aid the in-band mmWave covariance estimation. Some other out-of-band aided mmWave communication methodologies, however, have been proposed. In [64], coarse angle estimation at sub-6 GHz followed by refinement at mmWave was proposed. In [63], the legacy WiFi measurements were used to configure the 60 GHz WiFi links. The measurement results presented in [63] demonstrated the benefits and practicality of using out-of-band information for mmWave communications. In [31], a scheduling strategy for joint sub-6 GHz-mmWave communication system was introduced to maximize the delay-constrained throughput of the mmWave system. In [34], radar aided mmWave communication was introduced. Specifically, the mmWave radar covariance was used directly to configure mmWave communication beams.

The algorithms in [64, 31] were designed specifically for analog architectures. We consider a more general hybrid analog-digital architecture. Only LOS channels were considered in [63], whereas the methodologies proposed

in this chapter are applicable to NLOS channels. Radar information (coming from a band adjacent to the mmWave communication band) is used in [34]. We, however, use information from a sub-6 GHz communication band as out-of-band information.

The analysis in the chapter uses singular vector perturbation theory [42] to quantify the loss in received SNR when the covariance estimate is imperfect. The prior work on mmWave covariance estimation in [109, 110, 50] is based on compressed sensing, and the analysis is based on mutual coherence of the sensing matrices [50]. We analyze SNR degradation using singular vector perturbation theory as the analysis generalizes to both mmWave covariance estimation strategies proposed in this chapter.

3.2 Contributions

The main contributions of this chapter are as follows:

- We propose an out-of-band covariance translation strategy for MIMO systems. The proposed translation approach is based on a parametric estimation of the mean angle and angle spread (AS) of all clusters at sub-6 GHz. The estimated parameters are then used in the theoretical expressions of the spatial covariance at mmWave to complete the translation.

- We formulate the problem of covariance estimation for mmWave hybrid MIMO systems as a compressed signal recovery problem. To incorpo-

rate out-of-band information in the proposed formulation, we introduce the concept of weighted compressed covariance estimation (similar to weighted sparse signal recovery [38]). The weights in the proposed approach are chosen based on the out-of-band information.

- We use tools from singular vector perturbation theory [42] to quantify the loss in received post-processing SNR due to the use of imperfect covariance estimates. The singular vector perturbation theory has been used for robust bit-allocation [43] and robust block-diagonalization [44] in MIMO systems. For SNR degradation analysis, we consider a single path channel and find an upper and lower bound on the loss in SNR. The resulting expressions permit a simple and intuitive explanation of the loss in terms of the mismatch between the true and estimated covariance.

The rest of the chapter is organized as follows. In Section 3.3, we provide the system and channel models for sub-6 GHz and mmWave. We present the out-of-band covariance translation in Section 3.4 and out-of-band aided compressed covariance estimation in Section 3.5. In Section 3.6, we analyze the SNR degradation. We present the simulation results in Section 3.7, and in Section 3.8, we compare the proposed covariance estimation strategies. Finally, the conclusions are presented in Section 3.9.

3.3 System, channel and, covariance models

We consider a single-user multi-band MIMO system, shown in Fig. 3.1, where the sub-6 GHz and mmWave systems operate simultaneously. We consider uniform linear arrays (ULAs) of isotropic point-sources at the TX and the RX. The strategies proposed in this work can be extended to other array geometries with suitable modifications. The sub-6 GHz and mmWave arrays are co-located, aligned, and have comparable apertures.

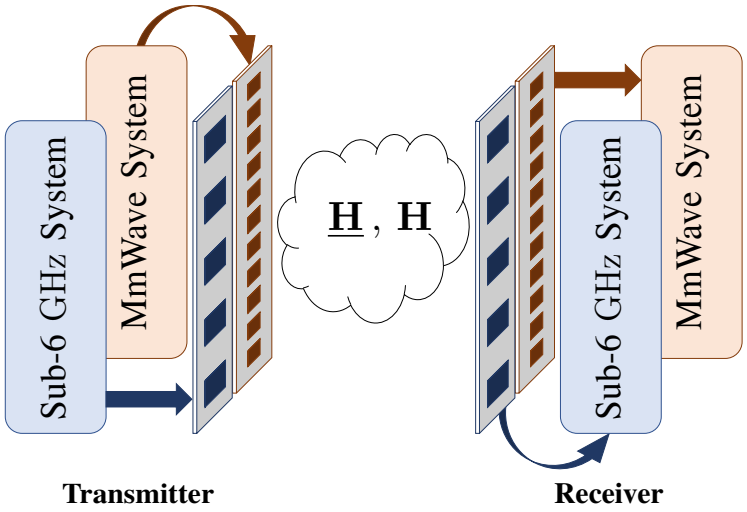

Figure 3.1: The multi-band MIMO system with co-located sub-6 GHz and mmWave antenna arrays. The sub-6 GHz channel is denoted $\underline{\mathbf{H}}$ and the mmWave channel is denoted $\mathbf{H}$.

3.3.1 Millimeter wave system model

The mmWave system is shown in Fig. 3.2. The TX has N_{TX} antennas and $M_{\mathrm{TX}} \leq N_{\mathrm{TX}}$ RF-chains, whereas the RX has N_{RX} antennas and $M_{\mathrm{RX}} \leq N_{\mathrm{RX}}$ RF-chains. We assume that $N_{\mathrm{s}} \leq \min\{M_{\mathrm{TX}}, M_{\mathrm{RX}}\}$ data-streams

are transmitted. We consider OFDM transmission with K sub-carriers. The transmission symbols on sub-carrier k are denoted as $\mathbf{s}[k] \in \mathbb{C}^{N_\mathrm{s}\times 1}$, and follow $\mathbb{E}[\mathbf{s}[k]\mathbf{s}^*[k]] = \frac{P}{KN_\mathrm{s}}\mathbf{I}_{N_\mathrm{s}}$, where P is the total average transmitted power. The data-symbols $\mathbf{s}[k]$ are first precoded using the baseband-precoder $\mathbf{F}_{\mathrm{BB}}[k] \in \mathbb{C}^{M_{\mathrm{TX}}\times N_\mathrm{s}}$, then converted to time-domain using M_{TX} K-point IDFTs. Cyclic-prefixes (CPs) are then prepended to the time-domain samples before applying the RF-precoder $\mathbf{F}_{\mathrm{RF}} \in \mathbb{C}^{N_{\mathrm{TX}}\times M_{\mathrm{TX}}}$. Since the RF-precoder is implemented using analog phase-shifters, it has constant modulus entries i.e., $|[\mathbf{F}_{\mathrm{RF}}]_{i,j}|^2 = \frac{1}{N_{\mathrm{TX}}}$. Further, we assume that the angles of the analog phase-shifters are quantized and have a finite set of possible values. With these assumptions, $[\mathbf{F}_{\mathrm{RF}}]_{i,j} = \frac{1}{\sqrt{N_{\mathrm{TX}}}}e^{\mathrm{j}\zeta_{i,j}}$, where $\zeta_{i,j}$ is the quantized angle. The precoders satisfy the total power constraint $\sum_{k=1}^{K} \|\mathbf{F}_{\mathrm{RF}}\mathbf{F}_{\mathrm{BB}}[k]\|_{\mathrm{F}}^2 = KN_\mathrm{s}$.

We assume perfect time and frequency synchronization at the receiver. The received signals are first combined using the RF-combiner $\mathbf{W}_{\mathrm{RF}} \in \mathbb{C}^{N_{\mathrm{RX}}\times M_{\mathrm{RX}}}$. The CPs are then removed and the time-domain samples are converted back to frequency-domain using M_{RX} K-point DFTs. Subsequently, the frequency-domain signals are combined using the baseband combiner $\mathbf{W}_{\mathrm{BB}}[k] \in \mathbb{C}^{M_{\mathrm{RX}}\times N_\mathrm{s}}$. If $\mathbf{H}[k]$ denotes the frequency-domain $N_{\mathrm{RX}} \times N_{\mathrm{TX}}$ mmWave MIMO channel on sub-carrier k, then the post-processing received signal on sub-carrier K can be represented as

$$\begin{aligned}\mathbf{y}[k] &= \mathbf{W}_{\mathrm{BB}}^*[k]\mathbf{W}_{\mathrm{RF}}^*\mathbf{H}[k]\mathbf{F}_{\mathrm{RF}}\mathbf{F}_{\mathrm{BB}}[k]\mathbf{s}[k] + \mathbf{W}_{\mathrm{BB}}^*[k]\mathbf{W}_{\mathrm{RF}}^*\mathbf{n}[k],\\ &= \mathbf{W}^*[k]\mathbf{H}[k]\mathbf{F}[k]\mathbf{s}[k] + \mathbf{W}^*[k]\mathbf{n}[k], \end{aligned} \tag{3.1}$$

where $\mathbf{F}[k] = \mathbf{F}_{\mathrm{RF}}\mathbf{F}_{\mathrm{BB}}[k] \in \mathbb{C}^{N_{\mathrm{TX}} \times N_{\mathrm{s}}}$ is the precoder, and $\mathbf{W}[k] = \mathbf{W}_{\mathrm{RF}}\mathbf{W}_{\mathrm{BB}}[k] \in \mathbb{C}^{N_{\mathrm{RX}} \times N_{\mathrm{s}}}$ is the combiner. Finally, $\mathbf{n} \sim \mathcal{CN}(\mathbf{0}, \sigma_{\mathbf{n}}^2\mathbf{I})$ is the additive white Gaussian noise.

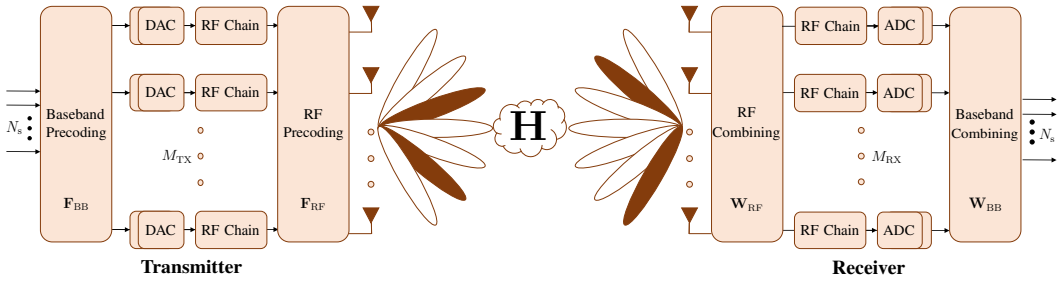

Figure 3.2: The mmWave system with hybrid analog-digital precoding.

3.3.2 Sub-6 GHz system model

The sub-6 GHz system is shown in Fig. 3.3. We underline all sub-6 GHz variables to distinguish them from the mmWave variables. Though hybrid analog-digital architectures are also interesting for sub-6 GHz systems [111], we consider a fully digital sub-6 GHz system, i.e., one RF-chain per antenna. As such, fully digital precoding is possible at sub-6 GHz. The $\underline{N}_{\mathrm{s}}$ data-streams are communicated by the TX with $\underline{N}_{\mathrm{TX}}$ antennas to the receiver with $\underline{N}_{\mathrm{RX}}$ antennas as shown in Fig. 3.3. The sub-6 GHz OFDM system has $\underline{K}$ sub-carriers.

3.3.3 Channel model

We present the channel model for mmWave, i.e., using non-underlined notation. The sub-6 GHz channel follows the same model. We adopt a wide-

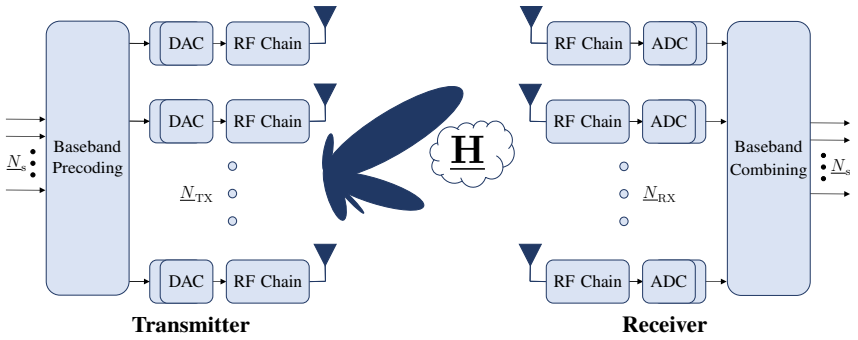

Figure 3.3: The sub-6 GHz system with digital precoding.

band geometric channel model with C clusters. Each cluster has a mean time-delay $\tau_c \in \mathbb{R}$, mean physical angle-of-arrival (AoA) and angle-of-departure (AoD) $\{\theta_c, \phi_c\} \in [0, 2\pi)$. Each cluster is further assumed to contribute R_c rays/paths between the TX and the RX. Each ray $r_c \in [R_c]$ has a relative time-delay τ_{r_c}, relative angle shift $\{\vartheta_{r_c}, \varphi_{r_c}\}$, and complex path coefficient α_{r_c} (including path-loss). Further, $p(\tau)$ denotes the combined effects of analog filtering and pulse shaping filter evaluated at point τ. Under this model, the delay-d MIMO channel matrix $\mathbf{H}[d]$ can be written as [65]

$$\mathbf{H}[d] = \sqrt{N_{\mathrm{RX}} N_{\mathrm{TX}}} \sum_{c=1}^{C} \sum_{r_c=1}^{R_c} \alpha_{r_c} p(dT_{\mathrm{s}} - \tau_c - \tau_{r_c}) \times \mathbf{a}_{\mathrm{RX}}(\theta_c + \vartheta_{r_c}) \mathbf{a}_{\mathrm{TX}}^{*}(\phi_c + \varphi_{r_c}), \tag{3.2}$$

where T_{s} is the signaling interval and $\mathbf{a}_{\mathrm{RX}}(\theta)$ and $\mathbf{a}_{\mathrm{TX}}(\phi)$ are the antenna array response vectors of the RX and the TX, respectively. The array response vector of the RX is

$$\mathbf{a}_{\mathrm{RX}}(\theta) = \frac{1}{\sqrt{N_{\mathrm{RX}}}} [1, e^{\mathrm{j}2\pi\Delta \sin(\theta)}, \cdots, e^{\mathrm{j}(N_{\mathrm{RX}}-1)2\pi\Delta \sin(\theta)}]^{\mathsf{T}}, \tag{3.3}$$

where Δ is the inter-element spacing normalized by the wavelength. The array response vector of the TX is defined in a similar manner. With the delay-d MIMO channel matrix given in (3.2), the channel at sub-carrier k, $\mathbf{H}[k]$ can be expressed as [65]

$$\mathbf{H}[k] = \sum_{d=0}^{D-1} \mathbf{H}[d] e^{-\mathrm{j}\frac{2\pi k}{K} d}, \tag{3.4}$$

where D is the number of delay-taps in the mmWave channel.

3.3.4 Covariance model

We simplify (3.4) before discussing the channel covariance model. First, we plug in the definition of $\mathbf{H}[d]$ from (3.2) in (3.4), change the order of summation, and re-arrange terms to write (3.4) as

$$\mathbf{H}[k] = \sqrt{N_{\mathrm{RX}} N_{\mathrm{TX}}} \sum_{c=1}^{C} \sum_{r_c=1}^{R_c} \Big(\sum_{d=0}^{D-1} \alpha_{r_c} p(dT_{\mathrm{s}} - \tau_c - \tau_{r_c}) e^{-\mathrm{j}\frac{2\pi k}{K} d} \Big) \times \mathbf{a}_{\mathrm{RX}}(\theta_c + \vartheta_{r_c}) \mathbf{a}_{\mathrm{TX}}^{*}(\phi_c + \varphi_{r_c}). \tag{3.5}$$

Second, we define $\bar{\alpha}_{r_c,k} = \sum_{d=0}^{D-1} \alpha_{r_c} p(dT_{\mathrm{s}} - \tau_c - \tau_{r_c}) e^{-\mathrm{j}\frac{2\pi k}{K} d}$ to rewrite (3.5) as

$$\mathbf{H}[k] = \sqrt{N_{\mathrm{RX}} N_{\mathrm{TX}}} \sum_{c=1}^{C} \sum_{r_c=1}^{R_c} \bar{\alpha}_{r_c,k} \mathbf{a}_{\mathrm{RX}}(\theta_c + \vartheta_{r_c}) \mathbf{a}_{\mathrm{TX}}^{*}(\phi_c + \varphi_{r_c}). \tag{3.6}$$

Finally, we define $\bar{\boldsymbol{\alpha}}_k = [\bar{\alpha}_{1_1,k}, \cdots, \bar{\alpha}_{R_1,k}, \cdots, \bar{\alpha}_{1_C,k}, \cdots, \bar{\alpha}_{R_C,k}]^{\mathsf{T}}$, $\mathbf{A}_{\mathrm{RX}} = [\mathbf{a}_{\mathrm{RX}}(\theta_1 + \vartheta_{1_1}), \cdots, \mathbf{a}_{\mathrm{RX}}(\theta_C + \vartheta_{R_C})]$, and $\mathbf{A}_{\mathrm{TX}} = [\mathbf{a}_{\mathrm{TX}}(\phi_1 + \varphi_{1_1}), \cdots, \mathbf{a}_{\mathrm{TX}}(\phi_C + \varphi_{R_C})]$, to compactly write (3.6) as

$$\mathbf{H}[k] = \sqrt{N_{\mathrm{RX}} N_{\mathrm{TX}}} \mathbf{A}_{\mathrm{RX}} \mathrm{diag}(\bar{\boldsymbol{\alpha}}_k) \mathbf{A}_{\mathrm{TX}}^{*}. \tag{3.7}$$

The transmit covariance of the channel on sub-carrier k is defined as $\mathbf{R}_{\mathrm{TX}}[k] = \frac{1}{N_{\mathrm{RX}}}\mathbb{E}[\mathbf{H}^*[k]\mathbf{H}[k]]$ while the receive covariance is $\mathbf{R}_{\mathrm{RX}}[k] = \frac{1}{N_{\mathrm{TX}}}\mathbb{E}[\mathbf{H}[k]\mathbf{H}^*[k]]$. For the development of the proposed strategies, we make the typical assumption that the channel taps are uncorrelated. With this assumption, the covariances across all sub-carriers are identical [112]. In practice, the channel delay-taps have some correlation and the covariances on all sub-carriers, though similar, are not identical. In Section 3.7, we will test the robustness of the proposed strategies to the practical correlated delay-taps case. The uncorrelated taps assumption implies that (for a given k), the coefficients $\bar{\alpha}_{r_c,k}$ are uncorrelated i.e., $\mathbb{E}[\bar{\alpha}_{i,k}\bar{\alpha}^*_{j,k}] = 0,\ \forall i \neq j$. Let us denote the variance of coefficient $\bar{\alpha}_{r_c,k}$ as $\sigma^2_{\bar{\alpha}_{r_c}}$. Then, under the uncorrelated gains simplification, the transmit covariance for fixed AoDs can be written as $\mathbf{R}_{\mathrm{TX}}[k] = N_{\mathrm{TX}}\mathbf{A}_{\mathrm{TX}}\mathbf{R}_{\bar{\boldsymbol{\alpha}}}\mathbf{A}^*_{\mathrm{TX}}$, and similarly $\mathbf{R}_{\mathrm{RX}}[k] = N_{\mathrm{RX}}\mathbf{A}_{\mathrm{RX}}\mathbf{R}_{\bar{\boldsymbol{\alpha}}}\mathbf{A}^*_{\mathrm{RX}}$, where $\mathbf{R}_{\bar{\boldsymbol{\alpha}}} = \mathbb{E}[\bar{\boldsymbol{\alpha}}_k\bar{\boldsymbol{\alpha}}^*_k] = \mathrm{diag}([\sigma^2_{\bar{\alpha}_{1_1}}, \cdots, \sigma^2_{\bar{\alpha}_{R_C}}])$. We denote the transmit covariance averaged across the sub-carriers simply as $\mathbf{R}_{\mathrm{TX}} = \frac{1}{K}\sum_{k=1}^{K}\mathbf{R}_{\mathrm{TX}}[k]$, and the averaged receive covariance as $\mathbf{R}_{\mathrm{RX}} = \frac{1}{K}\sum_{k=1}^{K}\mathbf{R}_{\mathrm{RX}}[k]$.

3.4 Out-of-band covariance translation

In this section, we address the problem of obtaining an estimate of the mmWave covariance directly from the sub-6 GHz covariance with no in-band training. We continue the exposition assuming the receive covariance is translated (the transmit covariance is translated using the same procedure). To simplify notation, we remove the subscript RX from the receive covariance

in subsequent exposition. Hence, we seek to estimate $\mathbf{R} \in \mathbb{C}^{N_{\mathrm{RX}} \times N_{\mathrm{RX}}}$ from $\underline{\mathbf{R}} \in \mathbb{C}^{\underline{N}_{\mathrm{RX}} \times \underline{N}_{\mathrm{RX}}}$. We assume that the estimate of the sub-6 GHz covariance $\hat{\underline{\mathbf{R}}}$ is available. With no hardware constraints at sub-6 GHz and a small number of antennas, empirical estimation of $\hat{\underline{\mathbf{R}}}$ is easy [113]. Further, the CSI at sub-6 GHz is required for the operation of the sub-6 GHz system itself. Therefore, obtaining the out-of-band information (i.e., the sub-6 GHz covariance) for mmWave covariance estimation does not incur any additional training overhead.

In the parametric covariance translation proposed in this work, the parameters of the covariance matrix are estimated at sub-6 GHz. Subsequently, these parameters are used in the theoretical expressions of covariance matrices to generate mmWave covariance. To give a concrete example, consider a single-cluster channel. Assume a mean AoA θ, AS σ_ϑ, and a azimuth power spectrum (APS) with characteristic function $\Phi(x)$ corresponding to $\sigma_\vartheta = 1$. Then, under the small AS assumption, the channel covariance can be written as [73]

$$[\mathbf{R}]_{i,j} = e^{\mathrm{j}(i-j)2\pi\Delta\sin(\theta)}\Phi\big((i-j)2\pi\Delta\cos(\theta)\sigma_\vartheta\big). \tag{3.8}$$

To get a closed form expression for the covariance, (3.8) is evaluated for a specific APS. The resulting expressions for Truncated Laplacian, Truncated Gaussian, and Uniform distribution are summarized in Table 3.1. For a single-cluster channel, the mean AoA and AS of the cluster (i.e., only two parameters) are estimated at sub-6 GHz and subsequently used in one of the expressions (in

Table 3.1) to obtain the mmWave covariance [45]. This is possible, as under the assumption of the same mean AoA and AS at sub-6 GHz and mmWave, the theoretical expressions for sub-6 GHz covariance and mmWave covariance are parameterized by the same parameters and differ only in the size. For channels with multiple-clusters, the parametric covariance translation is complicated as the number of unknown parameters is typically higher. As an example, for only a two-cluster channel, 6 parameters need to be estimated. The 6 parameters are the AoA and AS of both clusters (i.e., 4 parameters), and the power contribution of each cluster in the covariance (i.e., 2 additional parameters). The estimation procedure is further complicated by the fact that the number of clusters is unknown, and needs to be estimated. In the following, we outline a parametric covariance translation procedure for multi-cluster channels.

Table 3.1: Theoretical expressions for covariance $[\mathbf{R}]_{i,j}$

APS	**Expression**
Truncated Laplacian [114]	$\frac{\beta e^{\mathrm{j}2\pi\Delta(i-j)\sin(\theta)}}{1+\frac{\sigma_\vartheta^2}{2}[2\pi\Delta(i-j)\cos(\theta)]^2},\ \beta=\frac{1}{1-e^{-\sqrt{2}\pi/\sigma_\vartheta}}$
Truncated Gaussian [73]	$e^{-((i-j)2\pi\Delta\cos(\theta)\sigma_\vartheta)^2}e^{\mathrm{j}2\pi\Delta(i-j)\sin(\theta)}$
Uniform [73]	$\frac{\sin((i-j)\varrho_\vartheta)}{((i-j)\varrho_\vartheta)}e^{\mathrm{j}2\pi\Delta(i-j)\sin(\theta)},$ $\varrho_\vartheta=\sqrt{3}\times 2\pi\Delta\sigma_\vartheta\cos(\theta)$

For clarity in exposition, we consider the covariance translation to be a four-step procedure and explain each step separately. In the first three steps, the parameters are estimated from sub-6 GHz covariance. These parameters are: (i) the number of clusters, (ii) the AoA and AS of each cluster, and (iii)

the power contribution of each cluster in the covariance. In the fourth step, the estimated parameters are used in covariance expressions - given in Table 3.1 and evaluated for the number of antennas in the mmWave system - to complete the translation.

3.4.0.1 Estimating the number of clusters

The first step in the parametric translation is to estimate the number of clusters in the channel. Enumerating the number of signals impinging on an array is a fundamental problem known as model order selection. The most common solution is to use information theoretic criteria e.g., minimum description length (MDL) [115] or Akaike information criterion (AIC) [116]. The model order selection algorithms estimate the number of point-sources and do not directly give the number of clusters (i.e., distributed/scattered sources). To obtain the number of clusters, we make the following observation. The dimension of the channel subspace of a two point-source channel is 2. In addition, it was shown in [73] that, the dimension of the channel subspace of a channel with a single-cluster and small AS is also 2. With this observation, the model order selection algorithms can be used for estimating the number of clusters. Specifically, if the number of point-sources estimated by a model order selection algorithm is $\underline{\hat{\mathrm{PS}}}$, we consider the channel to have $\underline{\hat{C}} = \max\{\lfloor \frac{\underline{\hat{\mathrm{PS}}}}{2} \rfloor, 1\}$ clusters. The term $\lfloor \frac{\underline{\hat{\mathrm{PS}}}}{2} \rfloor$ equates the number of clusters to half the point-sources (exactly for even number of point-sources, and approximately for odd). To deal with the case of a single source with very small AS, we set the minimum

number of clusters to 1.

3.4.0.2 Estimating angle-of-arrival and angle spread

AoA estimation is a well studied problem and several AoA estimation strategies exist [117, 118, 119, 120, 121]. Prior work has also considered the specific problem of estimating both the AoA and the AS jointly from an empirically estimated spatial covariance matrix. In this work, we use spread root-MUSIC algorithm [73], due to its low computational complexity and straightforward extension for multiple-clusters. We refer the interested reader to [73] for the details of the spread root-MUSIC algorithm. Here, we focus instead on a robustification necessary for the success of the proposed strategy.

If the channel has a single-cluster and the AS is very small, the spread root-MUSIC algorithm can fail [73]. In this case, the algorithm returns an arbitrary AoA and an unusually large AS. This failure can be detected by setting a threshold on AS. Specifically, if the estimated AS is larger than the threshold value, AoA only estimation (e.g., using root-MUSIC [122]) is performed and the AS is set to zero. In addition, the AoA only estimation should also be performed when only a single point-source is detected while estimating the number of clusters.

3.4.0.3 Estimating the power contribution of each cluster

We denote the covariance due to the $\underline{c}$th cluster as $\underline{\mathbf{R}}(\underline{\theta}_{\underline{c}}, \underline{\sigma}_{\underline{\vartheta},\underline{c}})$. This covariance is calculated using the expressions in Table 3.1. Specifically, the

AoA and AS estimated from the second step are used, and the covariance expressions are evaluated for the number of antennas in the sub-6 GHz system. Further, we denote the power contribution of the $\underline{c}$th cluster as $\underline{\epsilon}_{\underline{c}}$. Now, under the assumption of uncorrelated clusters, the total covariance can be written as

$$\underline{\mathbf{R}} = \sum_{\underline{c}=1}^{\underline{C}} \underline{\epsilon}_{\underline{c}} \underline{\mathbf{R}}(\underline{\theta}_{\underline{c}}, \underline{\sigma}_{\underline{\vartheta},\underline{c}}) + \underline{\sigma}^2_{\underline{\mathbf{n}}} \mathbf{I}. \tag{3.9}$$

Introducing the vectorized notation $\underline{\mathbf{r}} = \text{vec}(\underline{\mathbf{R}})$ for the covariance matrix, we re-write (3.9) as

$$\underline{\mathbf{r}} = \left[\underline{\mathbf{r}}(\underline{\theta}_1, \underline{\sigma}_{\underline{\vartheta},1}), \cdots, \underline{\mathbf{r}}(\underline{\theta}_{\underline{C}}, \underline{\sigma}_{\underline{\vartheta},\underline{C}}), \text{vec}(\mathbf{I})\right] \left[\underline{\epsilon}_1, \cdots, \underline{\epsilon}_{\underline{C}}, \underline{\sigma}^2_{\underline{\mathbf{n}}}\right]^{\mathsf{T}}. \tag{3.10}$$

The system of equations (3.10) can be solved (e.g., using non-negative least-squares) to obtain the power contributions of the clusters.

3.4.0.4 Obtaining the mmWave covariance

The mmWave covariance corresponding to the $\underline{c}$th cluster is denoted as $\mathbf{R}(\underline{\theta}_{\underline{c}}, \underline{\sigma}_{\underline{\vartheta},\underline{c}})$. Similar to sub-6 GHz covariance $\underline{\mathbf{R}}(\underline{\theta}_{\underline{c}}, \underline{\sigma}_{\underline{\vartheta},\underline{c}})$, the mmWave covariance $\mathbf{R}(\underline{\theta}_{\underline{c}}, \underline{\sigma}_{\underline{\vartheta},\underline{c}})$ is also calculated using the expressions in Table 3.1. The covariance expressions, however, are now evaluated for the number of antennas in the mmWave system. With this, we have the mmWave covariances corresponding to all $\underline{C}$ clusters. Further, we have estimates of the cluster power contributions $\underline{\epsilon}_{\underline{c}}$ from step three. We now use the mmWave analog of (3.9) to obtain the mmWave covariance, i.e.,

$$\mathbf{R} = \sum_{\underline{c}=1}^{\underline{C}} \underline{\epsilon}_{\underline{c}} \mathbf{R}(\underline{\theta}_{\underline{c}}, \underline{\sigma}_{\underline{\vartheta},\underline{c}}). \tag{3.11}$$

We have purposely ignored the contribution of white noise in (3.11). Though it is possible to estimate the noise variance at mmWave, it is not necessary for our application. This is because the hybrid precoders/combiners are designed to approximate the dominant singular vectors of the channel covariance matrix [19]. As the singular vectors of a covariance matrix do not change with the addition of a scaled identity matrix, the addition is inconsequential.

3.5 Out-of-band aided compressed covariance estimation

Compressed covariance estimation is a process of recovering the covariance information of a signal from its low-dimensional projections [123]. This problem has been studied for different covariance matrix structures e.g., Toeplitz, sparse and low-rank [123, 124]. There is some prior work on covariance estimation in hybrid mmWave systems, see e.g., [109, 110]. In [110], the Hermitian symmetry of the covariance matrix and the limited scattering of the mmWave channel are exploited. By exploiting Hermitian symmetry, [110] outperforms the methods that only use sparsity e.g., [109]. We closely follow the framework of [110] for compressed covariance estimation. As only SIMO systems were considered in [110], we extend [110] to MIMO systems. Subsequently, we use the concept of weighted sparse signal recovery to aid the in-band compressed covariance estimation with out-of-band information.

3.5.1 Problem formulation

We start with an implicit understanding that the formulation is per sub-carrier, but do not explicitly mention k in the equations to reduce the notation overhead. We assume a single stream transmission in the training phase without loss of generality. With $N_{\mathrm{s}} = 1$, the post RF-combining received signal can be written as

$$\mathbf{y}_t = \mathbf{W}^*_{\mathrm{RF},t}\mathbf{H}_t\mathbf{f} + \mathbf{W}^*_{\mathrm{RF},t}\mathbf{n}_t, \tag{3.12}$$

where we have introduced a discrete time index t. The time index t denotes a snapshot. We assume that the channel remains fixed inside a snapshot. Further, we have used vector notation for the precoder to highlight the single stream case and have made a simplistic choice $\mathsf{s}_t = 1$ for ease of exposition.

First, we outline a strategy to synthesize an omni-directional precoder. Note that, a single active antenna based omni-directional precoding is not feasible in large antenna systems due to per-antenna power constraint [125]. In this work, we utilize two successive transmissions to synthesize an omni-directional precoder. Thus, a single snapshot consists of two consecutive OFDM training frames. An example is that in the first training frame, we use $\mathbf{f}_1 = \frac{1}{\sqrt{N_{\mathrm{TX}}}}[1, \cdots, 1]^{\mathsf{T}}$, and in the second we use $\mathbf{f}_2 = \frac{1}{\sqrt{N_{\mathrm{TX}}}}[1, -1, \cdots, -1]^{\mathsf{T}}$. To see how these precoders can give omni-directional transmission, we write the received signal in the first transmission of the tth snapshot as

$$\mathbf{y}_{t,1} = \mathbf{W}^*_{\mathrm{RF},t}\mathbf{H}_t\mathbf{f}_1 + \mathbf{W}^*_{\mathrm{RF},t}\mathbf{n}_{t,1}, \tag{3.13}$$

where $\mathbf{n}_{t,1} \sim \mathcal{CN}(\mathbf{0}, \sigma_{\mathbf{n}}^2\mathbf{I})$, and the received signal in the second transmission of the tth snapshot as

$$\mathbf{y}_{t,2} = \mathbf{W}_{\mathrm{RF},t}^{*}\mathbf{H}_t\mathbf{f}_2 + \mathbf{W}_{\mathrm{RF},t}^{*}\mathbf{n}_{t,2}. \tag{3.14}$$

Now we consider the received signal (3.12) in the tth snapshot, as the sum of the two individual transmissions, i.e.,

$$\begin{aligned}\mathbf{y}_t = \mathbf{y}_{t,1} + \mathbf{y}_{t,2} &= \mathbf{W}_{\mathrm{RF},t}^{*}\mathbf{H}_t(\mathbf{f}_1 + \mathbf{f}_2) + \mathbf{W}_{\mathrm{RF},t}^{*}(\mathbf{n}_{t,1} + \mathbf{n}_{t,2}), \\ &= \frac{2}{\sqrt{N_{\mathrm{TX}}}}\mathbf{W}_{\mathrm{RF},t}^{*}\mathbf{H}_t[1, 0, \cdots, 0]^{\mathsf{T}} + \mathbf{W}_{\mathrm{RF},t}^{*}(\mathbf{n}_{t,1} + \mathbf{n}_{t,2}).\end{aligned} \tag{3.15}$$

Thus effectively, combined over two transmissions, the precoder behaves as an omni-directional precoder, and effectively reduces a MIMO system to a SIMO system. The factor $\frac{2}{\sqrt{N_{\mathrm{TX}}}}$ in (3.15) denotes the power lost in trying to achieve omni-directional transmission. Similarly, as two independent transmissions are summed up, we have $\mathbf{n}_t \sim \mathcal{CN}(\mathbf{0}, 2\sigma_{\mathbf{n}}^2\mathbf{I})$. Depending on the scenario, this SNR loss (due to low received power and increased noise variance) may be tolerated or compensated by repeated transmission. Assuming that the path angles do not change during the T snapshots, the MIMO channel (3.7) can be written as

$$\mathbf{H}_t = \sqrt{N_{\mathrm{RX}}N_{\mathrm{TX}}}\mathbf{A}_{\mathrm{RX}}\mathrm{diag}(\bar{\boldsymbol{\alpha}}_t)\mathbf{A}_{\mathrm{TX}}^{*},\ t = 1, 2, \cdots, T, \tag{3.16}$$

where the vector $\bar{\boldsymbol{\alpha}}_t$ represents the complex coefficients in the tth snapshot. Further, note that

$$\mathbf{H}_t[1, 0, \cdots, 0]^{\mathsf{T}} = \sqrt{N_{\mathrm{RX}}}\mathbf{A}_{\mathrm{RX}}\bar{\boldsymbol{\alpha}}_t. \tag{3.17}$$

Now, the received signal (3.12) can be re-written as

$$\mathbf{y}_t = \mathbf{W}^*_{\mathrm{RF},t}\mathbf{A}_{\mathrm{RX}}\mathbf{g}_t + \mathbf{W}^*_{\mathrm{RF},t}\mathbf{n}_t, \tag{3.18}$$

where we have introduced $\mathbf{g}_t = 2\sqrt{\frac{N_{\mathrm{RX}}}{N_{\mathrm{TX}}}}\bar{\boldsymbol{\alpha}}_t$. After which, the covariance of the received signal $\mathbf{y}_t$ is

$$\mathbf{R}_{\mathbf{y}} = \mathbb{E}[\mathbf{y}\mathbf{y}^*] = \mathbf{W}^*_{\mathrm{RF}}\mathbf{A}_{\mathrm{RX}}\mathbf{R}_{\mathbf{g}}\mathbf{A}^*_{\mathrm{RX}}\mathbf{W}_{\mathrm{RF}} + 2\sigma^2_{\mathbf{n}}\mathbf{W}^*_{\mathrm{RF}}\mathbf{W}_{\mathrm{RF}}, \tag{3.19}$$

where the expectation is over snapshots and $\mathbf{R}_{\mathbf{g}} = \mathbb{E}[\mathbf{g}\mathbf{g}^*]$. By the definition of $\mathbf{g}_t$, we have

$$\mathbf{R}_{\mathbf{g}} = 4\frac{N_{\mathrm{RX}}}{N_{\mathrm{TX}}}\mathbb{E}[\bar{\boldsymbol{\alpha}}\bar{\boldsymbol{\alpha}}^*] = 4\frac{N_{\mathrm{RX}}}{N_{\mathrm{TX}}}\mathbf{R}_{\bar{\boldsymbol{\alpha}}}. \tag{3.20}$$

As the RX covariance can be written as $\mathbf{R}_{\mathrm{RX}} = N_{\mathrm{RX}}\mathbf{A}_{\mathrm{RX}}\mathbf{R}_{\bar{\boldsymbol{\alpha}}}\mathbf{A}^*_{\mathrm{RX}}$, once $\mathbf{R}_{\mathbf{g}}$ and the AoAs are estimated, the receive covariance can be obtained. Hence, the main problem is to recover $\mathbf{R}_{\mathbf{g}}$ and the AoAs from $\mathbf{R}_{\mathbf{y}}$. We re-write (3.18) as

$$\mathbf{y}_t \approx \mathbf{W}^*_{\mathrm{RF},t}\bar{\mathbf{A}}_{\mathrm{RX}}\bar{\mathbf{g}}_t + \mathbf{W}^*_{\mathrm{RF},t}\mathbf{n}_t, \tag{3.21}$$

where $\bar{\mathbf{A}}_{\mathrm{RX}}$ is an $N_{\mathrm{RX}} \times B_{\mathrm{RX}}$ dictionary matrix whose columns are composed of the array response vector evaluated at a predefined set of AoAs, and $\bar{\mathbf{g}}_t$ is a $B_{\mathrm{RX}} \times 1$ vector. The received signal (3.18) can only be approximated as (3.21) because the true AoAs in the channel are not confined to the predefined set. Further, though there are several paths in the channel, the AoAs are spaced closely due to clustered behavior. Therefore, the number of coefficients with significant magnitude in $\bar{\mathbf{g}}_t$ is $L \ll B_{\mathrm{RX}}$.

Due to limited scattering of the channel, the matrix, $\bar{\mathbf{g}}_t\bar{\mathbf{g}}_t^*$, has a Hermitian sparse structure. This structure can be exploited in the estimation of $\hat{\mathbf{R}}_{\bar{\mathbf{g}}}$ via the algorithm called covariance OMP (COMP) [110]. The performance of the COMP algorithm, however, is limited by the number of RF-chains used in the systems. This limitation can be somewhat circumvented by using time-varying RF-combiners $\mathbf{W}_{\mathrm{RF},t}$ [20, 110]. Specifically, we use a distinct RF-combiner in each snapshot. The modification of COMP that uses time-varying RF-combiners is called dynamic covariance OMP (DCOMP) [110].

Remark: Our extension of [110] (from SIMO to MIMO systems) is based on omnidirectional precoding to reduce the MIMO system to a SIMO system. Another possible extension of [110] to MIMO systems was outlined in [50]. Specifically, the full MIMO covariance $\mathbf{R}_{\text{full}} = \mathbb{E}[\text{vec}(\mathbf{H})\text{vec}(\mathbf{H})^*]$ was estimated in [50], though with high computational complexity. To understand this, consider $N_{\mathrm{TX}} = N_{\mathrm{RX}} = 64$ antennas and 4x oversampled dictionaries i.e., $B_{\mathrm{RX}} = B_{\mathrm{TX}} = 256$. These are modest system parameters for mmWave communication and were used in [50]. With these parameters, the full covariance estimation requires support search over a $B_{\mathrm{RX}}B_{\mathrm{TX}} \times B_{\mathrm{RX}}B_{\mathrm{TX}} = 65536 \times 65536$ dimensional Hermitian-sparse unknown. In comparison, our approach requires the recovery of a $B_{\mathrm{RX}} \times B_{\mathrm{RX}}$ unknown and a $B_{\mathrm{TX}} \times B_{\mathrm{TX}}$ unknown, i.e., two 256×256 dimensional Hermitian-sparse unknowns. Furthermore, in mmWave systems, the precoders and combiners are designed based on transmit and receive covariances separately. Therefore, we believe our approach is more reasonable than [50].

3.5.2 Weighted compressed covariance estimation

The compressed covariance estimation algorithm divides the AoA range into B_{RX} intervals using the dictionary $\bar{\mathbf{A}}_{\mathrm{RX}}$ and assumes that the prior probability of the support is uniform, i.e., the active path angles on the grid have the same probability p throughout the AoA range. This is a reasonable assumption under no prior information about the AoAs. If some prior information about the non-uniformity in the support is available, the compressed covariance estimation algorithms can be modified to incorporate this prior information. Note that the DCOMP algorithm is an extension of the OMP algorithm to the covariance estimation problem. In [38] a modified OMP algorithm called logit weighted - OMP (LW-OMP) was proposed for non-uniform prior probabilities. Here we use logit weighting in compressed covariance estimation via DCOMP algorithm. Assume that $\boldsymbol{\rho} \in \mathbb{R}^{B_{\mathrm{RX}} \times 1}$ is the vector of prior probabilities $0 \leq [\boldsymbol{\rho}]_i \leq 1$. Then we introduce an additive weighting function $w([\boldsymbol{\rho}]_i)$ to weight the DCOMP algorithm according to prior probabilities. The authors refer the interested reader to [38] for the details of logit weighting and the selection of $w([\boldsymbol{\rho}]_i)$. The general form of $w([\boldsymbol{\rho}]_i)$, however, can be given as $w([\boldsymbol{\rho}]_i) = J_{\mathrm{w}} \log \dfrac{[\boldsymbol{\rho}]_i}{1 - [\boldsymbol{\rho}]_i}$, where J_{w} is a constant that depends on the number of active coefficients in $\hat{\mathbf{R}}_{\bar{\mathbf{g}}}$, the amplitude of the unknown coefficients, and the noise level [38]. We present the logit weighted - DCOMP (LW-DCOMP) in Algorithm 3. In the absence of prior information, LW-DCOMP can be used with uniform probability $\boldsymbol{\rho} = \varepsilon \mathbf{1}$, where $0 < \varepsilon <= 1$, which is equivalent to DCOMP.

Algorithm 3 Logit weighted - Dynamic Covariance OMP (LW-DCOMP)

Input: $\mathbf{W}_{\mathrm{RF},t}\forall T, \mathbf{y}_t\forall T, \bar{\mathbf{A}}_{\mathrm{RX}}, \sigma^2_{\mathbf{n}}, \mathbf{p}$
Initialization: $\mathbf{V}_t = \mathbf{y}_t\mathbf{y}_t^*\forall t, \mathcal{S} = \emptyset, i = 0$
while $(\sum_t \|\mathbf{V}_t\|_{\mathrm{F}} > 2\sigma^2_{\mathbf{n}} \sum_t \|\mathbf{W}^*_{\mathrm{RF},t}\mathbf{W}_{\mathrm{RF},t}\|_{\mathrm{F}}$ and $i < M_{\mathrm{RX}})$ **do**
  $j = \arg\max_i \sum_{t=1}^{T} |[\mathbf{W}_{\mathrm{RF},t}\bar{\mathbf{A}}_{\mathrm{RX}}]^*_{:,i}\mathbf{V}_t[\mathbf{W}_{\mathrm{RF},t}\bar{\mathbf{A}}_{\mathrm{RX}}]_{:,i}| + w([\boldsymbol{\rho}]_i)$
  $\mathcal{S} = \mathcal{S} \cup \{j\}$
  $\hat{\mathbf{R}}_{\bar{\mathbf{g}},t} = [\mathbf{W}_{\mathrm{RF},t}\bar{\mathbf{A}}_{\mathrm{RX}}]^{\dagger}_{:,\mathcal{S}}(\mathbf{y}_t\mathbf{y}_t^*)\big([\mathbf{W}_{\mathrm{RF},t}\bar{\mathbf{A}}_{\mathrm{RX}}]^{\dagger}_{:,\mathcal{S}}\big)^*,\ \forall t$
  $\mathbf{V}_t = \hat{\mathbf{R}}_{\mathbf{y},t} - [\mathbf{W}_{\mathrm{RF},t}\bar{\mathbf{A}}_{\mathrm{RX}}]_{:,\mathcal{S}}\hat{\mathbf{R}}_{\bar{\mathbf{g}},t}[\mathbf{W}_{\mathrm{RF},t}\bar{\mathbf{A}}_{\mathrm{RX}}]^*_{:,\mathcal{S}}, \forall t$
  $i = i + 1$
end while
Output: $\mathcal{S}$, $\hat{\mathbf{R}}_{\bar{\mathbf{g}}} = \frac{1}{T}\sum_{t=1}^{T}\hat{\mathbf{R}}_{\bar{\mathbf{g}},t}$.

The spatial information from sub-6 GHz can be used to obtain a proxy for $\boldsymbol{\rho}$. Specifically, let us define an $\underline{N}_{\mathrm{RX}} \times B_{\mathrm{RX}}$ dictionary matrix $\underline{\bar{\mathbf{A}}}_{\mathrm{RX}}$, which is obtained by evaluating the sub-6 GHz array response vector at the same B_{RX} angles that were used to obtain the mmWave dictionary matrix $\bar{\mathbf{A}}_{\mathrm{RX}}$. Then, a simple proxy of the probability vector based on the sub-6 GHz covariance is

$$\boldsymbol{\rho} = J_{\rho}\frac{|\frac{1}{B_{\mathrm{RX}}}\sum_{b=1}^{B_{\mathrm{RX}}}[\underline{\bar{\mathbf{A}}}^*_{\mathrm{RX}}\,\underline{\mathbf{R}}\,\underline{\bar{\mathbf{A}}}_{\mathrm{RX}}]_{:,b}|}{\max|\frac{1}{B_{\mathrm{RX}}}\sum_{b=1}^{B_{\mathrm{RX}}}[\underline{\bar{\mathbf{A}}}^*_{\mathrm{RX}}\,\underline{\mathbf{R}}\,\underline{\bar{\mathbf{A}}}_{\mathrm{RX}}]_{:,b}|}, \tag{3.22}$$

where the matrix $\underline{\bar{\mathbf{A}}}^*_{\mathrm{RX}}\,\underline{\mathbf{R}}\,\underline{\bar{\mathbf{A}}}_{\mathrm{RX}}$ is the extended virtual channel covariance [126]. We average across the columns of the extended virtual channel covariance matrix to obtain a vector, and normalize by the largest entry in this vector to ensure that $0 \leq [\boldsymbol{\rho}]_i \leq 1$. Finally, we scale by an appropriately chosen constant J_{ρ} that captures the reliability of the out-of-band information. The reliability is a function of the sub-6 GHz and mmWave spatial congruence, and operating SNR. A higher value for J_{ρ} should be used for highly reliable information. For the results in Section 3.7, we optimized for J_{ρ} by testing a

few values and choosing the one that gave the best performance.

3.6 SNR degradation due to covariance mismatch

We start by providing the preliminaries required for analyzing the loss in received post-processing SNR due to imperfections in channel covariance estimates. We perform the analysis for a single path channel and as such single stream transmission suffices. This can be considered an extreme case where the AS is zero, and as such the only AoA is the mean AoA θ. For the channel model presented in Section 3.3, this implies that the receive covariance can be written as $\mathbf{R}_{\mathrm{RX}} = N_{\mathrm{RX}}\sigma_\alpha^2 \mathbf{a}_{\mathrm{RX}}(\theta)\mathbf{a}_{\mathrm{RX}}^*(\theta)$. Similarly, the transmit covariance can be written as $\mathbf{R}_{\mathrm{TX}} = N_{\mathrm{TX}}\sigma_\alpha^2 \mathbf{a}_{\mathrm{TX}}(\phi)\mathbf{a}_{\mathrm{TX}}^*(\phi)$. The subspace decomposition of the receive covariance matrix is

$$\mathbf{R}_{\mathrm{RX}} = \mathbf{U}_{\mathrm{RX}}\mathbf{\Sigma}\mathbf{U}_{\mathrm{RX}}^* = \mathbf{U}_{\mathrm{RX,s}}\mathbf{\Sigma}_{\mathrm{s}}\mathbf{U}_{\mathrm{RX,s}}^* + \mathbf{U}_{\mathrm{RX,n}}\mathbf{\Sigma}_{\mathrm{n}}\mathbf{U}_{\mathrm{RX,n}}^*, \tag{3.23}$$

where the columns of $\mathbf{U}_{\mathrm{RX}}$ are the singular vectors and the diagonal entries of $\mathbf{\Sigma}$ are the singular values. The vector $\mathbf{U}_{\mathrm{RX,s}}$ spans the channel subspace, and the columns of $\mathbf{U}_{\mathrm{RX,n}}$ span the noise subspace. The transmit covariance $\mathbf{R}_{\mathrm{TX}}$ has a similar subspace decomposition. The statistical digital precoding/combining is based on the channel subspace. For a single path channel, the array response vector evaluated at AoA θ spans the channel subspace. As such, the received signal with digital precoding/combing based on channel

subspace can be written as

$$\begin{aligned}
\mathsf{y} &= \mathbf{U}_{\mathrm{RX,s}}^{*}\mathbf{H}\mathbf{U}_{\mathrm{TX,s}}\mathsf{s} + \mathbf{U}_{\mathrm{RX,s}}^{*}\mathbf{n}, \\
&= \sqrt{N_{\mathrm{RX}}N_{\mathrm{TX}}}\alpha\mathbf{a}_{\mathrm{RX}}^{*}(\theta)\mathbf{a}_{\mathrm{RX}}(\theta)\mathbf{a}_{\mathrm{TX}}^{*}(\phi)\mathbf{a}_{\mathrm{TX}}(\phi)\mathsf{s} + \mathbf{a}_{\mathrm{RX}}^{*}(\theta)\mathbf{n}, \\
&= \sqrt{N_{\mathrm{RX}}N_{\mathrm{TX}}}\alpha\mathsf{s} + \mathbf{a}_{\mathrm{RX}}^{*}(\theta)\mathbf{n}. \qquad (3.24)
\end{aligned}$$

From (3.24), the average received SNR with perfect covariance knowledge is

$$\mathrm{SNR}_{\mathbf{R}} = \frac{\mathrm{N_{RX}N_{TX}}\mathbb{E}[|\alpha|^2]\mathbb{E}[|\mathsf{s}|^2]}{\mathbb{E}[\|\mathbf{a}_{\mathrm{RX}}^{*}(\theta)\mathbf{n}\|_{\mathrm{F}}^2]}. \qquad (3.25)$$

Recall from Section 3.3 that the variance of channel paths is $\mathbb{E}[|\alpha|^2] = \sigma_\alpha^2$, and the transmit symbol power is $\mathbb{E}[|\mathsf{s}|^2] = \frac{P}{K}$. Further, with noise $\mathbf{n} \sim \mathcal{CN}(\mathbf{0}, \sigma_{\mathbf{n}}^2\mathbf{I})$, we have $\mathbb{E}[\|\mathbf{a}_{\mathrm{RX}}^{*}(\theta)\mathbf{n}\|_{\mathrm{F}}^2] = \sigma_{\mathbf{n}}^2$. Therefore, we re-write (3.25) as

$$\mathrm{SNR}_{\mathbf{R}} = \frac{\mathrm{N_{RX}N_{TX}P}\sigma_\alpha^2}{\mathrm{K}\sigma_{\mathbf{n}}^2}. \qquad (3.26)$$

We model the error in the estimated covariance as additive, i.e., the true covariance matrix and the estimated covariance matrix differ by a perturbation $\Delta\mathbf{R}$ such that $\hat{\mathbf{R}}_{\mathrm{RX}} = \mathbf{R}_{\mathrm{RX}} + \Delta\mathbf{R}_{\mathrm{RX}}$ and $\hat{\mathbf{R}}_{\mathrm{TX}} = \mathbf{R}_{\mathrm{TX}} + \Delta\mathbf{R}_{\mathrm{TX}}$. For out-of-band covariance translation presented in Section 3.4, the perturbation embodies the error in sub-6 GHz parameter estimation and subsequent translation to mmWave. For out-of-band aided compressed covariance estimation presented in Section 3.5, the perturbation embodies the errors in sparse support recovery and subsequent estimation of the coefficients on the recovered

support set. Now, a decomposition of the estimated covariance matrix $\hat{\mathbf{R}}_{\mathrm{RX}}$ (similar to (3.23)) is

$$\hat{\mathbf{R}}_{\mathrm{RX}} = \hat{\mathbf{U}}_{\mathrm{RX}}\hat{\mathbf{\Sigma}}\hat{\mathbf{U}}_{\mathrm{RX}}^{*} = \hat{\mathbf{U}}_{\mathrm{RX,s}}\hat{\mathbf{\Sigma}}_{\mathrm{s}}\hat{\mathbf{U}}_{\mathrm{RX,s}}^{*} + \hat{\mathbf{U}}_{\mathrm{RX,n}}\hat{\mathbf{\Sigma}}_{\mathrm{n}}\hat{\mathbf{U}}_{\mathrm{RX,n}}^{*}. \tag{3.27}$$

The vector $\hat{\mathbf{U}}_{\mathrm{RX,s}}$ can be written as a sum of two vectors $\mathbf{U}_{\mathrm{RX,s}}$ and $\Delta\mathbf{U}_{\mathrm{RX,s}}$. Hence, the vector $\hat{\mathbf{U}}_{\mathrm{RX,s}}$ will typically not meet the normalization $\|\hat{\mathbf{U}}_{\mathrm{RX,s}}\|^2 = 1$ assumed in the system model. We ensure that the power constraint on the precoders/combiners is met by using a normalized version. Hence, the received signal with digital precoding/combining based on the imperfect covariance is

$$\mathsf{y} = \frac{\hat{\mathbf{U}}_{\mathrm{RX,s}}^{*}}{\|\hat{\mathbf{U}}_{\mathrm{RX,s}}\|}\mathsf{H}\frac{\hat{\mathbf{U}}_{\mathrm{TX,s}}}{\|\hat{\mathbf{U}}_{\mathrm{TX,s}}\|}\mathsf{s} + \frac{\hat{\mathbf{U}}_{\mathrm{RX,s}}^{*}}{\|\hat{\mathbf{U}}_{\mathrm{RX,s}}\|}\mathbf{n}. \tag{3.28}$$

Now we quantify the averaged receive SNR with imperfect covariance in the following theorem.

Theorem 3.6.1. *For the received signal* y *in* (3.28)*, the precoder that follows the model* $\hat{\mathbf{U}}_{\mathrm{TX,s}} = \hat{\mathbf{U}}_{\mathrm{TX,s}} + \Delta\mathbf{U}_{\mathrm{TX,s}}$*, and the combiner that follows the model* $\hat{\mathbf{U}}_{\mathrm{RX,s}} = \hat{\mathbf{U}}_{\mathrm{RX,s}} + \Delta\mathbf{U}_{\mathrm{RX,s}}$*, the averaged received SNR is*

$$\mathrm{SNR}_{\hat{\mathbf{R}}} = \frac{\mathrm{N_{RX}N_{TX}P}\sigma_{\alpha}^{2}}{\mathrm{K}\sigma_{\mathbf{n}}^{2}\|\hat{\mathbf{U}}_{\mathrm{RX,s}}\|^{2}\|\hat{\mathbf{U}}_{\mathrm{TX,s}}\|^{2}}. \tag{3.29}$$

Proof. See Appendix. □

Now given the SNR with perfect covariance (3.26) and the SNR with imperfect covariance (3.29), the loss in the SNR, γ is

$$\gamma = \frac{\mathrm{SNR}_{\mathbf{R}}}{\mathrm{SNR}_{\hat{\mathbf{R}}}} = \|\hat{\mathbf{U}}_{\mathrm{RX,s}}\|^{2}\|\hat{\mathbf{U}}_{\mathrm{TX,s}}\|^{2}. \tag{3.30}$$

The SNR loss (3.30) is given in terms of the vectors that span the estimated channel subspace. In the following theorem, we give the loss explicitly in terms of the perturbations $\Delta\mathbf{R}_{\mathrm{RX}}$ and $\Delta\mathbf{R}_{\mathrm{TX}}$.

Theorem 3.6.2. *The loss in the SNR γ can be written approximately as*

$$\gamma \approx \left(1 + \frac{\|\Delta\mathbf{R}_{\mathrm{RX}}\mathbf{U}_{\mathrm{RX,s}}\|^2}{N_{\mathrm{RX}}^2\sigma_\alpha^4}\right)\left(1 + \frac{\|\Delta\mathbf{R}_{\mathrm{TX}}\mathbf{U}_{\mathrm{TX,s}}\|^2}{N_{\mathrm{TX}}^2\sigma_\alpha^4}\right), \tag{3.31}$$

and can be bounded as

$$\gamma \lesssim \left(1 + \frac{\sigma_{\max}^2(\Delta\mathbf{R}_{\mathrm{RX}})}{N_{\mathrm{RX}}^2\sigma_\alpha^4}\right)\left(1 + \frac{\sigma_{\max}^2(\Delta\mathbf{R}_{\mathrm{TX}})}{N_{\mathrm{TX}}^2\sigma_\alpha^4}\right), \tag{3.32}$$

and

$$\gamma \gtrsim \left(1 + \frac{\sigma_{\min}^2(\Delta\mathbf{R}_{\mathrm{RX}})}{N_{\mathrm{RX}}^2\sigma_\alpha^4}\right)\left(1 + \frac{\sigma_{\min}^2(\Delta\mathbf{R}_{\mathrm{TX}})}{N_{\mathrm{TX}}^2\sigma_\alpha^4}\right), \tag{3.33}$$

where $\sigma_{\max}(\cdot)$ and $\sigma_{\min}(\cdot)$ represent the largest and smallest singular value of the argument.

Proof. See Appendix. □

The SNR loss expression (3.31) admits a simple explanation. The loss is proportional to the alignment of the true channel subspace to the column space of the perturbation matrix. If the true channel subspace is orthogonal to the column space of the perturbation matrix i.e., $\mathbf{U}_{\mathrm{RX,s}}$ lies in the null space of $\Delta\mathbf{R}_{\mathrm{RX}}$, then there is no loss in the SNR due to the perturbation, which makes intuitive sense. Further, the results (3.32) and (3.33) give the bounds on SNR loss explicitly in the form of the singular values of the perturbation matrices $\Delta\mathbf{R}_{\mathrm{RX}}$ and $\Delta\mathbf{R}_{\mathrm{TX}}$.

3.7 Simulation results

In this section, we present simulation results to test the effectiveness of the proposed covariance estimation strategies and validate the SNR loss analysis. First, we test the performance of the proposed covariance estimation strategies in simpler channels, assuming that the parameters governing the sub-6 GHz and mmWave channels are consistent. This is to say that the cluster in the sub-6 GHz and mmWave channel has the same AoA, AoD, arrival AS, and departure AS. Subsequently, we study the performance of the proposed covariance estimation strategies in realistic channels when the parameters of the sub-6 GHz and mmWave channels do not match. Finally, we validate the SNR loss analysis. To show the benefit of the out-of-band information in comparison with in-band only training, we compare the proposed strategies with the DCOMP algorithm [110]. For covariance estimation, the DCOMP algorithm was shown to perform better than several well known sparse recovery algorithms [110].

We test the performance of the proposed covariance estimation strategies using two metrics. The first metric is the efficiency metric η [49] that captures the similarity in the channel subspace of the true covariance and the estimated covariance. This metric is relevant in the current setup as the precoders/combiners are designed using the singular vectors that span the channel subspace. The efficiency metric is given as [49]

$$\eta(\mathbf{R}, \hat{\mathbf{R}}) = \frac{\mathrm{tr}(\mathbf{U}_{N_\mathrm{s}}^* \hat{\mathbf{R}} \mathbf{U}_{N_\mathrm{s}})}{\mathrm{tr}(\hat{\mathbf{U}}_{N_\mathrm{s}}^* \mathbf{R} \hat{\mathbf{U}}_{N_\mathrm{s}})}, \tag{3.34}$$

where $\mathbf{U}_{N_\mathrm{s}}$ ($\hat{\mathbf{U}}_{N_\mathrm{s}}$) are the N_s singular vectors of the matrix $\mathbf{R}$ ($\hat{\mathbf{R}}$) corresponding to the largest N_s singular values. Note that $0 \leq \eta \leq 1$ and it is desirable to make η as close to 1 as possible.

The second metric is the achievable rate using the hybrid precoders/combiners designed from the covariance information. We assume that the channel covariance is constant over T_stat OFDM blocks. Here, the subscript stat signifies that the interval T_stat is the time for which the statistics remain unchanged, and not the coherence time of the channel. In fact, the statistics vary slowly and typically T_stat is much larger than the channel coherence time. If T_train out of the T_stat blocks are used in covariance estimation, $(1 - \frac{T_\mathrm{train}}{T_\mathrm{stat}})$ is the fraction of blocks left for data transmission. With this, the effective achievable rate is estimated as [18, 65]

$$R = \max\big(0, 1 - \frac{T_\mathrm{train}}{T_\mathrm{stat}}\big)\frac{1}{K}\sum_{k=1}^{K}\log_2\Big|\mathbf{I}_{N_\mathrm{s}} + \frac{P}{KN_\mathrm{s}}\mathbf{R_n}[k]^{-1}\mathbf{W}^*_{\mathrm{BB}}[k]\mathbf{W}^*_{\mathrm{RF}}\mathbf{H}[k]\mathbf{F}_{\mathrm{RF}}\mathbf{F}_{\mathrm{BB}}[k]\times \mathbf{F}^*_{\mathrm{BB}}[k]\mathbf{F}^*_{\mathrm{RF}}\mathbf{H}^*[k]\mathbf{W}_{\mathrm{RF}}\mathbf{W}_{\mathrm{BB}}[k]\Big|, \tag{3.35}$$

where $\mathbf{R_n}[k] = \sigma^2_{\mathbf{n}}\mathbf{W}_{\mathrm{BB}}[k]^*\mathbf{W}^*_{\mathrm{RF}}\mathbf{W}_{\mathrm{RF}}\mathbf{W}_{\mathrm{BB}}[k]$ is the noise covariance matrix after combining.

The main simulation parameters are summarized in Table 3.2. The path-loss coefficient at sub-6 GHz and mmWave is 3 and the complex path coefficients of the channels are IID complex Normal. The CP length is one less than the number of delay-taps. A raised cosine filter with a roll-off factor

Table 3.2: Simulation Parameters

Parameter	**Sub-6 GHz**	**MmWave**
Operating frequency	3.5GHz	28GHz
Bandwidth	150MHz	850MHz
Transmit antennas and RF-chains	$\underline{N}_{\mathrm{TX}} = \underline{M}_{\mathrm{TX}} = 4$	$N_{\mathrm{TX}} = 32,\ M_{\mathrm{TX}} = 8$
Receive antennas and RF-chains	$\underline{N}_{\mathrm{RX}} = \underline{M}_{\mathrm{RX}} = 8$	$N_{\mathrm{RX}} = 64,\ M_{\mathrm{RX}} = 16$
Inter-element spacing in wavelength	$\underline{\Delta} = 1/2$	$\Delta = 1/2$
Transmission power	$\underline{P} = 30$ dBm per 25 MHz [101]	$P = 43$ dBm [102]
Sub-carriers	$\underline{K} = 32$	$K = 128$
Delay-taps	$\underline{D} = 9$	$D = 33$

of 1 is used for pulse shaping. The number of streams is $N_{\mathrm{s}} = 4$. The MDL algorithm [115] is used to estimate the number of clusters for covariance translation. A 2x over-complete DFT basis. i.e., $B_{\mathrm{RX}} = 2N_{\mathrm{RX}}$ and $B_{\mathrm{TX}} = 2N_{\mathrm{TX}}$ is used for compressed covariance estimation. Two-bit phase-shifters based analog precoders/combiners are used. All results are obtained by ensemble averaging over 1000 independent trials.

We start by considering a simple two-cluster channel, where each cluster contributes 100 rays. We assume that all the rays within a cluster arrive at the same time. We use Gaussian APS with 3° AS. To calculate the efficiency metric (3.34), we use the theoretical expressions of the covariance matrix with Gaussian APS (see Table 3.1) in (3.11) as the true covariance. The TX-RX distance is 90 m and the number of snapshots for sub-6 GHz covariance estimation is 30.

We present the results of covariance translation as a function of the separation between the mean AoA of the clusters. Specifically, the mean AoA of one cluster is fixed at 5° and the mean AoA of the second cluster is varied from 5°-20°. The difference between the mean AoAs of the clusters is the separation in degrees. We assume that the power contribution of the clusters is the same i.e., $\epsilon_1 = \epsilon_2 = 0.5$. The time of arrival of the cluster at 5° is fixed at 0. For the other cluster, the time of arrival is chosen uniformly at random between 0 to 10 ns. We plot the number of clusters estimated in the proposed translation strategy versus mean AoA separation in Fig. 3.4. Note that due to the robustification discussed earlier, it is possible that the final number of estimated clusters be different than the estimate provided by MDL. We are plotting the final number of estimated clusters. For small separations, effectively the channel has a single-cluster, and hence a single-cluster is estimated. As the separation increased, the algorithm can detect one or two clusters. With large enough separation, the algorithm successfully determines two clusters. Fig. 3.5 shows the efficiency metric of the proposed strategy versus separation. When separation is below 8°, and two clusters are detected, their AoA and AS estimation is erroneous due to small separation and the efficiency is low. As the separation increases, the AoA and AS estimation improves and with it the efficiency of the covariance translation approach.

We test the performance of the proposed LW-DCOMP algorithm as a function of TX-RX distance. The number of snapshots is 30. We fix the clusters at 5° and 45°, and the cluster powers at $\epsilon_1 = \epsilon_2 = 0.5$. The time of

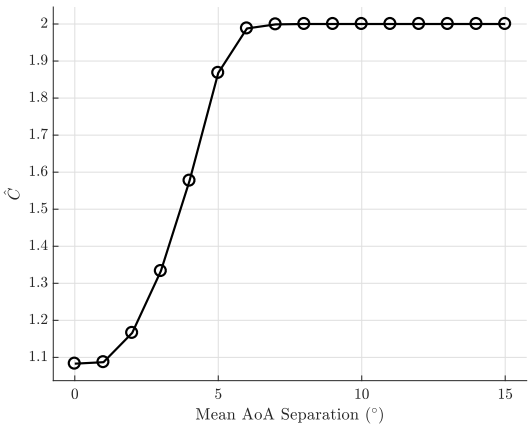

Figure 3.4: The estimated number of clusters $\hat{C}$ (in a two-cluster channel) versus the mean AoA separation (°) of the proposed covariance translation strategy. The mean AoA of the first cluster is 5° and the mean AoA of the second cluster is varied from 5° to 20°. The TX-RX distance is 90 m. The algorithm successfully estimates 2 clusters when the mean AoA separation is greater than 7°.

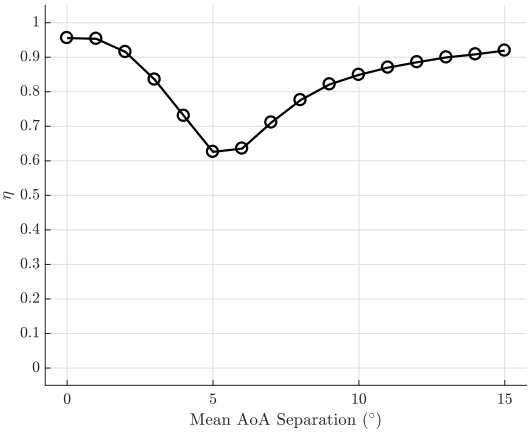

Figure 3.5: The efficiency metric η (in a two-cluster channel) versus the mean AoA separation (°) of the proposed covariance translation strategy. The mean AoA of the first cluster is 5° and the mean AoA of the second cluster is varied from 5° to 20°. The TX-RX distance is 90 m. The efficiency is high when the algorithm at low (high) mean AoA separations as the algorithm successfully estimates 1 (2) clusters.

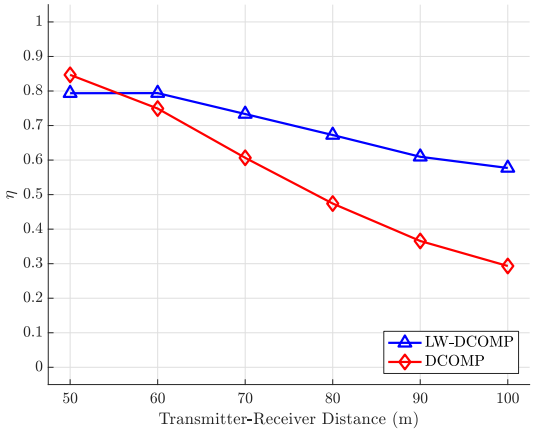

Figure 3.6: The efficiency metric η (in a two-cluster channel) of the the proposed LW-DCOMP algorithm versus the TX-RX distance (m). First cluster has mean AoA 5° and the second cluster has a mean AoA 45°. The number of snapshots T is 30. The out-of-band aided LW-DCOMP approach performs better at large TX-RX distances.

arrival of the cluster at 5° is fixed at 0, and the time of arrival of the cluster at 45° is chosen uniformly at random between 0 to 10 ns. The results of this experiment are shown in Fig. 3.6. We see that as the TX-RX separation increases - and the SNR decreases - the benefit of using out-of-band information in compressed covariance estimation becomes clear.

So far we did not consider the spatial discrepancy in the sub-6 GHz and mmWave channels. We now test the performance of the proposed strategies in more realistic channels, i.e., where sub-6 GHz and mmWave systems have a mismatch. Specifically, we generate the channels according to the methodology proposed in [41]. We refer the interested reader to [41] for the details of the method to generate sub-6 GHz and mmWave channels. Here, we only give the channel parameters. The sub-6 GHz and mmWave channels have

$\underline{C} = 10$ and $C = 5$ clusters respectively, each contributing $\underline{R}_{\mathrm{c}} = R_{\mathrm{c}} = 20$ rays. The mean angles of the clusters are limited to $[-\frac{\pi}{3}, \frac{\pi}{3})$. The relative angle shifts come from a wrapped Gaussian distribution with with AS $\{\underline{\sigma}_{\vartheta_c}, \underline{\sigma}_{\varphi_c}\} = 4^\circ$ and $\{\sigma_{\vartheta_c}, \sigma_{\varphi_c}\} = 2^\circ$ As the delay spread of sub-6 GHz channel is expected to be larger than the delay spread of mmWave [86, 87, 88, 89], we choose $\underline{\tau}_{\mathrm{RMS}} \approx 3.8$ ns and $\tau_{\mathrm{RMS}} \approx 2.7$ ns. The relative time delays of the paths within the clusters are drawn from zero mean Normal distributions with RMS AS $\underline{\sigma}_{\underline{\tau}_{r_{\underline{c}}}} = \frac{\underline{\tau}_{\mathrm{RMS}}}{10}$ and $\sigma_{\tau_{r_c}} = \frac{\tau_{\mathrm{RMS}}}{10}$. The powers of the clusters are drawn from exponential distributions. Specifically, the exponential distribution with parameter μ is defined as $f(x|\mu) = \frac{1}{\mu} e^{-\frac{x}{\mu}}$. The parameter for sub-6 GHz was chosen as $\underline{\mu} = 0.2$ and for mmWave $\mu = 0.1$. This implies that the power in late arriving multi-paths for mmWave will decline more rapidly than sub-6 GHz. The system parameters are identical to the previously explained setup. The hybrid precoders/combiners are designed using the greedy algorithm given in [19]. The effective achievable rate results are shown in Fig. 3.7. For compressed covariance estimation and weighted compressed covariance estimation, we assume that $T_{\mathrm{stat}} = 2048$. The number of training OFDM blocks is $T_{\mathrm{train}} = 2 \times 2 \times T$. Here, T is the number of snapshots. A factor of 2 appears as we use 2 OFDM blocks to create omnidirectional transmission, i.e., one snapshot. Another factor of 2 appears as the training is performed for the transmit and the receive covariance estimation. The ideal case - i.e., sample covariance based on perfect channel knowledge - is also plotted. The rate for the ideal case is calculated assuming no overhead. The

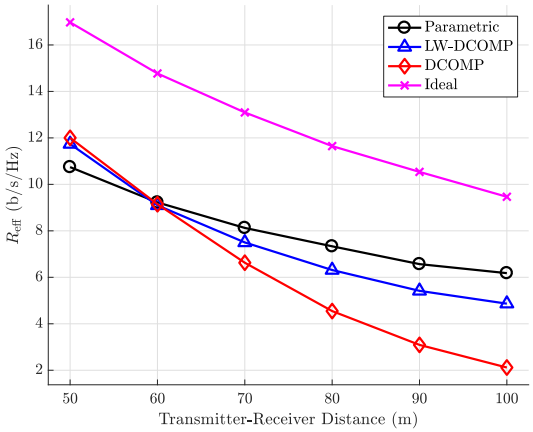

Figure 3.7: The effective achievable rate of the proposed covariance estimation strategies versus the TX-RX distance. The rate calculations are based on $T_{\text{stat}} = 2048$ blocks and $T_{\text{train}} = 120$ blocks. The benefit of out-of-band information becomes more pronounced at high TX-RX distances.

observations about the benefit of using out-of-band information in mmWave covariance estimation also hold in this experiment. Note that, the achievable rate drops with increasing TX-RX distance due to decreasing SNR. Further, this experiment validates the robustness of the designed covariance estimation strategies to the correlated channel taps case.

We now compare the overhead of the proposed LW-DCOMP approach to the DCOMP approach. We use $T_{\text{train}} = 2 \times 2 \times T$ for rate calculations. In Fig. 3.8, we plot the effective achievable rate versus the number of snapshots T for three different values of T_{stat}. For dynamic channels, i.e., with $T_{\text{stat}} = 1024$ or $T_{\text{stat}} = 2048$, the effective rate of both LW-DCOMP and DCOMP increases with snapshots, but as we keep on increasing T, the rate starts to decrease. This is because, though the channel estimation quality increases, a significant

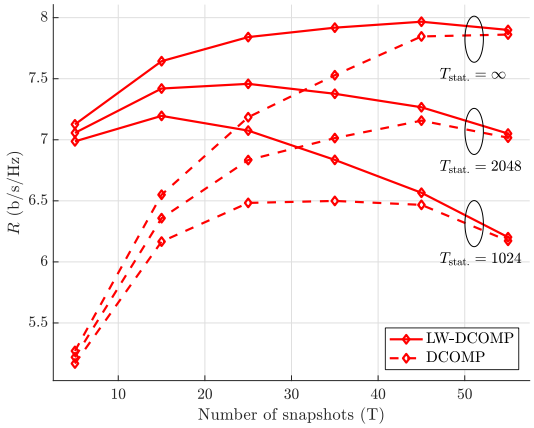

Figure 3.8: The effective achievable rate of LW-DCOMP and DCOMP versus the number of snapshots T (at the transmitter and the receiver). The effective rate is plotted for three values of T_{stat}. The TX-RX distance is fixed at 70 m. The LW-DCOMP reduces the training overhead of DCOMP by over 3x.

fraction of the T_{stat} is spent training and the thus there is less time to use the channel for data transmission. Taking $T_{\text{stat}} = 2048$ as an example, the highest rate of DCOMP algorithm is 7.16 b/s/Hz and is achieved with 45 snapshots. In comparison, the optimal rate of the LW-DCOMP algorithm is 7.46 b/s/Hz and is achieved with only 25 snapshots. The LW-DCOMP achieves a rate better than the highest rate of DCOMP algorithm (7.16 b/s/Hz) with less than 15 snapshots. Thus, the LW-DCOMP can reduce the training overhead of DCOMP by over 3x.

Note that, so far we have used the greedy algorithm given in [19] to design the hybrid precoders/combiners. The greedy algorithm designs the RF as well as baseband precoders/combiners based on the spatial covariance information. It is, however, possible to design the RF precoder/combiner based on

the channel covariance and the baseband precoder based on the instantaneous channel information. There are two reasons to follow such a strategy over [19]. One, note that the RF precoders/combiners are implemented in time-domain. As such the RF precoder/combiner is the same across all sub-carriers. The baseband precoder/combiners, however, can be designed per sub-carrier. This freedom is not exploited by [19]. This is because there is a common covariance across sub-carriers and any strategy based solely on covariance will be limited to the same RF and baseband precoder/combiner across all sub-carriers. Two, note that the instantaneous channel captures the variations of gains across the sub-carriers. Therefore, separate baseband precoders/combiners based on the instantaneous channel per sub-carrier may give better performance. We now compare the following strategies for designing the precoders/combiners.

1. Full instantaneous CSI and fully digital precoding/combining: The instantaneous MIMO channel is available, and the precoders/combiners on all sub-carriers are designed based on the singular vector decomposition of the channel.

2. Full statistical CSI and partial instantaneous CSI: The RF precoders/combiners are designed based on covariance information using [19]. The effective instantaneous channel (after applying the RF precoders/combiners) on each sub-carriers is then used to design the baseband precoders/combiners using the singular vector decomposition of the effective channel.

3. Statistical CSI only: The RF as well as baseband precoders/combiners are based on covariance information and are designed using [19].

We test the performance of the three strategies as a function of the number of paths in the channel and present the results in Fig. 3.9. Note that for this experiment, we consider a simple channel model. We consider that there are C clusters each contributing $R_{\mathrm{c}} = 1$ paths. The AoA and AoD are $\mathcal{U}[-\frac{\pi}{3}, \frac{\pi}{3}]$, and the power contribution of each cluster is $1/C$. The results in Fig. 3.9 show that with a few paths (1-2), all the strategies have similar performance. As the number of paths increase (3-4), the full instantaneous CSI performs a bit better than the other two strategies based on covariance information. That said when the number of paths is greater than the number of RF-chains (i.e., 4 at the TX), the performance gap increases. The full instantaneous CSI performs much better than two strategies based on covariance information. Furthermore, the full statistical CSI and partial instantaneous CSI based strategy performs better than the statistical CSI only based strategy. This is because partial instantaneous CSI allows the freedom to design the baseband precoder per-subcarriers, unlike statistical CSI only case. These observations are in-line with [127] where optimality of frequency flat precoding was established for limited scattering channels.

Now we verify the SNR loss analysis outlined in Section 3.6. For this purpose, we consider two mmWave systems with $N_{\mathrm{TX}} = N_{\mathrm{RX}} = 64$ and $N_{\mathrm{TX}} = N_{\mathrm{RX}} = 16$ antennas. The number of RF-chains in both cases

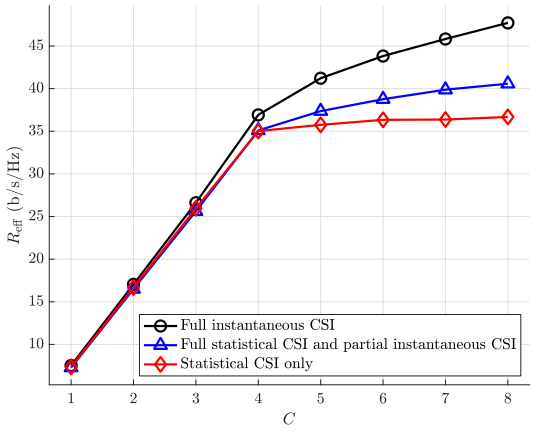

Figure 3.9: The comparative rate of (i) Full instantaneous CSI, (ii) Full statistical CSI and partial instantaneous CSI, and (iii) Statistical CSI only. The number of RF-chains is $M_{\text{RX}} = 8$ and $M_{\text{TX}} = 4$ and the number of streams is $N_{\text{s}} = 4$. The number of sub-carriers is $K = 16$, and the TX-RX distance is fixed at 70 m.

is $M_{\text{TX}} = M_{\text{RX}} = \sqrt{N_{\text{TX}}} = \sqrt{N_{\text{RX}}}$. We plot the loss in SNR γ as a function of the SNR per-subcarrier i.e., $\text{SNR}_{\text{k}} = \frac{\text{P}}{\sigma_{\text{n}}^2 \text{K}}$. We assume that $[\Delta \mathbf{R}_{\text{RX}}]_{i,j} = [\Delta \mathbf{R}_{\text{TX}}]_{i,j} \sim \mathcal{CN}(0, \frac{1}{\text{SNR}_{\text{k}}})$. The smallest singular value of the Gaussian matrices vanishes as the dimensions increase [128], and the analytical lower bound (3.33) becomes trivial. As such, we only show the analytical upper bound (3.32) in Fig. 3.10. We compare the upper bound on SNR loss (3.32) and the empirical difference in the average SNR of the mmWave systems based on true covariance and the perturbed covariance. The empirical difference is plotted for the case when the singular vectors are used as precoder/combiner (i.e., assuming fully digital precoding/combining) and also for the case when hybrid precoders/combiners are used. From the results, we can see that the upper bound is valid for both systems with 16 and 64 antennas respectively.

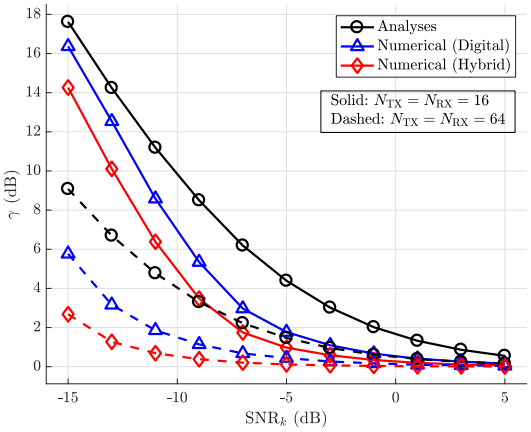

Figure 3.10: The upper bound on the SNR loss γ with complex Normal perturbation. The number of RF-chains is $M_{\mathrm{TX}} = M_{\mathrm{RX}} = \sqrt{N_{\mathrm{TX}}} = \sqrt{N_{\mathrm{RX}}}$ and $\mathrm{SNR_k} = \frac{\mathrm{P}}{\sigma_{\mathbf{n}}^2 \mathrm{K}}$. The upper-bound derived in the analysis holds for both the tested scenarios.

An interesting observation is that when the hybrid precoders/combiners are used in the mmWave system, the loss due to the mismatch in the estimated and true covariance is less than the case when fully digital precoding and combining is used.

3.8 Comparison of proposed covariance estimation strategies

We now compare some characteristics of the proposed covariance estimation strategies.

3.8.1 Computational complexity

The out-of-band covariance translation has four steps. The computational complexity of the first two steps at the receiver is dictated by the

eigenvalue decomposition of the covariance matrix, i.e., $O(\underline{N}_{\mathrm{RX}}^3)$. The computational complexity of finding the cluster powers using least-squares (i.e., the third step) is $O(\hat{C}^2\underline{N}_{\mathrm{RX}}^2)$. Finally, the computational complexity of fourth step, i.e., constructing the mmWave covariance, is $O(\hat{C}N_{\mathrm{RX}}^2)$. For the out-of-band aided compressed covariance estimation strategy, the online computational complexity of the LW-DCOMP algorithm is $O(TB_{\mathrm{RX}}M_{\mathrm{RX}}^2L)$.

3.8.2 Overhead

The out-of-band covariance translation completely eliminates the in-band training. As the sub-6 GHz channel information is required for the operation of sub-6 GHz system, the out-of-band covariance translation does not have a training overhead. The out-of-band aided compressed covariance estimation strategy uses in-band training in conjunction with out-of-band information. The in-band training overhead, however, is very small. As shown in Fig. 3.8, the proposed out-of-band aided compressed covariance estimation has an achievable rate of more than 7 (b/s/Hz) with only 5 snapshots.

3.8.3 Robustness to erroneous information

The out-of-band covariance translation relies completely on sub-6 GHz information. As such, the out-of-band covariance translation may perform poorly if the mmWave and sub-6 GHz channels are spatially incongruent. The out-of-band aided compressed covariance estimation relies on in-band as well as out-of-band information. The reliance on in-band information makes it

more robust to spatial incongruence between sub-6 GHz and mmWave channels.

3.8.4 Inherent limitations

The out-of-band covariance translation is based on parametric estimation. The number of point sources that can be estimated at the receiver are $\underline{N}_{\mathrm{RX}} - 1$. This translates to $\hat{C} = \max\{\lfloor \frac{\underline{N}_{\mathrm{RX}}-1}{2} \rfloor, 1\}$ estimated clusters. As such, the translated mmWave covariance is also limited to $\hat{C}$ clusters. The out-of-band aided compressed covariance strategy assumes limited scattering of the mmWave channel. Further, the covariance recovery is limited by the number of RF-chains in the mmWave system. Specifically, it is required that the number of coefficients with significant magnitude be $L \leq M_{\mathrm{RX}}$.

3.8.5 Favorable operating conditions

If the TX-RX separation is small, i.e., the SNR is high, the out-of-band aided compressed covariance estimation performs better than out-of-band covariance translation (see Fig. 3.8). As the TX-RX distance increases, however, the out-of-band covariance translation starts to perform better. This result informs that depending on the TX-RX separation (or the SNR), the out-of-band aided compressed covariance estimation or the out-of-band covariance translation may be preferred.

3.9 Conclusion

In this chapter, we used the sub-6 GHz covariance to predict the mmWave covariance. We presented a parametric approach that relies on the estimates of mean angle and angle spread and their subsequent use in theoretical expressions of the covariance pertaining to a postulated power azimuth spectrum. To aid the in-band compressed covariance estimation with out-of-band information, we formulated the compressed covariance estimation problem as weighted compressed covariance estimation. For a single path channel, we bounded the loss in SNR caused by imperfect covariance estimation using singular-vector perturbation theory.

The out-of-band covariance translation and out-of-band aided compressed covariance estimation had better effective achievable rate than in-band only training, especially in low SNR scenarios. The out-of-band covariance translation eliminated the in-band training but performed poorly (in comparison with in-band training) when the SNR of the mmWave link was favorable. The out-of-band aided compressed covariance estimation reduced the training overhead of the in-band only covariance estimation by 3x.

Chapter 4

Millimeter Wave Link Configuration Using Radar Information

In this chapter, we propose to use a passive radar receiver at the road-side unit to reduce the training overhead of establishing a millimeter wave communication link. Specifically, the passive radar taps the transmissions from the automotive radars of the vehicles on road. The spatial covariance of the received radar signals is, in turn, used to establish the communication link. To this end, we propose a simplified radar receiver that does not require the transmitted waveform as a reference. We also propose a covariance correction strategy to improve the similarity of the radar data and communication channel. We present the simulation results based on ray-tracing data to demonstrate the benefit of proposed radar covariance correction strategy and to show the potential of using passive radar for establishing the communication links. The results show that (i) covariance correction improves the similarity of radar and communication APS, and (ii) the proposed radar-assisted strategy reduces the training overhead significantly and is particularly useful in non-line-of-sight scenarios. Part of this work was published in [51] (©IEEE) and a part is under preparation for submission.

4.1 Motivation and prior work

High data-rate communication is possible at millimeter waves (mmWaves) owing to the large bandwidth [1, 2, 53]. Low pre-beamforming signal-to-noise ratio (SNR), however, poses several challenges in establishing reliable mmWave links. Highly directional communication by deploying a large number of antennas can overcome the low SNR. Large antenna systems, however, will be inefficient (or even infeasible) from hardware cost and energy consumption point of view, if a dedicated high-resolution RF-chain is used for each antenna element. As such, either low-resolution RF-chains will be used with each antenna [105, 129], or a small number of high-resolution RF-chains will be used [18, 19, 130]. These architectures, though low cost and energy efficient, make the link configuration difficult. The primary reason is that the channel is not accessible at the baseband. In low-resolution architectures, the channel observed at the baseband is quantized. With limited RF-chains, the baseband observes a low-dimensional projection of the channel observed at the RF front-end. Therefore, link configuration in hardware limited architectures requires a large training overhead. This problem is further compounded in highly mobile scenarios, like vehicle-to-everything (V2X) communication, where channel changes frequently and rapid link re-configuration is necessary.

In this work, we propose to use a passive radar at the roadside unit (RSU) to configure the mmWave link. The passive radar receiver array at the RSU taps the signals transmitted by the automotive radars on the ego-vehicle. The mmWave communication channels and the radar received signals

stem from the same environment. Therefore, there is bound to be similarity in the spatial information embedded in the radar received signal and spatial characteristics of the communication channels. As such, we seek to use the spatial covariance of the radar received signals for mmWave link configuration.

Several sources of out-of-band information have been considered for mmWave communication systems. In [63, 31, 41, 46], spatial information extracted from sub-6 GHz channels was used for mmWave systems. For vehicular mmWave communications, the location of the vehicle has been used to reduce the beam-training overhead [32, 33]. Light Detection and Ranging (LIDAR) data has been used to detect the line-of-sight cases (LOS) between the RSU and the vehicles, and subsequently to reduce the beam-training overhead [131]. In [132], information from inertial sensors mounted on the antenna arrays has been used for beam-tracking in vehicle-to-vehicle (V2V) communication systems.

The prior work on using location [32, 33], LIDAR [131], and inertial sensors [132] is limited only to LOS links. The sub-6 GHz assisted strategies in [63, 31] are also limited to LOS.

There is also some prior work on using radar for mmWave communications. In [34], radar covariance was used to design the hybrid analog-digital precoders. In [133], the location of the vehicle was estimated using radar, and later this information was used to reduce the mmWave training overhead. In [134], a joint communication-radar system based on IEEE 802.11ad physical layer frames was used. Once the location of the vehicle was determined

through the radar operation, it was used to reduce the training overhead. In [36], radar-based vehicle tracking is used to avoid blockage by preemptively switching to a link that is predicted to be unblocked. For an indoor environment, the location of all targets is estimated using radar in [135]. This information is then used to predict the channel as the users move.

As with [32, 33], the radar-based location estimation [133, 134, 36] is limited only to LOS links. Similarly, in [135], it is not possible to recover the NLOS targets, and hence their contribution in the channel of a user. Radar covariance used in [34] provides more information than location. In this work, we also use radar covariance for mmWave links. As such, among the prior work, [34] can be considered closest to our current work. That said, the key difference between this work and [34] is that in this work we use a passive radar, whereas [34] used an active radar. This difference has two implications. First, putting an active radar on the RSU for mmWave links implies power cost. This power cost is remarkably reduced in passive radars as no signal is transmitted. Second, the active radar mounted on the RSU is also limited to the LOS as the NLOS ego-vehicle cannot be detected. In contrast, as we tap the signals transmitted by the ego-vehicle, our approach works even in NLOS scenarios. This claim is verified in the simulation section using ray-tracing data.

There are also several technical novelties unique to our work. These include a simplified radar receiver architecture for passive radar, correcting the angle estimation bias in FMCW radars, and a similarity metric to assess

the similarity of radar and communication APS.

4.2 Contributions

The main contributions of this chapter are as follows:

- We propose to use a passive radar at the RSU. The passive radar at the RSU will tap the radar signals transmitted by the automotive radars mounted on the ego-vehicle. The spatial covariance of the radar signals received at the RSU is in turn used to configure the mmWave link.

- We propose a simplified radar receiver architecture that does not require the transmitted waveform as a reference. We show that the spatial covariance of the signals in the simplified architecture is the same as the spatial covariance with perfect waveform knowledge. Due to the lack of waveform knowledge, however, the range and Doppler cannot be recovered using the proposed architecture.

- In [37], it was shown that the angle estimation in frequency modulated continuous wave (FMCW) radar is biased. We note that a similar bias appears in frequency division duplex (FDD) systems, where the uplink (UL) covariance is used to configure the downlink (DL). After establishing this connection, we use a strategy initially proposed for FDD covariance correction [47], to correct the bias in FMCW radars.

- In order to use the radar information for configuring the mmWave links,

it is necessary to understand the congruence (or similarity) of the spatial information provided by radar and the spatial characteristic of the mmWave channel. Intuitively, by congruence, we mean the similarity in the azimuth power spectrum (APS) of radar and communication. To quantify this similarity, we propose a similarity metric to compare two power spectra. We show that in certain cases the proposed similarity metric is identical to relative precoding efficiency (RPE), i.e., a commonly used metric to measure the accuracy of covariance estimation in literature [48, 49, 50]. Further, [48], the RPE was related to the rate. As such, establishing a connection between the proposed metric and RPE also implies a connection between the proposed similarity metric and rate.

The rest of this chapter is organized as follows: In Section 4.3, we discuss the general vehicle-to-infrastructure (V2I) communication setup. We discuss the communication system model in Section 4.4, and radar system model in Section 4.5. We outline the proposed simplified radar receiver in Section 4.5, the strategy to correct the bias in FMCW radar in Section 4.7, and the metric to compare the similarity of radar and communication in Section 4.8. Next, we provide the simulation results in Section 4.9, and finally conclude the chapter in Section 4.10.

4.3 V2I communication setup

We consider the vehicle-to-infrastructure (V2I) communication setup shown in Fig. 4.1. The RSU is equipped with a communication array and a passive radar array. The communication and radar arrays are collocated and horizontally aligned. The ego-vehicle on the road - as shown in Fig. 4.2 - is equipped with multiple communication arrays as proposed in 3GPP [136]. The vehicle is also equipped with multiple medium range radars (MRRs) (e.g., as used in Audi A8 [137]). Note that the radars and the communication arrays on the vehicle are not collocated. Our objective is to tap the radar transmissions at the RSU to obtain the radar spatial covariance. Subsequently, we seek to use this spatial covariance to configure the mmWave communication link. The developments in this work assume uniform linear arrays (ULAs) for communication between the RSU and the vehicle. The radars at the vehicle are single antenna, whereas the RSU has a passive ULA to tap the radar transmissions. With suitable modifications, however, the strategies proposed in this work can be extended to other array geometries.

4.4 Communication system model

The mmWave communication system is shown in Fig. 4.3. The RSU communication array has N_{RSU} antennas and $M_{\mathrm{RSU}} \leq N_{\mathrm{RSU}}$ RF-chains. The vehicle has A antenna arrays, each with N_{V} antenna elements and $M_{\mathrm{V}} \leq N_{\mathrm{V}}$ RF-chains. We assume that $N_{\mathrm{s}} \leq \min\{M_{\mathrm{RSU}}, M_{\mathrm{V}}\}$ data-streams are transmitted. For communication, we consider an OFDM system with K sub-

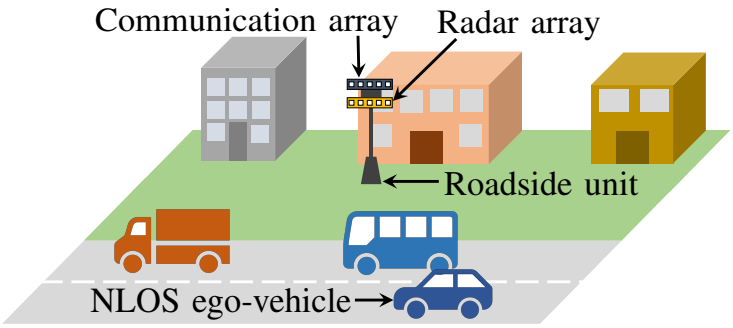

Figure 4.1: The V2I communication setup with the RSU equipped with a communication and a radar array.

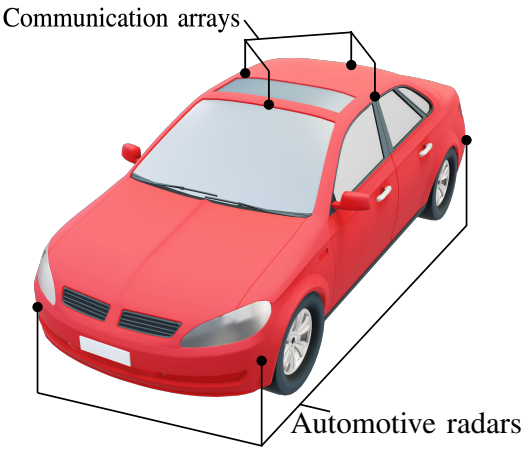

Figure 4.2: The ego-vehicle with multiple communication arrays and multiple radars.

carriers. The transmission symbols on sub-carrier k are $\mathbf{s}[k] \in \mathbb{C}^{N_\mathrm{s}\times 1}$ that follow $\mathbb{E}[\mathbf{s}[k]\mathbf{s}^*[k]] = \frac{P_\mathrm{c}}{KN_\mathrm{s}}\mathbf{I}_{N_\mathrm{s}}$, where P_c is the total average transmitted power. Let $\mathbf{F}_{\mathrm{BB}}[k] \in \mathbb{C}^{M_{\mathrm{RSU}}\times N_\mathrm{s}}$ be a baseband-precoder and $\mathbf{F}_{\mathrm{RF}} \in \mathbb{C}^{N_{\mathrm{RSU}}\times M_{\mathrm{RSU}}}$ be an RF-precoder, then we use $\mathbf{F}[k] = \mathbf{F}_{\mathrm{RF}}\mathbf{F}_{\mathrm{BB}}[k] \in \mathbb{C}^{N_{\mathrm{RSU}}\times N_\mathrm{s}}$ to denote the precoder on sub-carrier k. The RF-precoder is implemented in the time-domain

and is common to all sub-carriers. We assume that the RF-precoder is implemented using quantized phase-shifters with a finite set of possible values i.e., $[\mathbf{F}_{\mathrm{RF}}]_{i,j} = \frac{1}{\sqrt{N_{\mathrm{RSU}}}} e^{\mathrm{j}\zeta_{i,j}}$, where $\zeta_{i,j}$ is the quantized phase. The precoders satisfy the total power constraint $\sum_{k=1}^{K} \|\mathbf{F}[k]\|_{\mathrm{F}}^2 = KN_{\mathrm{s}}$.

We assume perfect time and frequency synchronization at the receiver. Further, let $\mathbf{W}_{\mathrm{BB}}^{(a)}[k] \in \mathbb{C}^{M_{\mathrm{V}} \times N_{\mathrm{s}}}$ be a baseband-combiner, and $\mathbf{W}_{\mathrm{RF}}^{(a)} \in \mathbb{C}^{N_{\mathrm{V}} \times M_{\mathrm{V}}}$ be an RF-combiner, then we use $\mathbf{W}^{(a)}[k] = \mathbf{W}_{\mathrm{RF}}^{(a)} \mathbf{W}_{\mathrm{BB}}^{(a)}[k] \in \mathbb{C}^{N_{\mathrm{V}} \times N_{\mathrm{s}}}$ to denote the combiner. For the ath array on the vehicle, if $\mathsf{H}^{(a)}[k]$ denotes the frequency-domain $N_{\mathrm{V}} \times N_{\mathrm{RSU}}$ mmWave MIMO channel on sub-carrier k, then the post-processing received signal on sub-carrier k is

$$\mathsf{y}^{(a)}[k] = \mathsf{W}^{(a)*}[k] \mathsf{H}^{(a)}[k] \mathsf{F}[k] \mathsf{s}[k] + \mathsf{W}^{(a)*}[k] \mathsf{n}^{(a)}[k], \tag{4.1}$$

where $\mathbf{n}^{(a)} \sim \mathcal{CN}(\mathbf{0}, \sigma_{\mathbf{n}}^2 \mathbf{I})$ is the additive white Gaussian noise.

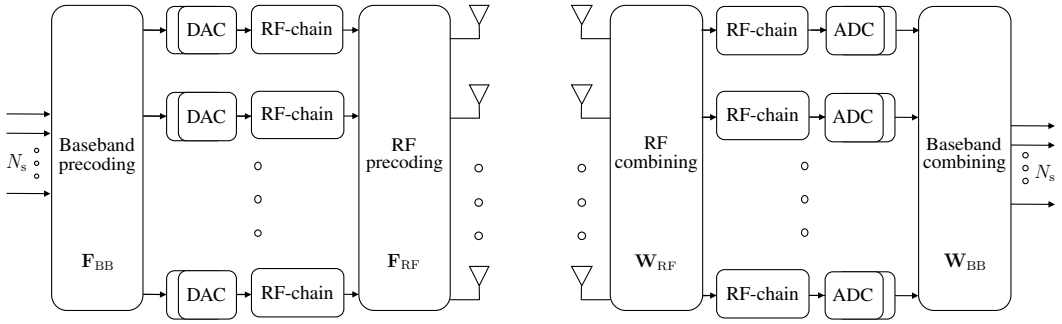

Figure 4.3: The mmWave communication system with hybrid analog-digital precoding and combining.

4.4.1 Channel model

We adopt a wideband geometric channel model with C clusters. Each cluster has a mean time-delay $\tau_c \in \mathbb{R}$, mean physical angle-of-departure (AoD) and angle-of-arrival (AoA) $\{\theta_c, \phi_c\} \in [0, 2\pi)$. Each cluster contributes R_c rays/paths between the RSU and the vehicle, where each ray $r_c \in [R_c]$ has a relative time-delay τ_{r_c}, relative angle shift $\{\vartheta_{r_c}, \varphi_{r_c}\}$, and a complex path gain α_{r_c}. W use $\mathbf{a}_{\mathrm{V}}(\theta)$ and $\mathbf{a}_{\mathrm{RSU}}(\phi)$ to denote the antenna array response vectors of the vehicle and the RSU, respectively. Let Δ be the inter-element spacing normalized by the wavelength, then the array response vector of the RSU is

$$\mathbf{a}_{\mathrm{RSU}}(\theta) = [1, e^{\mathrm{j}2\pi\Delta\sin(\theta)}, \cdots, e^{\mathrm{j}(N_{\mathrm{RSU}}-1)2\pi\Delta\sin(\theta)}]^{\mathsf{T}}, \tag{4.2}$$

The array response vector of the vehicle arrays is defined in a similar manner. Further, let $p(\tau)$ denote the combined effects of analog filtering and pulse shaping filter evaluated at point τ, and let T_{c} be the signaling interval. To write the channel model, we remove the superscript (a) from the channel $\mathbf{H}$ to lighten the notation with the understanding that the channels between the RSU and all vehicle arrays follow the same model. Now, the delay-d MIMO channel matrix $\mathbf{H}[d]$ is [65]

$$\mathbf{H}[d] = \sum_{c=1}^{C} \sum_{r_c=1}^{R_c} \alpha_{r_c} p(dT_{\mathrm{c}} - \tau_c - \tau_{r_c}) \mathbf{a}_{\mathrm{V}}(\phi_c + \varphi_{r_c}) \mathbf{a}^*_{\mathrm{RSU}}(\theta_c + \vartheta_{r_c}). \tag{4.3}$$

If there are D delay-taps in the channel, the channel at sub-carrier k, $\mathbf{H}[k]$ is [65]

$$\mathbf{H}[k] = \sum_{d=0}^{D-1} \mathbf{H}[d] e^{-\mathrm{j}\frac{2\pi k}{K} d}. \tag{4.4}$$

4.4.2 Covariance model

The RSU spatial covariance on sub-carrier k is defined as $\mathbf{R}_{\mathrm{RSU}}[k] = \frac{1}{N_{\mathrm{V}}}\mathbb{E}[\mathbf{H}^{*}[k]\mathbf{H}[k]]$. For the development of the proposed strategies, we make the typical assumption that covariances across all sub-carriers are identical [112]. With this assumption, we can base our designs on a covariance averaged across the sub-carriers and denoted simply as $\mathbf{R}_{\mathrm{RSU}} = \frac{1}{K}\sum_{k=1}^{K}\mathbf{R}_{\mathrm{RSU}}[k]$. Note that same covariance across sub-carriers implies that the time domain channel taps are uncorrelated. In practice, however, the channel delay-taps have some correlation and the spatial covariance matrices on all sub-carriers, though similar, are not identical. Thus designing the RF and baseband precoders/combiners for all sub-carriers using an averaged covariance will result in some performance loss. Note, however, that the analog combiner is designed commonly for all sub-carriers. As such, if the covariance is used only for analog precoder and combiner design, it is feasible to use averaged covariance. The baseband can then be configured independently for all sub-carriers.

4.5 Radar system model

The ego-vehicle shown in Fig. 4.2 is equipped with multiple radars. We start by developing the system model for a single radar and later incorporate transmissions from all radars. An FMCW radar system is shown in Fig. 4.4. For the development, we consider a fully digital receiver at the RSU. This assumption can be justified, as, for radar, a fully digital receiver can be emulated by a switching network and a few RF-chains. Specifically, measurements from

only a few antennas are collected at a given time. These measurements are then combined by correcting for the effects of sequential sampling to mimic a simultaneous measurement from all antennas. The INRAS Radarbook [138] is an example of a radar with this architecture. Specifically, two analog-to-digital converters (ADCs) are sequentially connected to four antennas. These four sequential measurements (from two antennas each) are then corrected and combined to obtain a received signal from all the eight receive antennas. Note also that we are only interested in retrieving angular information from the radar. As such, co-prime arrays can also be used. Using co-prime arrays the spatial correlation matrix can be recovered for a large array with a few antenna elements [139], each connected with a dedicated RF-chain.

The FMCW signals are transmitted in chirps. Let T_{p} be the chirp duration, and let B_{r} be the radar bandwidth, then $\beta = \frac{B_{\mathrm{r}}}{T_{\mathrm{p}}}$ is the chirp rate [140, 141]. If we let f_{r} denote the initial frequency of the radar, then the transmit waveform is [140, 141]

$$s_{\mathrm{r}}(t) = \exp(\mathrm{j}2\pi(f_{\mathrm{r}}t + \frac{\beta t^2}{2})),\ 0 \leq t < T_{\mathrm{p}}. \tag{4.5}$$

The transmit waveform is scaled before transmission so as to have the transmit power P_{r}. With this, the transmitted signal is

$$s(t) = \sqrt{P_{\mathrm{r}}} s_{\mathrm{r}}(t). \tag{4.6}$$

If the radar receiver has N_{r} antennas, let us denote the received signal on all antennas by a vector $\mathbf{x}(t) \in \mathbb{C}^{N_{\mathrm{r}}}$. The transmitted waveform arrives at

the nth antenna of the receiver with attenuation α and delay τ_n. The received signal on nth antenna is thus

$$[\mathbf{x}(t)]_n = \alpha s(t - \tau_n). \tag{4.7}$$

Let τ be the propagation time of the transmit signal that contains the delay due to distance. Further, let τ_n' be the additional time-delay of the wave propagating from the reference antenna to the nth antenna of the ULA. For an incoming signal that has angle θ relative to the broadside of the array, the delay τ_n' in a half wavelength spacing ULA is

$$\tau_n' = \frac{\sin\theta(n-1)}{2f_{\mathrm{r}}}. \tag{4.8}$$

With τ being the delay due to distance, and τ_n' being the additional delay, we can write the delay of the transmit waveform on antenna n as $\tau_n = \tau + \tau_n'$ [142].

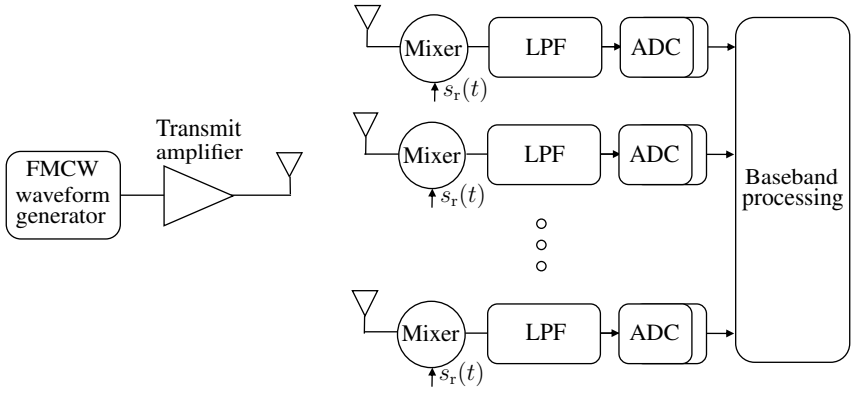

Figure 4.4: The FMCW radar system with multiple antennas at the receiver.

When the reference signal $s_{\mathrm{r}}(t)$ is known at the receiver, the echo signal $[\mathbf{x}(t)]_n$ is cross-correlated with the reference signal and passed through the low

pass filter (LPF) to obtain

$$[\mathbf{y}(t)]_n = [\mathbf{x}^*(t)]_n s_{\mathrm{r}}(t) = \sqrt{P}\alpha \exp(\mathrm{j}2\pi(f_{\mathrm{r}}\tau_n - \frac{\beta\tau_n^2}{2} + \beta\tau_n t)). \tag{4.9}$$

The term $\beta\tau_n$ is the constant frequency of the signal (called beat-frequency) that is used to estimate the range of the target. Further, $2\pi f_{\mathrm{r}}\tau_n - \pi\beta\tau_n^2$ is the constant phase of the signal. The variation of this phase across the chirps is used to estimate the Doppler. Let us collect the I samples of the signal in a matrix $\mathbf{Y} \in \mathbb{C}^{N_{\mathrm{r}} \times I}$. If $i \in \{1, 2, \cdots, I\}$ denotes the sample index, and T_{r} denotes the sampling time, then the ith sample on the nth antenna is

$$[\mathbf{Y}]_{n,i} = \sqrt{P}\alpha \exp(\mathrm{j}2\pi(f_{\mathrm{r}}\tau_n - \frac{\beta\tau_n^2}{2} + \beta\tau_n i T_{\mathrm{r}})). \tag{4.10}$$

Note that, so far we considered a single radar at the vehicle and a single reflector. As discussed previously, the vehicle is equipped with multiple radars. We assume that all the radars transmit at the same time. This is feasible as the radars mounted on a vehicle have exclusive field-of-view, and they do not need to be separated in time to avoid interference. We introduce superscripts to denote the radar number and the reflector number i.e., the signal received from the jth radar and the lth reflector is $\mathbf{Y}^{j,l}$. Further, let $\mathbf{N}$ be the additive white Gaussian noise with entries $\mathcal{CN}(0, \sigma_n^2)$. Then, we can write the superimposed radar received signal $\mathbf{Y}_{\mathrm{r}}$ as

$$\mathbf{Y}_{\mathrm{r}} = \sum_{j=1}^{J}\sum_{l=1}^{L} \mathbf{Y}^{j,l} + \mathbf{N}. \tag{4.11}$$

In this work, our objective is to configure the downlink of the mmWave communication system based on the spatial covariance matrix constructed

from (4.11). There are, however, two obstacles in this pursuit. First is that - so far - we have assumed that the reference signal $s_{\mathrm{r}}(t)$ is known at the receiver. In a typical passive radar, a static source illuminates the environment. The receiver has a dedicated channel through which the reference waveform is monitored and sampled. In our application, however, the source is mobile and it is not possible to have access to the reference signal of the source. The second obstacle is that angular information retrieved from radar covariance has a bias [37]. The impact of this bias is significant for a system with a large number of antennas. Specifically, due to a narrow beamwidth in a large antenna system, small pointing errors can result in a significant loss in link budget. In the following two sections, we address these two problems respectively.

4.6 Proposed radar receiver

The reference signal and the transmission time is required to estimate the range (through beat-frequency) and Doppler (through phase variations across chirps). In our application, however, we are interested in the spatial covariance of the radar received signal $\mathbf{R}_{\mathrm{r}} \in \mathbb{C}^{N_{\mathrm{r}} \times N_{\mathrm{r}}}$. The spatial covariance matrix, of the radar received signal (for a single target), can be estimated from the received signal $\mathbf{Y}$ in (4.10) as

$$\mathbf{R} = \frac{1}{I}\mathbf{Y}\mathbf{Y}^{*}. \tag{4.12}$$

If we define $\Delta\tau_{qp} = \tau'_q - \tau'_p$, then ignoring the contribution of noise, the covariance between the signal received on the qth antenna and the pth antenna

with perfect reference signal knowledge is

$$[\mathbf{R}_{\mathrm{r}}]_{q,p} = \frac{1}{I}\sum_{i=1}^{I} \exp(\mathrm{j}2\pi(f_c\Delta\tau_{qp} - \frac{\beta}{2}(2\tau + \tau'_q + \tau'_p)\Delta\tau_{qp} + \beta i T_{\mathrm{r}}\Delta\tau_{qp})). \quad (4.13)$$

As we are only interested in the spatial covariance, we propose a simple radar processing chain that does not require the reference signal and achieves the same covariance as in (4.13). To this end, let Δf be the frequency offset between the clock at the RSU and the vehicle, and ϵ be the phase-offset. Then, in the absence of the reference signal, we correlate the received signal with $\check{s}_{\mathrm{r}}(t) = \exp(\mathrm{j}\{2\pi(f_{\mathrm{r}} + \Delta f)t + \epsilon\})$. The received signal after correlation with $\check{s}_{\mathrm{r}}(t)$ and passing it through the LPF is

$$[\check{\mathbf{y}}(t)]_n = [\mathbf{x}^*(t)]_n \check{s}_{\mathrm{r}}(t) = \sqrt{P_{\mathrm{r}}}\alpha \exp(\mathrm{j}\{2\pi(f_{\mathrm{r}}\tau_n + \Delta f t - \frac{\beta(t-\tau_n)^2}{2}) + \epsilon\}). \quad (4.14)$$

With the proposed architecture, the frequency of the received signal $[\check{\mathbf{y}}(t)]_n$ is $\beta\tau_n + \Delta f - \frac{\beta t}{2}$ which is random (due to Δf) and time-varying (due to $\frac{\beta t}{2}$). Thus, the range of the target cannot be estimated by the proposed simplified receiver architecture. The phase of the received signal is $2\pi f_{\mathrm{r}}\tau_n - \pi\beta\tau_n^2 + \epsilon$, which is also random and varies from one chirp to another (as ϵ varies from one chirp to another). Thus, also, the Doppler of the target cannot be estimated by the proposed simplified receiver architecture. Note that, ith sample of the received signal on antenna n (collected in a matrix $\check{\mathbf{Y}} \in \mathbb{C}^{N_{\mathrm{r}} \times I}$) is

$$[\check{\mathbf{Y}}]_{n,i} = \sqrt{P_{\mathrm{r}}}\alpha \exp(\mathrm{j}2\pi(f_{\mathrm{r}}\tau_n + \Delta f i T_{\mathrm{r}} - \frac{\beta\tau_n^2}{2} - \frac{\beta i^2 T_{\mathrm{r}}^2}{2} + \beta\tau_n i T_{\mathrm{r}} + \epsilon)), \quad (4.15)$$

and the spatial covariance matrix based on (4.15) is

$$\check{\mathbf{R}}_{\mathrm{r}} = \frac{1}{I}\check{\mathbf{Y}}\check{\mathbf{Y}}^{*}. \tag{4.16}$$

It is easy to show that $[\check{\mathbf{R}}_{\mathrm{r}}]_{q,p} = [\mathbf{R}]_{q,p}$. This observation allows us to circumvent the requirement of the reference signal in our application without any loss in terms of spatial information. Note that, we have shown that the simplified architecture has the same spatial covariance as with perfect waveform knowledge in a single target scenario. This choice was made for ease of exposition, and similarly, it can be shown that the spatial covariance is the same for multiple target case also. Similar to (4.11), we define $\check{\mathbf{Y}}^{j,l}$ as the signal received from jth radar and lth reflector in the simplified architecture. Then, the superimposed signal for all the targets and all the radar transmitters is

$$\check{\mathbf{Y}}_{\mathrm{r}} = \sum_{j=1}^{J}\sum_{l=1}^{L}\check{\mathbf{Y}}^{j,l} + \check{\mathbf{N}}. \tag{4.17}$$

4.7 Radar bias correction

In [37], it was shown that the angle estimation based on FMCW radar is biased. Specifically, for a single point target at angle θ, the true and the estimated angles are related by [37]

$$\sin\hat{\theta} = (1 + \frac{B_{\mathrm{r}}}{2f_{\mathrm{r}}})\sin\theta, \tag{4.18}$$

in a noiseless scenario. For a system with a large number of antennas - where the beams are narrow - this multiplicative bias can have a significant impact

on the performance. As an example, note that the first-null of a ULA with N antennas is $2/N$ away from the main lobe (say centered at $\sin(\theta)$) [143]. For $N = 256$, we get $2/N = 7.8 \times 10^{-3}$. Similarly, for $f_{\mathrm{r}} = 76\,\mathrm{GHz}$, and $B_{\mathrm{r}} = 1.2\,\mathrm{GHz}$ (i.e., a fraction of bandwidth available in 76 GHz band), we have $\frac{B_{\mathrm{r}}}{2f_{\mathrm{r}}} = 7.9 \times 10^{-3}$. Thus, even in the noiseless case, the beamforming based on the biased estimate can imply a null in the direction of the true angle.

A similar error/mismatch appears in FDD systems. Assuming perfect angular reciprocity, the differences in the UL and DL covariance come only from the array response in the UL and DL. Assume that the array is a ULA with inter-element spacing set to half the DL wavelength. Further, let λ_{DL} and λ_{UL} denote the DL and UL wavelength, then the true and estimated angles in the UL will be related by

$$\sin\hat{\theta} = \frac{\lambda_{\mathrm{DL}}}{\lambda_{\mathrm{UL}}}\sin\theta. \tag{4.19}$$

Now beamforming based on the estimated angle is sub-optimal, especially for a large number of antennas as discussed earlier. Further, note that the biased angle information is recovered from covariance matrices. Covariance matrices, however, can be used for other purposes e.g., precoder/combiner design based on singular vectors of the covariance. As such, it is of interest to correct the covariance matrices directly rather than the angles estimated from the covariance matrices. This problem has been considered in the past for FDD systems and several strategies have been proposed e.g., [57, 144, 47, 59, 145].

Noting that the bias in the FMCW radar has the same form as of that in FDD, we use a covariance correction strategy, i.e., [47] in this work.

The strategy [47] is based on interpolation of the covariance for correction. The sampled radar covariance matrix $\check{\mathbf{R}}_{\mathrm{r}}$ is not necessarily Toeplitz. Therefore, to improve the estimate, we project $\check{\mathbf{R}}_{\mathrm{r}}$ to the Toeplitz, Hermitian, positive semi-definite cone $\mathbf{T}_{+}^{N}$, i.e.,

$$\hat{\mathbf{R}}_{\mathrm{r}} = \underset{\mathbf{X}\in\mathbf{T}_{+}^{N}}{\arg\min} \|\mathbf{X} - (\check{\mathbf{R}}_{\mathrm{r}} - \sigma_n^2\mathbf{I})\|_{\mathrm{F}}. \tag{4.20}$$

As $\hat{\mathbf{R}}_{\mathrm{r}}$ is Toeplitz Hermitian matrix, it is fully described by its first column which we denote as $\hat{\mathbf{r}}$.

For simplicity, let us denote the multiplication constant in (4.18) as $\gamma = (1 + \frac{B_{\mathrm{r}}}{2f_{\mathrm{r}}})$. Note that the vector $\hat{\mathbf{r}}$ are the samples of the covariance at $n \in \{0, 1, \cdots, N-1\}$. For correction, we need the samples at points $n/\gamma \ \forall n \in \{0, 1, \cdots, N-1\}$. This can be achieved by interpolation (note that as $\gamma > 1$, there is no need for extrapolation). As the vector $\hat{\mathbf{r}}$ is complex, we interpolate the magnitude and phase separately. The magnitude of $\hat{\mathbf{r}}$ is smooth and *spline* interpolation, followed by resampling, will provide good performance as shown in Fig. 4.5a. The phase of $\hat{\mathbf{r}}$ can be unambiguously determined only in the interval $(-\pi, \pi]$ as shown in Fig. 4.5b. That said, the phase changes slowly with n, and hence the jumps of 2π can be observed. For interpolation of phase, the actual phase needs to be reconstructed. Hence, first, the observed phase is *unwrapped* as shown in Fig 4.5c, and then spline interpolation followed by resampling is used. We can then obtain the corrected covariance vector

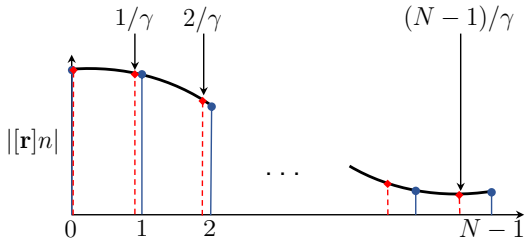

(a) Observed and resampled magnitude of the covariance vector $\mathbf{r}$ for covariance correction.

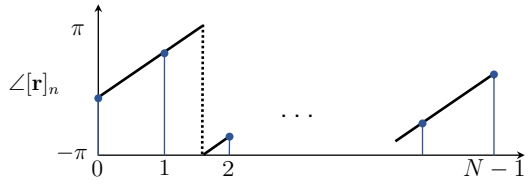

(b) Observed wrapped phase of the covariance vector $\mathbf{r}$.

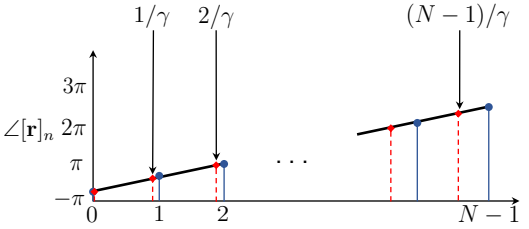

(c) Unwrapped and resampled phase of the covariance vector $\mathbf{r}$.

Figure 4.5: The covariance correction strategy that (i) resamples the covariance vector magnitude, (ii) unwraps and resamples the phase of the covariance vector, and (iii) uses Toeplitz completion of the resampled covariance vector to obtain the corrected covariance.

$\hat{\mathbf{r}}_{\mathrm{c}}$ by combining the resampled magnitude and phase. Finally, the corrected covariance matrix $\hat{\mathbf{R}}_{\mathrm{c}}$ is obtained by Toeplitz completion $\hat{\mathbf{R}}_{\mathrm{c}} = \mathcal{T}(\hat{\mathbf{r}}_{\mathrm{c}})$.

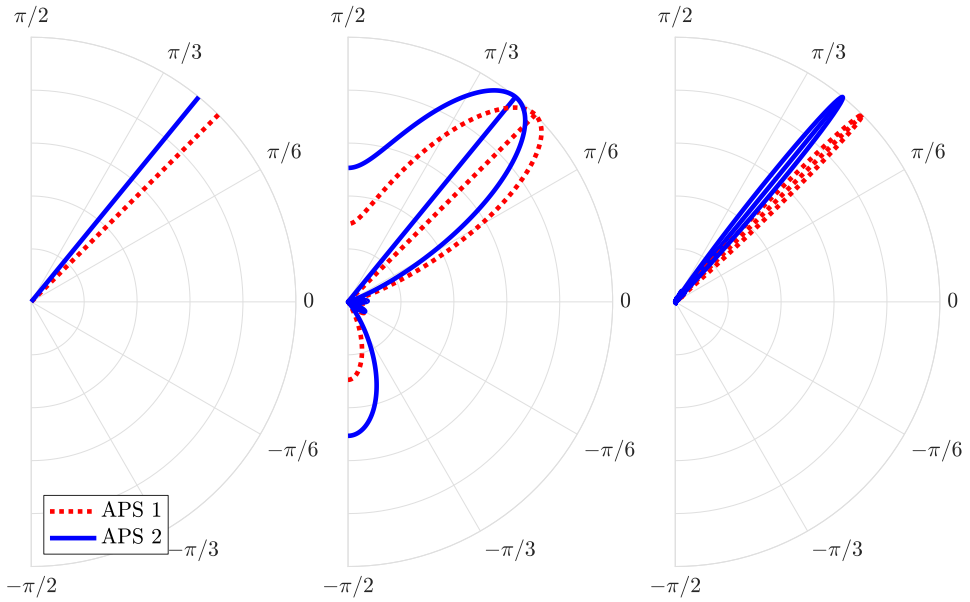

(a) Two over-the-air APS.

(b) Overlaid beams for a 4 antenna array.

(c) Overlaid beams for a 32 antenna array.

Figure 4.6: Over the air azimuth power spectra and observed power spectra through arrays of 4 antenna elements and 32 antenna elements.

4.8 Similarity metric to measure spatial congruence

In this work, we are proposing to use the information retrieved from radar to configure the mmWave communication link. This strategy, however, will be only useful if the spatial characteristics of the radar and the communication channel are congruent. Roughly speaking, we are interested in the similarity of APS of the radar received signals and communication channels. In our application, the differences in radar and communication APS will stem from (i) different operating frequencies of radar and communication, and (ii) different locations and field-of-views of communication and radars on the vehi-

cle - hence the different probability of blockage. We, however, need the radar and communication APS to be as similar as possible. That said, we also need a notion of quantifying this similarity. Furthermore, we need a similarity metric that is meaningful from the communication system point of view, i.e., the similarity metric should have a transparent connection with a communication system metric e.g., rate. Such a similarity metric to compare the APS will be useful beyond our current application. The metric will be useful, for example, to assess the accuracy of the angular reciprocity assumption in FDD. The proposed similarity metric can also be used to validate the assumption that sub-6 GHz and mmWave channels are spatially similar. This assumption is used in a recent line of work [41, 46] to reduce the mmWave training overhead using sub-6 GHz information.

To assess the similarity, one possibility is to compare over-the-air APS as shown in Fig. 4.6a. Note that over-the-air APS is system independent, i.e., it does not take into consideration how many antennas are used in a system. Directly comparing over the air APS, however, may not be most prudent. To motivate this, let us consider a toy example, where we are interested in measuring the similarity of the APS1 (shown with dotted line) and APS2 (shown with solid line). More specifically, consider that we observe APS1 (in our case through radar), whereas the actual spectrum is APS2 (in our case the APS of communication). Now, we consider two cases; (i) a 4 antenna system, and (ii) a 32 antenna system. The beam-patterns of 4 element ULAs pointing in the directions of the spectra are shown in Fig. 4.6b. In this case,

the information provided by APS1 is useful for beamforming on APS2. This is because the beam-pattern has a significant gain in the direction of APS2. Now for 32 antennas (the beam-patterns for 32 element ULAs are shown in Fig. 4.6c), the information provided by APS1 is not particularly useful for beamforming on APS2. This is because the beam-pattern directed towards APS1 does not have a high gain in the direction of APS2. Thus, a meaningful measure of similarity needs to take the system dimension, i.e., the number of antennas, into consideration.

To define the similarity metric, assume that we want to measure the similarity of two N point spectra $\mathbf{d}_1$ and $\mathbf{d}_2$. Consider the index set $\mathcal{I}_1$ ($\mathcal{I}_2$) of cardinality $L \leq N$ that contains indices of L largest entries of $\mathbf{d}_1$ ($\mathbf{d}_2$). Then, we define a similarity metric

$$\mathrm{S}_{1\to 2}(L,N) = \frac{\sum_{i\in\mathcal{I}_1} \mathbf{d}_2[i]}{\sum_{i\in\mathcal{I}_2} \mathbf{d}_2[i]}. \tag{4.21}$$

To explain the meaning of the metric, we use the help of Fig. 4.7. In the denominator, we have the sum of L largest spectral components of $\mathbf{d}_2$, whereas in the numerator we have the L components of $\mathbf{d}_2$ that correspond to the L largest spectral components of $\mathbf{d}_1$. It is clear that $0 \leq \mathrm{S}_{1\to 2}(L,N) \leq 1$. For given spectra, as we sum over L largest spectral components, $\mathrm{S}_{1\to 2}(L,N)$ will generally increase with L (for fixed N) and $\mathrm{S}_{1\to 2} = 1$ for $L = N$. Also, $\mathrm{S}_{1\to 2}(L,N)$ will generally decrease with N (for fixed L). Also note that the metric is asymmetric, i.e., it is not necessary that $\mathrm{S}_{1\to 2}(L,N) = \mathrm{S}_{2\to 1}(L,N)$. Finally, note that we have used the notation $\mathrm{S}_{1\to 2}(L,N)$ to include all the

relevant parameters. When there is no ambiguity, we will simply use S to denote the similarity metric. Further, note that from a system's point of view N is related to the number of antennas, and L is related to the the number of transmitted streams i.e., N_s.

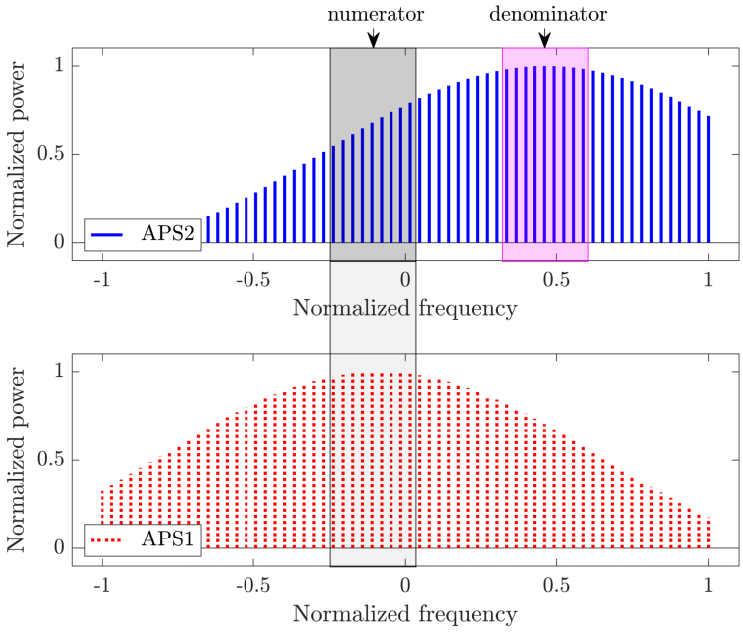

Figure 4.7: Intuitive explanation of the similarity metric (4.21). The denominator is the sum of a few strongest component of APS2, whereas the numerator is the sum of a few components of APS2, corresponding to the strongest components of APS1.

We now relate the proposed similarity metric to RPE [48, 49]. Consider two channels with spatial covariance matrices $\mathbf{R}_1$ and $\mathbf{R}_2$. Further consider that $\mathbf{F}_1$ ($\mathbf{F}_2$) contains the L columns of the DFT matrix corresponding to the L largest spectral components of the channel 1 (2). Then an alternative way

to write the proposed similarity metric (4.21) is

$$\mathrm{S} = \frac{\mathrm{tr}(\mathbf{F}_1^* \mathbf{R}_2 \mathbf{F}_1)}{\mathrm{tr}(\mathbf{F}_2^* \mathbf{R}_2 \mathbf{F}_2)}. \tag{4.22}$$

The equivalence between (4.21) and (4.22) becomes clear when we note that the APS $\mathbf{d}$ can be written as $\mathbf{d} = \mathrm{diag}(\mathbf{F}^* \mathbf{R} \mathbf{F})$. Further, if $\mathbf{U}_1$ ($\mathbf{U}_2$) are L singular vector of $\mathbf{R}_1$ ($\mathbf{R}_2$) corresponding to L largest singular values, then the RPE is defined as [48, 49]

$$\mathrm{RPE} = \frac{\mathrm{tr}(\mathbf{U}_1^* \mathbf{R}_2 \mathbf{U}_1)}{\mathrm{tr}(\mathbf{U}_2^* \mathbf{R}_2 \mathbf{U}_2)}. \tag{4.23}$$

In the special case, where the AoAs of all the paths fall on the DFT grid, it is easy to see that the proposed metric and the RPE are the same. This is because, for the on-grid case, vectors of Fourier basis are valid singular vectors. Therefore $\mathbf{U}_1$ ($\mathbf{U}_2$) and $\mathbf{F}_1$ ($\mathbf{F}_2$) are the same, and the similarity metric in (4.22) is the same as RPE in (4.23). This also implies that asymptotically (i.e., as $N \to \infty$), the proposed similarity metric is the same as the RPE. This is because one way to interpret the asymptotic case is to have a continuous DFT grid and hence all AoAs fall on-grid. It is, however, difficult to analytically relate the proposed metric to the RPE in the general off-grid case. In simulations, however, we study this off-grid scenario.

Finally, note that in [48], the RPE was related to the relative rate. To understand the relative rate, consider that true covariance is $\mathbf{R}_2$ (in our case the communication channel covariance), whereas we have access to $\mathbf{R}_1$ (in our case through radar). The relative rate is then the ratio of the achievable rate

given $\mathbf{R}_1$ to the achievable rate given $\mathbf{R}_2$. Particularly, in [48], it was shown that in low SNR setting the RPE is a good approximation of the relative rate. With this connection and the connection between the similarity metric and RPE, we can conclude that the proposed similarity metric also directly relates to the relative rate. To conclude, we proposed a similarity metric to compare two power spectra that relates directly to the relative rate.

4.9 Simulation results

In this section, we provide simulation results to verify the ideas presented in this work. We start by discussing the simulation setup in detail. Then, we present results to show the utility of bias correction strategy presented in Section 4.7, and to numerically study the relationship between similarity metric (presented in Section 4.8) and RPE for the off-grid scenario. Finally, we present results to verify the potential of using passive radar to configure mmWave links.

Material properties for ray-tracing: For all experiments, we assume that the communication system operates in the 73 GHz band, and the radar operates in the 76 GHz band. We use Wireless Insite [146] for ray-tracing simulations. The simulation environment is shown in Fig. 4.8a. This is an urban environment with buildings on both sides of the road. The color of a building corresponds to its height through a red-green-blue color scale with red representing high and blue representing low. The total length of the road is around 200 m. The buildings are made of concrete. The relative per-

mittivity of concrete is 5.31 and conductivity is $1.0509\,\mathrm{S\,m^{-1}}$ at 73 GHz (i.e., communication band), and $1.0858\,\mathrm{S\,m^{-1}}$ at 76 GHz (i.e., radar band) [147, Table 3]. The road surface is made of asphalt with relative permittivity 3.18 and conductivity $0.4061\,\mathrm{S\,m^{-1}}$ at 73 GHz, and $0.4227\,\mathrm{S\,m^{-1}}$ at 76 GHz [148]. The root-mean-square (RMS) surface roughness for concrete is 0.2 mm and for asphalt is 0.34 mm [148, Table 1]. Wireless Insite also models the diffuse scattering effects. The level of diffuse scattering is controlled using a scattering coefficient with valid values in the range $[0, 1]$ [149]. We use the scattering coefficient of 0.4 for concrete [149]. For asphalt, note that the RMS surface roughness is higher than concrete, and as diffuse scattering increases with surface roughness [150], we choose the scattering coefficient to be 0.5. Further, some of the diffused power becomes cross-polarized relative to the polarization of the incident ray. In Wireless Insite, this fraction is controlled using the cross-polarization coefficient that has a valid range $[0, 0.5]$ [149]. We chose the cross-polarization to be half the diffuse scattering coefficient for both concrete and asphalt. Finally, the vehicles on the road are made of metal i.e., perfect electric conductor.

Vehicle size and distribution: There are two types of vehicles on the road. Vehicles of size $5 \times 2 \times 1.6$m that represent cars, and vehicles of size $13 \times 2.6 \times 3$m that represent trucks [136, 6.1.2]. There are 80% cars and 20% trucks on the road. There are a total of four lanes, each 3.5 m wide. All the vehicles inside a lane have the same speed. The lane-speeds s_ℓ are 60, 50, 25, and $15\,\mathrm{km\,h^{-1}}$. The fraction of cars and trucks, lane widths, and

the lane speeds are the option B for Urban scenarios in [136, 6.1.2]. Let X be an exponential random variable with mean $\mu = s_\ell \times 2\,\mathrm{s}$ (where s_ℓ is in $\mathrm{m\,s^{-1}}$). Then, the distance between the rear bumper of a vehicle and the front bumper of the following vehicle is $\max(2, x)$ [136, 6.1.2]. Note that, the data collected from Wireless Insite is for a time snapshot. As such, the only role of the speed is in calculating inter-vehicle distances. All the results presented in this section are averaged over 1000 random snapshots, where the vehicles are placed independently in each snapshot according to the mentioned criterion.

Antenna locations on vehicle and RSU: The RSU (shown in Fig. 4.8b) has a height of the 5 m [136, 6.1.4]. The radar and communication arrays on the RSU are horizontally aligned and are vertically separated by 10 cm. The RSU arrays are down-tilted so as to face the center of the four lanes. The ego-vehicle has 4 communication antenna arrays at the height of 1.6 m [136, 6.1.2], one on each side as shown in Fig. 4.8c [136, Table 6.1.4-9]. The radars on the vehicle are placed at the height of 0.75 m. The front radars on the right and left side have 10° rotation towards the front. Similarly, the back radars on the right and left side have 10° rotation towards the back. The location, height, and the rotations are the numbers chosen to mimic Audi A8 MRRs [137]. All antenna elements have 120° 3 dB beamwidth, and 150° 3 dB first null beamwidth (both in E and H-plane). This choice is justified as practical ULAs also have a field-of-view of around 120°. We select the ego-vehicle from the vehicles on the road uniformly albeit inside the field-of-view of the RSU array.

Communication system parameters: We use $P_{\mathrm{c}} = 30$ dBm, and $B_{\mathrm{c}} = 1\,\mathrm{GHz}$ bandwidth for the communication system. We use the raised-cosine filter with a roll-off factor 0.4 for pulse shaping. Based on the RMS delay-spread of the channels obtained through ray-tracing, the bandwidth, and the roll-off factor, the number of time-domain taps required can be calculated to be $D = 512$. We use a cyclic-prefix (CP) of length $D - 1$. Further, we choose the number of sub-carriers to be $K = 2048$, i.e., the useful part of the OFDM symbol is almost $4\times$ the CP. The ULAs used in the communication system have half-wavelength inter-element spacing.

Radar parameters: We consider the chirp period of $T_{\mathrm{p}} = 500\,\mu\mathrm{s}$, $I = 1024$ samples in a chirp, and 128 chirps for radar processing. The transmit power is $P_{\mathrm{r}} = 30$ dBm and the bandwidth is $B_{\mathrm{r}} = 1\,\mathrm{GHz}$. With these parameters the chirp rate is $\beta = 2\,\mathrm{GHz\,ms^{-1}}$. For simplified receiver architecture discussed in Section 4.6, we select $\Delta f \sim \mathcal{U}[0, f_{\max}]$, with $f_{\max} = 3\,\mathrm{MHz}$, which is around 40 parts-per-million (ppm) at 76 GHz. The phase offset is $\epsilon \sim \mathcal{U}[0, 2\pi]$. The ULA used on the RSU for radar has half-wavelength inter-element spacing. In all experiments, the number of antenna elements in the radar and communication arrays at the RSU are same.

We modeled the optimization problem (4.20) using YALMIP [151] in MATLAB, and solved using the MOSEK [152] solver. We noticed that the solutions were not accurate when the covariance matrices had very small entries i.e., on the order of 10^{-11}. Thus, we normalized the covariance matrices to have unit Frobenius norm before solving the problem (4.20).

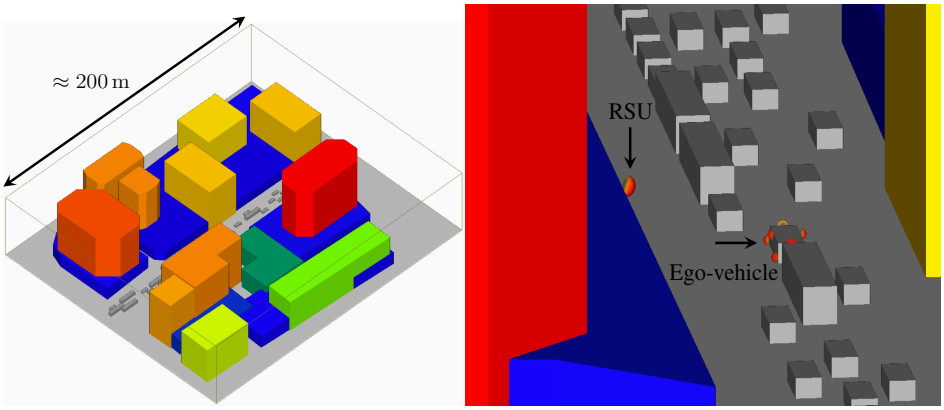

(a) The ray-tracing setup of length around 200 m.

(b) RSU and a randomly selected ego-vehicle.

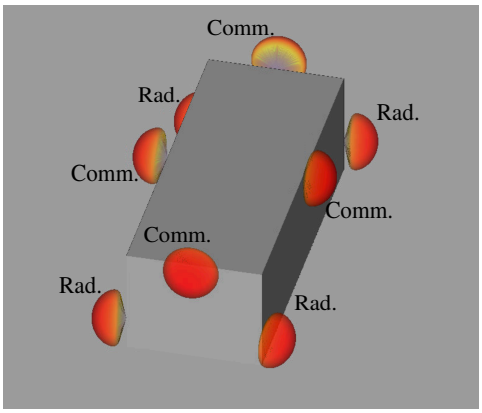

(c) Four communication arrays and four radars on the ego-vehicle.

Figure 4.8: The ray-tracing setup simulation in Wireless Insite with buildings of various heights, the RSU, and vehicles dropped in four lanes on the road.

We first demonstrate the impact of the bias (discussed in Section 4.7) on the performance of FMCW radar and the benefit of bias correction. Note that, in the setup described above, there are several sources of dissimilarity between radar and communication i.e., different operating frequencies, different location of the radar and communication antennas on the vehicle, the bias

in FMCW radar, and the thermal noise. To isolate only the impact of bias, we start with a simple scenario. First, the radar and the communication arrays on the RSU are collocated (i.e., horizontally and vertically aligned). We also assume a single antenna array on the vehicle. The radar on the vehicle is colocated with the communication array. This assumption takes away the dissimilarity due to different locations of the antennas. Second, we assume that the radar and communication systems operate in the same band to take out the differences due to the operating frequency. Third, for the first two experiments, we ignore the thermal noise. With this, the only remaining sources of dissimilarity is the bias in FMCW radar. We show the similarity in the APS of radar and communication as a function of the number of antennas N for ($N_{\mathrm{s}} = 1$) in Fig. 4.9. We also show the similarity after correcting the bias. In addition, we show the results for RPE before and after correction. We can see from the similarity metric results, as well as the RPE results, that correcting the bias is helpful as it increases the similarity as well as RPE. We show the same result for $N_{\mathrm{s}} = 4$ in Fig. 4.10. We note that the similarity and RPE increase with N_{s}. From this result also we can see that bias correction is helpful. Therefore, here onwards all the radar results are presented for the corrected case.

In the next experiment, we study the similarity of radar and communication in a realistic setup as discussed in the earlier parts of this section. In this experiment, we study $N_{\mathrm{s}} = 1$ as well as $N_{\mathrm{s}} = 4$ case. As there are four communication arrays on the vehicle, there are four communication channels.

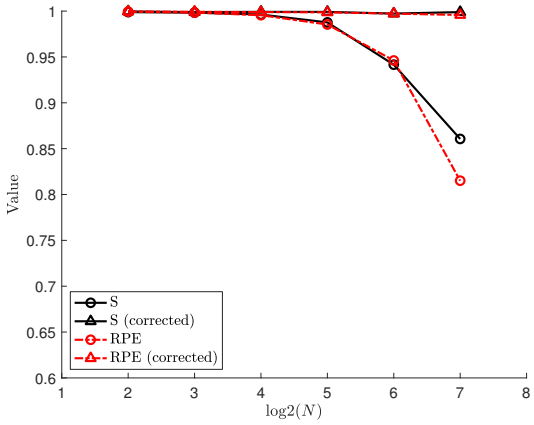

Figure 4.9: The similarity metric S and RPE as a function of the number of antennas N for $N_{\mathrm{s}} = 1$. The results are for a simplified case where the radar and communication arrays are collocated at the RSU and the vehicle and both systems operate on the same frequency.

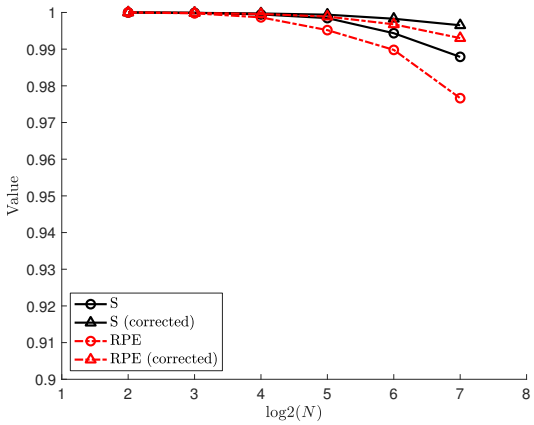

Figure 4.10: The similarity metric S and RPE as a function of the number of antennas N for $N_{\mathrm{s}} = 4$. The results are for a simplified case where the radar and communication arrays are collocated at the RSU and the vehicle and both systems operate on the same frequency.

We show the similarity results for the communication channel that has a path with the highest power (typically a LOS antenna array). The results of this

experiment are shown in Fig. 4.11. We can see that the similarity (and the RPE) between communication and radar decreases with the number of antennas N. Furthermore, the similarity (and RPE) increase with the number of streams N_{s}. Finally, the similarity metric and RPE follow the same trend, i.e., the similarity metric and RPE are closely related even for the general off-grid case.

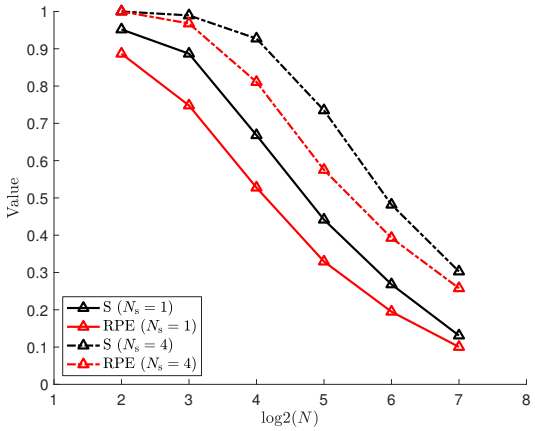

Figure 4.11: The similarity metric S and RPE as a function of the number of antennas N for $N_{\mathrm{s}} = 1$ and $N_{\mathrm{s}} = 4$. The results show that the similarity decreases with N and increases with N_{s}, and further similarity and RPE follow the same trend.

Now, we conduct an experiment to study the benefit of using radar data in a mmWave communication system. For this experiment, we consider a single RF-chain at the RSU, and one chain per receive array at the vehicle. Therefore only single stream transmission is possible, i.e., $N_{\mathrm{s}} = 1$. We consider that 2-bit phase-shifters are used at the RSU and the vehicle. The radar and the communication system have 128 antennas at the RSU, and there are 16 antennas each in vehicle arrays. We use an approximation

of DFT codebooks based on 2-bit phase-shifters [41] at the vehicle and the RSU. The nth codeword in the RSU codebook is thus a 2-bit approximation of $\frac{1}{\sqrt{N_{\text{RSU}}}}\mathbf{a}_{\text{RSU}}(\arcsin(\frac{2n-N_{\text{RSU}}-1}{N_{\text{RSU}}}))$, $n = 1, \cdots, N_{\text{RSU}}$. The codebooks for the vehicle are defined in a similar manner. For this experiment, we use rate as a metric. To define the rate, let us say T_{train} OFDM blocks are used for training, whereas the coherence time of the channel is $T_{\text{coh.}}$ blocks. Then $(1 - \frac{T_{\text{train}}}{T_{\text{coh.}}})$ is the fraction of blocks left for data transmission. With this, the rate is

$$R = \frac{B_{\text{c}}}{K}\big(1 - \frac{T_{\text{train}}}{T_{\text{coh.}}}\big)\sum_{k=1}^{K}\log_2\big(1 + \frac{P}{\sigma_{\text{e}}^2 K}\sum_{a=1}^{A}|\mathbf{w}^{(a)*}\mathbf{H}^{(a)}[k]\mathbf{f}|^2\big). \tag{4.24}$$

For this experiment, we compare three strategies. First is exhaustive-search in which all the codewords in the DFT codebooks of the RSU and the vehicle arrays are tried. If we assume that measurements on all the vehicle arrays are made simultaneously, the overhead of exhaustive-search is $N_{\text{RSU}} \times N_{\text{V}}$ OFDM blocks. There will be only one beam at the RSU that will be used to communicate to all the arrays of the vehicle. As such, at the RSU, we select a codeword that provides highest SNR (averaged across all the vehicle arrays). On the vehicle, we choose a codeword for each array that provides highest SNR for the selected codeword at the RSU.

The second strategy is location-assisted. In this strategy, we assume that the location of the vehicle is obtained through global navigation satellite system (GNSS). There is an error of 10 m in the estimated vehicle location [32]. This vehicle location is communicated to the RSU using a low-rate link, e.g., at sub-6 GHz frequencies. Based on the reported location of the vehicle, and

the expected error in vehicle location, only a subset of the beams are tried at the RSU. Note that, location of the center of the vehicle is reported. As the vehicle has length 5 m, the front and rear antennas are ± 2.5 m away from the center. We consider this additional 2.5 m offset while constructing the subset based on the location information. Specifically, assume that the true angular location of the vehicle - measured from the broadside of the RSU array- is ϕ. Furthermore, assume that the vehicle location estimate available to the RSU is $\hat{\phi}$, and $|\phi - \hat{\phi}| < \Delta\phi$, where $\Delta\phi$ represents the error of the vehicle localization mechanism. In our case, this error is around 12.5 m. The RSU reduces the codebook based on the angular information i.e., $\hat{\phi}$ and $\Delta\phi$. To formalize this, let us construct an index set $\mathcal{L}$ such that $n \in \mathcal{L}$ if

$$\sin(\hat{\phi} - \Delta\phi) - \frac{1}{N_{\text{RSU}}} \leq \frac{2n - N_{\text{RSU}} - 1}{N_{\text{RSU}}}, \tag{4.25}$$

and

$$\sin(\hat{\phi} + \Delta\phi) + \frac{1}{N_{\text{RSU}}} \geq \frac{2n - N_{\text{RSU}} - 1}{N_{\text{RSU}}}. \tag{4.26}$$

The addition (and subtraction) of $\frac{1}{N_{\text{RSU}}}$ in (4.25) (and (4.26)) ensures that the index set $\mathcal{L}$ has at least one entry even when $\Delta\phi = 0$, i.e., perfect vehicle localization. The above inequalities can be written simply as a compound inequality

$$\sin(\hat{\phi} - \Delta\phi) + 1 \leq \frac{2n}{N_{\text{RSU}}} \leq \sin(\hat{\phi} + \Delta\phi) + 1 + 2/N_{\text{RSU}}. \tag{4.27}$$

The RSU thus only uses the codewords indexed by $\mathcal{L}$.

The third strategy is radar-assisted. In this strategy, first, we find the peak in the radar APS. Then we train using a few codewords that point in the directions around the radar APS peak. For the rate results, the number of codewords tried for the radar-assisted strategy is the independent variable. First, we present the results for the case when $T_{\text{coh.}} \to \infty$ in Fig. 4.12. We can see that the radar-assisted strategy can achieve the same rate as exhaustive-search. This rate, however, is achieved by training through 80 codewords, i.e., around 38% savings in overhead. Note that, on average that location assisted strategy required 51 codewords, but did not achieve the rate of exhaustive-search. Second, we present the results for a highly dynamic channel with $T_{\text{coh.}} = 4N_{\text{RSU}}N_{\text{V}}$ OFDM blocks in Fig. 4.13. Note that, we expect the rate of all the strategies to drop in highly dynamic channels. Strategies with low-overhead, however, are expected to be advantageous in a highly dynamic channel as low training overhead implies larger duration for the data transmission. The results confirm this observation, as both the location-assisted and radar-assisted strategies perform better than the exhaustive-search. The radar-assisted strategy obtains a rate higher than exhaustive-search with only 50 measurements, implying an overhead reduction of 60%. Note that the rate of the radar-assisted strategy starts to decrease as we keep on increasing the number of measurements. The reason is that once we do enough measurements to find the best beam, additional measurements only increase the overhead and do not improve beam-training. One observation, however, is that the radar-assisted strategy only reaches the rate of the location-assisted strategy. The

reason is that the ego-vehicle is in LOS with the RSU in most of the random drops. In LOS channels beam-training based on location information is expected to perform well.

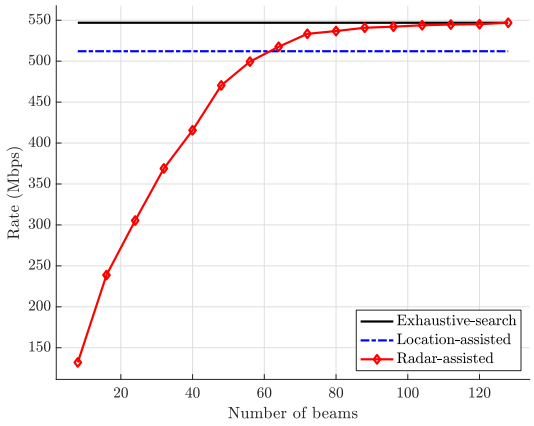

Figure 4.12: Rate versus the number of beams for $T_{\text{coh.}} \to \infty$. The proposed radar-assisted strategy achieves the rate of exhaustive-search with fewer measurements, whereas the location-assisted strategy fails to reach the rate of exhaustive search.

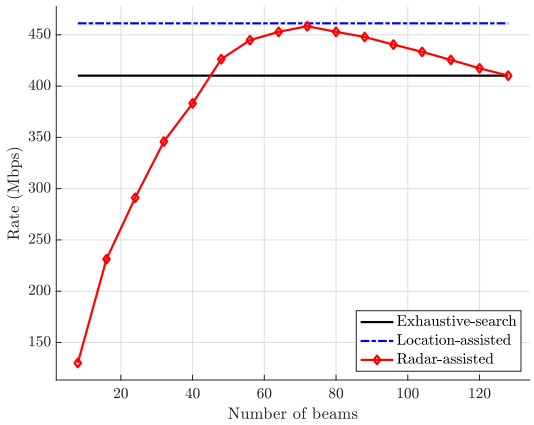

Figure 4.13: Rate versus the number of beams for $T_{\text{coh.}} = 4N_{\text{RSU}}N_{\text{V}}$. The low training overhead radar-assisted and location-assisted strategies have a better rate than the exhaustive-search strategy.

We now study the performance of the proposed strategy in NLOS scenario. Specifically speaking, only 179 out of the 1000 drops were such that none of the communication antennas on the vehicle had a direct path to the RSU. We now present the rate results averaged over these 179 drops. The results for $T_{\text{coh.}} \to \infty$ are presented in Fig. 4.14. We observe that in comparison with the earlier case (i.e., when most of the channels were LOS), the radar-assisted strategy can achieve a higher rate than the location-assisted strategy with fewer measurements. Further, the location-assisted strategy fails to achieve the exhaustive-search rate, whereas, the radar-assisted strategy achieves almost the exhaustive-search rate with 70 measurements. The results for $T_{\text{coh.}} = 4N_{\text{RSU}}N_{\text{V}}$ are presented in Fig. 4.15. We observe that the radar-assisted strategy can achieve a rate better than the exhaustive-search and location assisted strategy with only 30 measurements, implying an overhead reduction of around 77%.

4.10 Conclusion

We used the spatial covariance of the passive radar at the RSU to help establish the mmWave communication link. We proposed a simplified radar receiver that did not require the transmit waveform. Using the proposed architecture, the spatial covariance can be recovered perfectly, however, due to the lack of waveform knowledge the range and Doppler cannot be recovered. Further, we noticed a similarity in the bias that appears in FMCW radars to the well-studied problem in FDD systems and subsequently used one covariance

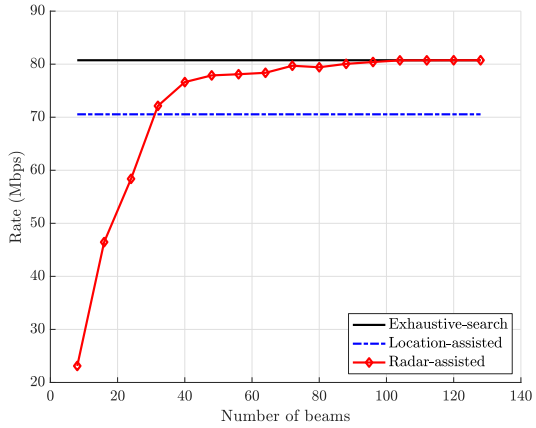

Figure 4.14: Rate versus the number of beams for $T_{\text{coh.}} \to \infty$ in NLOS channel. The proposed radar-assisted strategy achieves the rate of exhaustive-search with fewer measurements, whereas the location-assisted strategy fails to reach the rate of exhaustive search.

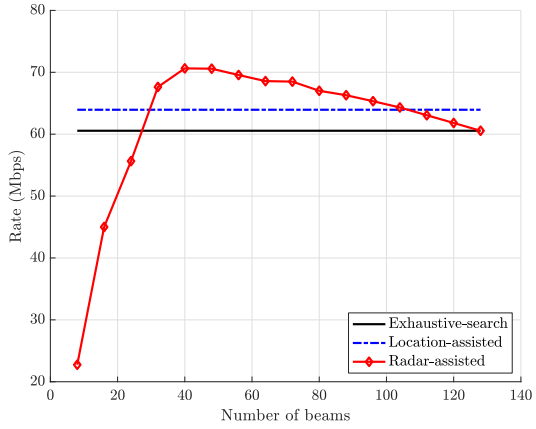

Figure 4.15: Rate versus the number of beams for $T_{\text{coh.}} = 4N_{\text{RSU}}N_{\text{V}}$. The radar-assisted strategy achieves a rate better than the location-assisted strategy and exhaustive-search with only 30 measurements, implying a 77% overhead reduction.

correction strategy from FDD literature to correct the bias in FMCW radars.

In addition, to compare the similarity of two APS, we proposed a similarity

metric that is identical to the RPE for the on-grid case and relates directly to the relative rate. The simulation results based on ray-tracing data showed that bias correction is important and increases the similarity in radar and communication APS. The rate results showed that the radar-assisted strategy can reduce the training overhead by around $30 - 75\%$ depending on the scenario. Higher gains for the radar-assisted strategy were observed in highly-dynamic channels and in NLOS scenarios.

Chapter 5

Conclusion

The main theme of this dissertation is the use of out-of-band information in mmWave link configuration. First, we outlined a method to incorporate spatial information obtained from a sub-6 GHz communication channel in mmWave beam-selection for analog mmWave systems. Second, we outlined two methods to construct mmWave covariance using sub-6 GHz information. The first method is a direct translation of sub-6 GHz covariance to mmWave covariance, and the second method is to aid the in-band compressed covariance estimation with sub-6 GHz information. The mmWave covariance obtained using the proposed methods is used for hybrid precoding in mmWave systems. Third, used the spatial covariance of the passive radar at the RSU to establish the mmWave communication link. We proposed a simplified radar receiver that did not require the transmit waveform. We proposed a bias correction strategy for the bias that appears in the FMCW radar. The simulation results based on ray-tracing data showed that bias correction is important and increases the similarity in radar and communication APS. The results using sub-6 GHz and radar information prove our thesis statement that

Out-of-band aided mmWave link configuration has a low training

overhead in comparison with in-band only link configuration.

In the next section, we summarize the main contributions presented in this dissertation.

5.1 Summary

Chapter 2: We used the sub-6 GHz spatial information to reduce the training overhead of beam-selection in an analog mmWave system. We formulated the compressed beam-selection problem with the codebooks generated from low-resolution phase-shifters. We used a weighted sparse recovery approach with structured random codebooks to incorporate out-of-band information. We proposed a method to generate multi-band frequency dependent channels according to the frequency dependent channel behavior observed in the prior work. We used the proposed multi-band frequency dependent channels to evaluate the achievable rate of the proposed approach. From the rate results, we concluded that the training overhead of in-band only compressed beam-selection can be reduced substantially if out-of-band information is used.

Chapter 3: We used the sub-6 GHz covariance to predict the mmWave covariance. We presented a parametric approach that relies on the estimates of mean angle and angle spread and their subsequent use in theoretical expressions of the covariance pertaining to a postulated power azimuth spectrum. To aid the in-band compressed covariance es-

timation with out-of-band information, we formulated the compressed covariance estimation problem as weighted compressed covariance estimation. For a single path channel, we bounded the loss in SNR caused by imperfect covariance estimation using singular-vector perturbation theory. The out-of-band covariance translation and out-of-band aided compressed covariance estimation had better effective achievable rate than in-band only training, especially in low SNR scenarios. The out-of-band covariance translation eliminated the in-band training but performed poorly (in comparison with in-band training) when the SNR of the mmWave link was favorable. The out-of-band aided compressed covariance estimation reduced the training overhead of the in-band only covariance estimation by 3x.

Chapter 4: We used the spatial covariance of the passive radar at the RSU to help establish the mmWave communication link. We proposed a simplified radar receiver that did not require the transmit waveform. Using the proposed architecture, the spatial covariance can be recovered perfectly, however, due to the lack of waveform knowledge the range and Doppler cannot be recovered. Further, we noticed a similarity in the bias that appears in FMCW radars to the well-studied problem in FDD systems and subsequently used one covariance correction strategy from FDD literature to correct the bias in FMCW radars. In addition, to compare the similarity of two APS, we proposed a similarity metric that is identical to the RPE for the on-grid case and relates directly

to the relative rate. The simulation results based on ray-tracing data showed that bias correction is important and increases the similarity in radar and communication APS. The rate results showed that the radar-assisted strategy can reduce the training overhead by around $30 - 75\%$ depending on the scenario. Higher gains for the radar-assisted strategy were observed in highly-dynamic channels and NLOS scenarios.

5.2 Future Research Directions

In this section, we describe several research directions related to the work represented in this dissertation.

5.2.1 Experimental verification of the proposed strategies

In this dissertation, we proposed several out-of-band assisted mmWave link configuration strategies. The numerical results for sub-6 GHz assisted strategies are based on the channels generated via multi-frequency channel model proposed in Chapter 2. The performance of the proposed strategy on these synthetic channels is promising. It, however, is an interesting direction to test the proposed sub-6 GHz assisted strategies on measured channels rather than synthesized channels. This can be done by collecting the joint sub-6 GHz and mmWave measurements and subsequently testing the proposed algorithms on the collected data. In [31, 63] measured channels were used to demonstrate the potential of sub-6 GHz information for mmWave. That said, the strategies in [31, 63] are limited to LOS channels, whereas the strategies

proposed in this dissertation are expected to perform well in NLOS channels also. Another possibility is to prototype a joint sub-6 GHz and mmWave communication system and perform mmWave link configuration with the aid of sub-6 GHz channels.

The results for passive radar assisted covariance estimation presented in Chapter 4 were based on ray-tracing data. Though ray-tracing is expected to give channels that are comparable to measurements [153], the limitations of the actual hardware can be accurately captured using prototyping. An example is that we assume that the radar and communication arrays are perfectly aligned, which will be difficult to achieve in practice. Further, the array calibration typically assumed in simulations will not hold in practice. As such, it is an interesting direction to verify the results of Chapter 4 by prototyping a co-located passive radar and mmWave communication system.

In Chapter 2, we presented a multi-frequency channel model to obtain the sub-6 GHz and mmWave channels. The channel model was proposed based on the multi-frequency channel characteristics observed in the past. As such, the proposed model appears more practical compared to the 3GPP channel model that is based on simplistic assumptions like same clusters at sub-6 GHz and mmWave [154]. That said, the proposed model needs to be calibrated with the measurements to give it more credence.

5.2.2 Extension to low resolution ADC based architectures

Some of the results presented in this dissertation were based on an analog mmWave architecture based on phase-shifters, whereas some of the results were based on hybrid analog-digital architecture. The advantage of analog architecture is low cost and low power consumption, whereas hybrid analog-digital architectures are more flexible.

Another promising architecture for practical mmWave systems is a fully digital architecture, in which each antenna element is connected to a dedicated RF-chain. To keep the power consumption and cost in check, however, the ADC associated with each RC-chain has a low resolution (possibly as low as only one bit). The channel acquisition in low-resolution mmWave systems is also challenging as only a quantized channel state is observed at the baseband. Therefore channel estimation in low-resolution ADC based mmWave systems also poses large overhead. It will be an interesting direction to explore the out-of-band assisted strategies in low-resolution mmWave systems. Note that some of the proposed strategies for incorporating out-of-band information in mmWave systems are based on compressed sensing framework, which has already been considered for low-resolution ADCs [155]. Therefore, the extension of proposed out-of-band assisted strategies to low-resolution ADCs is only natural.

5.2.3 Extension to multiuser scenario

This dissertation focused primarily on the link level, i.e., between a single mmWave transmitter and receiver. In practical systems, however, there are multiple users present at a given time. Thus, the performance of any link configuration strategy is affected by the multiple users present in the system. Therefore, the proposed sub-6 GHz assisted strategies need to be studied in a multiuser scenario.

For the passive radar assisted strategy, the automotive radar transmissions from multiple vehicles on the road will also impact the performance of covariance estimation, and subsequently its use in mmWave precoding. This deterioration can be controlled (or possibly circumvented) by designing intelligent strategies that take into consideration the presence of multiple users, which is an interesting direction for future work. Note that, at this stage, interference mitigation for automotive radar is an active area of research (see e.g., [156]). The problem of interference mitigation in an active radar, however, is different from the problem of interference mitigation in passive radar. This is because the active radar uses its transmission signal for correlation with the received signals. The passive radar, however, does not know the transmitted waveform.

5.2.4 Extension to other array geometries

This dissertation focused on uniform linear arrays for the sub-6 GHz, mmWave and radar systems. Other array geometries may be deployed in

practice e.g., uniform planar array, circular arrays or co-prime arrays. The uniform planar arrays are preferred because they allow incorporating a large number of antennas in a limited space. This enables large beamforming gains necessary for mmWave communication. Extension of the proposed compressed sensing-based strategies to uniform planar arrays will require that the sparsity in both azimuth and elevation direction be exploited. Note that most of the strategies proposed in this work are based on angular information retrieval and subsequently its use at mmWave. In this regard, circular arrays are interesting as they have spatial invariance properties. Spatial invariance properties imply that the angle estimation accuracy does not depend on the AoA. This is not the case with uniform linear arrays as the angle estimation at broadside is typically more accurate than endfire.

Specific to the radar assisted mmWave strategy presented in Chapter 4, note that the only purpose passive radar array at the base-station serves is the recovery of angular information. Further, as the radar also operates in the mmWave band, it is difficult to construct a fully digital radar with high-resolution ADCs. A simple alternative is to consider co-prime arrays that permit to recover the spatial covariance with a significantly reduced number of antenna elements [139].

5.2.5 Extension to other frameworks

For sub-6 GHz assisted beam-training strategy, we used weighted compressed sensing and structured random codebooks in Chapter 2 to incorporate

the out-of-band information. In Chapter 3, we used weighted compressed covariance estimation, and parametric covariance translation to use sub-6 GHz information. In Chapter 3, for radar assisted strategy we used beam-pruning to reduce the number of beam-pairs that need to be trained.

Other frameworks allow the use of side information. For example, side information can be incorporated in channel/covariance estimation strategies based on approximate message passing (AMP) algorithm [157]. Further, relating the out-of-band information to the communication channel using machine learning strategies is also possible and is an interesting direction for future work. As highlighted in the Chapter 2, the proposed sub-6 GHz assisted strategies may not perform well when the sub-6 GHz link is LOS, whereas the mmWave link is NLOS. The ML-based strategies can also be used to determining the state of the link at sub-6 GHz and mmWave.

Appendix

Proof of Theorems

Proof of Theorem 3.6.1

The received signal (3.28) can be written as

$$\begin{aligned}\mathsf{y} = &\frac{\mathbf{U}^*_{\mathrm{RX,s}}\mathbf{H}\mathbf{U}_{\mathrm{TX,s}}}{\|\hat{\mathbf{U}}_{\mathrm{RX,s}}\|\|\hat{\mathbf{U}}_{\mathrm{TX,s}}\|}\mathsf{s} + \frac{\Delta\mathbf{U}^*_{\mathrm{RX,s}}\mathbf{H}\mathbf{U}_{\mathrm{TX,s}}}{\|\hat{\mathbf{U}}_{\mathrm{RX,s}}\|\|\hat{\mathbf{U}}_{\mathrm{TX,s}}\|}\mathsf{s} \\ &+ \frac{\mathbf{U}^*_{\mathrm{RX,s}}\mathbf{H}\Delta\mathbf{U}_{\mathrm{TX,s}}}{\|\hat{\mathbf{U}}_{\mathrm{RX,s}}\|\|\hat{\mathbf{U}}_{\mathrm{TX,s}}\|}\mathsf{s} + \frac{\Delta\mathbf{U}^*_{\mathrm{RX,s}}\mathbf{H}\Delta\mathbf{U}_{\mathrm{TX,s}}}{\|\hat{\mathbf{U}}_{\mathrm{RX,s}}\|\|\hat{\mathbf{U}}_{\mathrm{TX,s}}\|}\mathsf{s} + \frac{\hat{\mathbf{U}}^*_{\mathrm{RX,s}}}{\|\hat{\mathbf{U}}_{\mathrm{RX,s}}\|}\mathbf{n}. \end{aligned} \tag{1}$$

The numerator of the first term on the RHS is identical to the first term in (3.24) and can be simplified as

$$\frac{\mathbf{U}^*_{\mathrm{RX,s}}\mathbf{H}\mathbf{U}_{\mathrm{TX,s}}}{\|\hat{\mathbf{U}}_{\mathrm{RX,s}}\|\|\hat{\mathbf{U}}_{\mathrm{TX,s}}\|}\mathsf{s} = \frac{\sqrt{N_{\mathrm{RX}}N_{\mathrm{TX}}}\alpha\mathsf{s}}{\|\hat{\mathbf{U}}_{\mathrm{RX,s}}\|\|\hat{\mathbf{U}}_{\mathrm{TX,s}}\|}. \tag{2}$$

Now using the channel representation in form of the signal subspace $\mathbf{H} = \sqrt{N_{\mathrm{RX}}N_{\mathrm{TX}}}\alpha\mathbf{U}_{\mathrm{RX,s}}\mathbf{U}^*_{\mathrm{TX,s}}$, the second term can be written as

$$\frac{\Delta\mathbf{U}^*_{\mathrm{RX,s}}\mathbf{H}\mathbf{U}_{\mathrm{TX,s}}}{\|\hat{\mathbf{U}}_{\mathrm{RX,s}}\|\|\hat{\mathbf{U}}_{\mathrm{TX,s}}\|}\mathsf{s} = \frac{\sqrt{N_{\mathrm{RX}}N_{\mathrm{TX}}}\alpha\Delta\mathbf{U}^*_{\mathrm{RX,s}}\mathbf{U}_{\mathrm{RX,s}}\mathbf{U}^*_{\mathrm{TX,s}}\mathbf{U}_{\mathrm{TX,s}}}{\|\hat{\mathbf{U}}_{\mathrm{RX,s}}\|\|\hat{\mathbf{U}}_{\mathrm{TX,s}}\|}\mathsf{s}. \tag{3}$$

Using the results from [42] we can write $\Delta\mathbf{U}_{\mathrm{RX,s}}$ as

$$\Delta\mathbf{U}_{\mathrm{RX,s}} = \frac{\mathbf{U}_{\mathrm{RX,n}}\mathbf{U}^*_{\mathrm{RX,n}}\Delta\mathbf{R}_{\mathrm{RX}}\mathbf{U}_{\mathrm{RX,s}}}{\sigma^2_\alpha N_{\mathrm{RX}}}, \tag{4}$$

and further

$$\Delta\mathbf{U}^*_{\mathrm{RX,s}}\mathbf{U}_{\mathrm{RX,s}} = \frac{\mathbf{U}^*_{\mathrm{RX,s}}\Delta\mathbf{R}^*_{\mathrm{RX}}\mathbf{U}_{\mathrm{RX,n}}\mathbf{U}^*_{\mathrm{RX,n}}\mathbf{U}_{\mathrm{RX,s}}}{\sigma^2_\alpha N_{\mathrm{RX}}}. \tag{5}$$

In (5), $\mathbf{U}^*_{\mathrm{RX,n}}\mathbf{U}_{\mathrm{RX,s}} = \mathbf{0}$, and hence the second term in (1) is zero. The third term and the fourth term in (1) vanish by the same argument. Hence the received signal can be simply written as

$$\mathsf{y} = \frac{\sqrt{N_{\mathrm{RX}}N_{\mathrm{TX}}}\alpha\mathsf{s}}{\|\hat{\mathbf{U}}_{\mathrm{RX,s}}\|\|\hat{\mathbf{U}}_{\mathrm{TX,s}}\|} + \frac{\hat{\mathbf{U}}^*_{\mathrm{RX,s}}}{\|\hat{\mathbf{U}}_{\mathrm{RX,s}}\|}\mathbf{n}, \tag{6}$$

from which SNR expression (3.29) can be obtained.

Proof of Theorem 3.6.2

We work solely on simplifying $\hat{\mathbf{U}}_{\mathrm{RX,s}}$ on the RHS of (3.30) as the simplification of $\hat{\mathbf{U}}_{\mathrm{TX,s}}$ is analogous. We can write

$$\begin{aligned}
\|\hat{\mathbf{U}}_{\mathrm{RX,s}}\|^2 &\overset{(a)}{=} \|\mathbf{U}_{\mathrm{RX,s}} + \Delta\mathbf{U}_{\mathrm{RX,s}}\|^2 \overset{(b)}{=} \|\mathbf{U}_{\mathrm{RX,s}}\|^2 + \|\Delta\mathbf{U}_{\mathrm{RX,s}}\|^2, \\
&\overset{(c)}{=} 1 + \frac{1}{\sigma_\alpha^4 N_{\mathrm{RX}}^2}\left\|\mathbf{U}_{\mathrm{RX,n}}\mathbf{U}^*_{\mathrm{RX,n}}\Delta\mathbf{R}_{\mathrm{RX}}\mathbf{U}_{\mathrm{RX,s}}\right\|^2, \\
&\overset{(d)}{\approx} 1 + \frac{1}{\sigma_\alpha^4 N_{\mathrm{RX}}^2}\left\|\Delta\mathbf{R}_{\mathrm{RX}}\mathbf{U}_{\mathrm{RX,s}}\right\|^2,
\end{aligned} \tag{7}$$

where (a) comes from the definition of $\hat{\mathbf{U}}_{\mathrm{RX,s}}$ and (b) comes from the assumption that the phase of the perturbation is adjusted to have the true signal subspace and the perturbation signal subspace orthogonal [42]. In (c) the first term simplifies to 1 as the norm of the singular vector and the second term comes from the definition of $\Delta\mathbf{U}_{\mathrm{RX,s}}$ in (4). Finally in (d) we use the approximation $\mathbf{U}_{\mathrm{RX,n}}\mathbf{U}^*_{\mathrm{RX,n}} \approx \mathbf{I}$. Note that for a single path channel, the channel subspace is one dimensional and $\frac{\|\mathbf{U}_{\mathrm{RX,n}}\mathbf{U}^*_{\mathrm{RX,n}} - \mathbf{I}_{N_{\mathrm{RX}}}\|_{\mathrm{F}}^2}{\|\mathbf{I}_{N_{\mathrm{RX}}}\|_{\mathrm{F}}^2} = \frac{1}{N_{\mathrm{RX}}}$. Hence $\frac{\|\mathbf{U}_{\mathrm{RX,n}}\mathbf{U}^*_{\mathrm{RX,n}} - \mathbf{I}_{N_{\mathrm{RX}}}\|_{\mathrm{F}}^2}{\|\mathbf{I}_{N_{\mathrm{RX}}}\|_{\mathrm{F}}^2} \to 0$ as $N_{\mathrm{RX}} \to \infty$ and the approximation is exact in the limit. For mmWave systems where the number of antennas is typically large,

the approximation is fair. Following an analogous derivation for $\hat{\mathbf{U}}_{\mathrm{TX,s}}$, we get (3.31).

To obtain the upper and lower bounds, note the following about the norm of a matrix-vector product $\mathbf{Ax}$: $\max_{\|\mathbf{x}\|_2=1} \|\mathbf{Ax}\|^2 = \sigma^2_{\max}(\mathbf{A})$ and $\min_{\|\mathbf{x}\|_2=1} \|\mathbf{Ax}\|^2 = \sigma^2_{\min}(\mathbf{A})$, where $\sigma_{\max}(\mathbf{A})$ and $\sigma_{\min}(\mathbf{A})$ is the largest and smallest singular value of the matrix $\mathbf{A}$. As in (3.31), $\mathbf{U}_{\mathrm{RX,s}}$ is a singular vector with unit norm, we can bound $\sigma_{\min}(\Delta\mathbf{R}_{\mathrm{RX}}) \leq \|\Delta\mathbf{R}_{\mathrm{RX}}\mathbf{U}_{\mathrm{RX,s}}\| \leq \sigma_{\max}(\Delta\mathbf{R}_{\mathrm{RX}})$. Using this result in (3.31), we get (3.32) and (3.33).

Publications

Publications related to the dissertation

1. Anum Ali, Nuria González-Prelcic and Robert W. Heath Jr., "Millimeter Wave Beam-Selection Using Out-of-Band Spatial Information", IEEE Transactions on Wireless Communications, vol. 17, no. 2, pp. 1038-1052, 2018.

2. Nuria González-Prelcic, Anum Ali, Vutha Va and Robert W. Heath Jr., "Millimeter Wave communication with out-of-band information", IEEE Communications Magazine, vol. 55, no. 12, pp. 140-146, 2017.

3. Anum Ali, Nuria González-Prelcic and Robert W. Heath Jr., "Spatial Covariance Estimation for Millimeter Wave Hybrid Systems using Out-of-Band Information", accepted to appear in IEEE Transactions on Wireless Communications.

4. Anum Ali, and Robert W. Heath Jr., "Compressed Beam-selection in Millimeter Wave Systems with Out-of-Band Partial Support Information", in Proceedings of International Conference on Acoustics, Speech and Signal Processing (ICASSP), 2017.

5. Anum Ali, Nuria González-Prelcic and Robert W. Heath Jr., "Estimating Millimeter Wave Channels using Out-of-Band Measurements", in

Proceedings of Information Theory and Applications (ITA) Workshop, 2016.

6. Anum Ali, Nuria González-Prelcic, and Amitava Ghosh, "Millimeter wave V2I beam-training using base-station mounted radar", to appear in Proceedings of IEEE Radar Conference, 2019.

7. Anum Ali, Nuria González-Prelcic, and Robert W. Heath Jr.,, "Automotive radar as signals of opportunity for millimeter wave V2I links", to appear in Proceedings of Asilomar Conference on Signals, Systems, and Computers (ASILOMAR), 2019.

Other publications

1. Anum Ali, Elisabeth De Carvalho, and Robert W. Heath Jr., "Linear Receivers in Non-stationary Massive MIMO Channels with Visibility Regions", IEEE Wireless Communication Letters, vol. 8, no. 3, pp. 885-888, 2019.

2. Elisabeth de Carvalho, Anum Ali, Abolfazl Amiri, Marko Angjelichinoski, and Robert W. Heath Jr., "Non-Stationarities in Extra-Large Scale Massive MIMO", submitted to IEEE Wireless Communications.

3. Sungwoo Park, Anum Ali, Nuria González-Prelcic, and Robert W. Heath Jr., "Spatial Channel Covariance Estimation for Hybrid Architectures Based on Tensor Decompositions", submitted to IEEE Transactions on Wireless Communications.

4. Anum Ali, Libin Jiang, Shailesh Patil, Junyi Li, Robert W. Heath Jr., "Vehicle-to-vehicle communication for autonomous vehicles: Safety and Maneuver Planning", in Proceedings of Proceedings of Vehicular Technology Conference.

5. Sungwoo Park, Anum Ali, Nuria González-Prelcic and Robert W. Heath Jr., Spatial channel covariance estimation for the hybrid MIMO architecture at a base station: a tensor-decomposition-based approach," in Proceedings of IEEE Global Conference on Signal and Information Processing.

Bibliography

[1] Z. Pi and F. Khan, "An introduction to millimeter-wave mobile broadband systems," *IEEE Commun. Mag.*, vol. 49, no. 6, pp. 101–107, Jun. 2011.

[2] T. S. Rappaport, S. Sun, R. Mayzus, H. Zhao, Y. Azar, K. Wang, G. N. Wong, J. K. Schulz, M. Samimi, and F. Gutierrez, "Millimeter wave mobile communications for 5G cellular: It will work!" *IEEE Access*, vol. 1, pp. 335–349, May 2013.

[3] S. Rangan, T. S. Rappaport, and E. Erkip, "Millimeter-wave cellular wireless networks: Potentials and challenges," *Proc. IEEE*, vol. 102, no. 3, pp. 366–385, Mar. 2014.

[4] T. Bai and R. W. Heath Jr., "Coverage and rate analysis for millimeter-wave cellular networks," *IEEE Trans. Wireless Commun.*, vol. 14, no. 2, pp. 1100–1114, Feb. 2015.

[5] T. S. Rappaport, R. W. Heath Jr., R. C. Daniels, and J. N. Murdock, *Millimeter wave wireless communications*. Prentice Hall, 2014.

[6] "IEEE standard for information technology–Telecommunications and information exchange between systems–Local and metropolitan area networks–Specific requirements-Part 11: Wireless LAN medium access

control (MAC) and physical layer (PHY) specifications amendment 3: Enhancements for very high throughput in the 60 GHz band," pp. 1–628, Dec. 2012.

[7] K. Venugopal and R. W. Heath Jr., "Millimeter wave networked wearables in dense indoor environments," *IEEE Access*, vol. 4, pp. 1205–1221, 2016.

[8] R. C. Daniels and R. W. Heath Jr., "60 GHz wireless communications: Emerging requirements and design recommendations," *IEEE Veh. Technol. Mag.*, vol. 2, no. 3, pp. 41–50, 2007.

[9] A. K. Gupta, J. G. Andrews, and R. W. Heath Jr., "On the feasibility of sharing spectrum licenses in mmWave cellular systems," vol. 64, no. 9, pp. 3981–3995, 2016.

[10] J. Choi, V. Va, N. González-Prelcic, R. Daniels, C. R. Bhat, and R. W. Heath Jr., "Millimeter wave vehicular communication to support massive automotive sensing," *IEEE Commun. Mag.*, vol. 54, no. 12, pp. 160–167, Dec. 2016.

[11] A. Ali, L. Jiang, S. Patil, J. Li, and R. W. Heath Jr., "Vehicle-to-Vehicle Communication for Autonomous Vehicles: Safety and Maneuver Planning," in *Proc. IEEE Veh. Tech. Conf. (VTC)*, 2018, pp. 1–5.

[12] *J2735 Dedicated Short Range Communications (DSRC) Message Set Dictionary*, Society of Automotive Engineers (SAE) Std., 2009.

[13] Y. J. Li, "An overview of the DSRC/WAVE technology," in *Proc. Qual., Rel., Security Robustness Heterogeneous Netw.* Springer Berlin Heidelberg, Nov. 2010, pp. 544–558.

[14] J. B. Kenney, "Dedicated short-range communications (DSRC) standards in the United States," *Proc. IEEE*, vol. 99, no. 7, pp. 1162–1182, 2011.

[15] 3GPP, "Evolved Universal Terrestrial Radio Access (E-UTRA) and Evolved Universal Terrestrial Radio Access Network (E-UTRAN); Overall description; Stage 2," 3rd Generation Partnership Project (3GPP), TS 36.300, Sep. 2018, version 15.3.0. [Online]. Available: http://www.3gpp.org/DynaReport/36300.htm

[16] M. Rumney *et al.*, *LTE and the evolution to 4G wireless: Design and measurement challenges.* John Wiley & Sons, 2013.

[17] R. W. Heath Jr., N. González-Prelcic, S. Rangan, W. Roh, and A. Sayeed, "An overview of signal processing techniques for millimeter Wave MIMO Systems," *IEEE J. Sel. Topics Signal Process.*, vol. 10, no. 3, pp. 436–453, Apr. 2016.

[18] O. El Ayach, S. Rajagopal, S. Abu-Surra, Z. Pi, and R. W. Heath Jr., "Spatially sparse precoding in millimeter wave MIMO systems," *IEEE Trans. Wireless Commun.*, vol. 13, no. 3, pp. 1499–1513, Mar. 2014.

[19] A. Alkhateeb, O. El Ayach, G. Leus, and R. W. Heath Jr., "Hybrid precoding for millimeter wave cellular systems with partial channel knowledge," in *Proc. Inf. Theory Appl. (ITA) Wksp*, Feb. 2013, pp. 1–5.

[20] ——, "Channel estimation and hybrid precoding for millimeter wave cellular systems," *IEEE J. Sel. Topics Signal Process.*, vol. 8, no. 5, pp. 831–846, Oct. 2014.

[21] J. Choi, "Beam selection in mm-Wave multiuser MIMO systems using compressive sensing," *IEEE Trans. Commun.*, vol. 63, no. 8, pp. 2936–2947, Aug. 2015.

[22] J. Seo, Y. Sung, G. Lee, and D. Kim, "Training beam sequence design for millimeter-wave MIMO systems: A POMDP framework," *IEEE Trans. Signal Process.*, vol. 64, no. 5, pp. 1228–1242, Mar. 2016.

[23] J. Wang, "Beam codebook based beamforming protocol for multi-Gbps millimeter-wave WPAN systems," *IEEE J. Sel. Areas Commun.*, vol. 27, no. 8, pp. 1390–1399, Oct. 2009.

[24] S. Hur, T. Kim, D. J. Love, J. V. Krogmeier, T. A. Thomas, and A. Ghosh, "Millimeter wave beamforming for wireless backhaul and access in small cell networks," *IEEE Trans. Commun.*, vol. 61, no. 10, pp. 4391–4403, Oct. 2013.

[25] P. Schniter and A. Sayeed, "Channel estimation and precoder design for millimeter-wave communications: The sparse way," in *Proc. Asilomar*

Conf. Signals, Syst. Comput. (ASILOMAR), Nov. 2014, pp. 273–277.

[26] J. Lee, G.-T. Gil, and Y. H. Lee, "Exploiting spatial sparsity for estimating channels of hybrid MIMO systems in millimeter wave communications," in *Proc. IEEE Glob. Telecom. Conf. (GLOBECOM)*, Dec. 2014, pp. 3326–3331.

[27] D. E. Berraki, S. M. Armour, and A. R. Nix, "Application of compressive sensing in sparse spatial channel recovery for beamforming in mmWave outdoor systems," in *Proc. IEEE Wireless Commun. Netw. Conf. (WCNC)*, Apr. 2014, pp. 887–892.

[28] Z. Zhou, J. Fang, L. Yang, H. Li, Z. Chen, and R. S. Blum, "Low-rank tensor decomposition-aided channel estimation for millimeter wave MIMO-OFDM systems," vol. 35, no. 7, pp. 1524–1538, 2017.

[29] Y. Kishiyama, A. Benjebbour, T. Nakamura, and H. Ishii, "Future steps of LTE-A: Evolution toward integration of local area and wide area systems," *IEEE Wireless Commun.*, vol. 20, no. 1, pp. 12–18, Feb. 2013.

[30] R. C. Daniels and R. W. Heath Jr., "Multi-band modulation, coding, and medium access control," IEEE 802.11-07/2780R1, pp. 1–18, Nov. 2007.

[31] M. Hashemi, C. E. Koksal, and N. B. Shroff, "Out-of-band millimeter wave beamforming and communications to achieve low latency and high

energy efficiency in 5G systems," *IEEE Trans. Commun.*, vol. 66, no. 2, pp. 875–888, 2018.

[32] N. Garcia, H. Wymeersch, E. G. Ström, and D. Slock, "Location-aided mm-wave channel estimation for vehicular communication," in *Proc. IEEE Int. Workshop Signal Process. Adv. Wireless Commun. (SPAWC)*, Jul. 2016, pp. 1–5.

[33] V. Va, T. Shimizu, G. Bansal, and R. W. Heath Jr., "Position-aided millimeter wave V2I beam alignment: A learning-to-rank approach," in *Proc. IEEE Int. Symp. Pers., Indoor Mobile Radio Commun. (PIMRC)*, Oct. 2017, pp. 1–5.

[34] N. González-Prelcic, R. Méndez-Rial, and R. W. Heath Jr., "Radar aided beam alignment in mmwave V2I communications supporting antenna diversity," in *Proc. Inf. Theory Appl. (ITA) Wksp*, Feb. 2016, pp. 1–5.

[35] J. Lu, D. Steinbach, P. Cabrol, and P. Pietraski, "Modeling human blockers in millimeter wave radio links," *ZTE Commun.*, vol. 10, no. 4, pp. 23–28, Dec. 2012.

[36] L. Simić, J. Arnold, M. Petrova, and P. Mähänen, "RadMAC: radar-enabled link obstruction avoidance for agile mm-wave beamsteering," in *Proc. 3rd Wksp Hot Topics Wireless*, 2016, pp. 61–65.

[37] J. Kim, J. Chun, and S. Song, "Joint Range and Angle Estimation for FMCW MIMO Radar and Its Application," *arXiv preprint*

arXiv:1811.06715, 2018.

[38] J. Scarlett, J. S. Evans, and S. Dey, "Compressed sensing with prior information: Information-theoretic limits and practical decoders," *IEEE Trans. Signal Process.*, vol. 61, no. 2, pp. 427–439, Jan 2013.

[39] J. A. Tropp, A. C. Gilbert, and M. J. Strauss, "Simultaneous sparse approximation via greedy pursuit," in *Proc. IEEE Int. Conf. Acoust., Speech Signal Process. (ICASSP)*, vol. 5, Mar. 2005, pp. 721–724.

[40] A. Ali and R. W. Heath Jr., "Compressed beam-selection in millimeter wave systems with out-of-band partial support information," in *Proc. IEEE Int. Conf. Acoust., Speech Signal Process. (ICASSP)*, Mar. 2017, pp. 3499–3503.

[41] A. Ali, N. González-Prelcic, and R. W. Heath Jr., "Millimeter wave beam-selection using out-of-band spatial information," *IEEE Trans. Wireless Commun.*, vol. 17, no. 2, pp. 1038–1052, 2018.

[42] J. Liu, X. Liu, and X. Ma, "First-order perturbation analysis of singular vectors in singular value decomposition," *IEEE Trans. Signal Process.*, vol. 56, no. 7, pp. 3044–3049, 2008.

[43] M. D. Larsen and A. L. Swindlehurst, "A MIMO channel perturbation analysis for robust bit loading," in *Proc. IEEE Int. Conf. Acoust., Speech Signal Process. (ICASSP)*, Apr. 2009, pp. 2825–2828.

[44] J. Zhang, M. Haardt, and F. Roemer, "Robust design of block diagonalization using perturbation analysis," in *Proc. IEEE Int. Conf. Acoust., Speech Signal Process. (ICASSP)*, May 2013, pp. 4192–4196.

[45] A. Ali, N. González-Prelcic, and R. W. Heath Jr., "Estimating millimeter wave channels using out-of-band measurements," in *Proc. Inf. Theory Appl. (ITA) Wksp*, Feb. 2016, pp. 1–6.

[46] A. Ali, N. González-Prelcic, and R. W. Heath Jr, "Spatial Covariance Estimation for Millimeter Wave Hybrid Systems using Out-of-Band Information," *IEEE Trans. Wireless Commun.*, 2019, (early access).

[47] M. Jordan, X. Gong, and G. Ascheid, "Conversion of the spatio-temporal correlation from uplink to downlink in FDD systems," in *Proc. IEEE Wireless Commun. Netw. Conf. (WCNC)*, Apr. 2009, pp. 1–6.

[48] S. Park, A. Ali, N. González-Prelcic, and R. W. Heath Jr, "Spatial Channel Covariance Estimation for Hybrid Architectures Based on Tensor Decompositions," *arXiv preprint arXiv:1902.06297*, 2019.

[49] S. Haghighatshoar and G. Caire, "Massive MIMO channel subspace estimation from low-dimensional projections," *IEEE Trans. Signal Process.*, vol. 65, no. 2, pp. 303–318, 2017.

[50] S. Park and R. W. Heath Jr, "Spatial Channel Covariance Estimation for the Hybrid MIMO Architecture: A Compressive Sensing Based Ap-

proach," *IEEE Trans. Wireless Commun.*, vol. 17, no. 12, pp. 8047–8062, 2018.

[51] A. Ali, N. González-Prelcic, and A. Ghosh, "Millimeter wave V2I beam-training using base-station mounted radar," in *Proc. IEEE Radar Conf.*, 2019, to appear.

[52] J. G. Andrews, S. Buzzi, W. Choi, S. V. Hanly, A. Lozano, A. C. Soong, and J. C. Zhang, "What will 5G be?" *IEEE J. Sel. Areas Commun.*, vol. 32, no. 6, pp. 1065–1082, Jun. 2014.

[53] Z. Pi, J. Choi, and R. Heath, "Millimeter-wave gigabit broadband evolution toward 5G: fixed access and backhaul," *IEEE Commun. Mag.*, vol. 54, no. 4, pp. 138–144, Apr. 2016.

[54] V. Va, J. Choi, and R. W. Heath Jr, "The impact of beamwidth on temporal channel variation in vehicular channels and its implications," *IEEE Trans. Veh. Technol.*, vol. 66, no. 6, pp. 5014–5029, Jun. 2017.

[55] A. D. Angelica. (2013) Googles self-driving car gathers nearly 1gb/sec. [Online]. Available: http://www.kurzweilai.net/googles-self-driving-car-gathers-nearly-1-gbsec

[56] M. Peter, K. Sakaguchi, S. Jaeckel, S. Wu, M. Nekovee, J. Medbo, K. Haneda, S. L. H. Nguyen, R. Naderpour, J. Vehmas *et al.*, "Measurement campaigns and initial channel models for preferred

suitable frequency ranges," Mar. 2016. [Online]. Available: https://bscw.5g-mmmagic.eu/pub/bscw.cgi/d94832/mmMAGIC_D2-1.pdf

[57] T. Asté, P. Forster, L. Féty, and S. Mayrargue, "Downlink beamforming avoiding DOA estimation for cellular mobile communications," in *Proc. IEEE Int. Conf. Acoust., Speech Signal Process. (ICASSP)*, May 1998, pp. 3313–3316.

[58] K. Hugl, K. Kalliola, and J. Laurila, "Spatial reciprocity of uplink and downlink radio channels in FDD systems," EUROPEAN COOPERATION IN THE FIELD OF SCIENTIFIC AND TECHNICAL RESEARCH (EURO-COST), Espoo, Finland, Tech. Rep., May 2002, COST 273 Technical Document TD(02) 066.

[59] A. Decurninge, M. Guillaud, and D. T. Slock, "Channel covariance estimation in massive MIMO frequency division duplex systems," in *Proc. IEEE Glob. Telecom. Conf. (GLOBECOM)*, Dec. 2015, pp. 1–6.

[60] B. K. Chalise, L. Häring, and A. Czylwik, "Uplink to downlink spatial covariance matrix transformation methods for downlink beamforming of a UMTS-FDD system," in *Proc. IEEE Veh. Tech. Conf. (VTC)*, vol. 1, May 2004, pp. 132–136.

[61] D. Vasisht, S. Kumar, H. Rahul, and D. Katabi, "Eliminating channel feedback in next-generation cellular networks," in *Proc. ACM SIGCOMM*, Aug. 2016, pp. 398–411.

[62] J. Shen, J. Zhang, E. Alsusa, and K. Letaief, "Compressed CSI acquisition in FDD massive MIMO: How much training is needed?" *IEEE Trans. Wireless Commun.*, vol. 15, no. 6, pp. 4145–4156, Jun. 2016.

[63] T. Nitsche, A. B. Flores, E. W. Knightly, and J. Widmer, "Steering with eyes closed: mm-wave beam steering without in-band measurement," in *Proc. IEEE Int. Conf. Comput. Commun. (INFOCOM)*, Apr. 2015, pp. 2416–2424.

[64] V. Raghavan, S. Subramanian, A. Sampath, and J. Li, "Low-frequency assisted methods for beamforming, timing and frequency offset in mm-wave access systems," May 2016, US Patent 9,337,969. [Online]. Available: https://www.google.com/patents/US9337969

[65] A. Alkhateeb and R. W. Heath Jr., "Frequency selective hybrid precoding for limited feedback millimeter wave systems," *IEEE Trans. Commun.*, vol. 64, no. 5, pp. 1801–1818, May 2016.

[66] F. Maschietti, D. Gesbert, P. de Kerret, and H. Wymeersch, "Robust location-aided beam alignment in millimeter wave massive MIMO," *arXiv preprint arXiv:1705.01002*, 2017.

[67] V. Raghavan, J. Cezanne, S. Subramanian, A. Sampath, and O. Koymen, "Beamforming tradeoffs for initial UE discovery in millimeter-wave MIMO systems," *IEEE J. Sel. Topics Signal Process.*, vol. 10, no. 3, pp. 543–559, Apr. 2016.

[68] K. Venugopal, A. Alkhateeb, N. G. Prelcic, and R. W. Heath, "Channel estimation for hybrid architecture based wideband millimeter wave systems," *IEEE J. Sel. Areas Commun.*, vol. 35, no. 9, pp. 1996–2009, Sep. 2017.

[69] A. Alkhateeb, G. Leus, and R. W. Heath Jr., "Compressed sensing based multi-user millimeter wave systems: How many measurements are needed?" in *Proc. IEEE Int. Conf. Acoust., Speech Signal Process. (ICASSP)*, Apr. 2015, pp. 2909–2913.

[70] J. A. Tropp and A. C. Gilbert, "Signal recovery from random measurements via orthogonal matching pursuit," *IEEE Trans. Inf. Theory*, vol. 53, no. 12, pp. 4655–4666, Dec 2007.

[71] Z. Gao, L. Dai, Z. Wang, and S. Chen, "Spatially common sparsity based adaptive channel estimation and feedback for FDD massive MIMO," *IEEE Trans. Signal Process.*, vol. 63, no. 23, pp. 6169–6183, Dec. 2015.

[72] M. L. Bencheikh, Y. Wang, and H. He, "Polynomial root finding technique for joint DOA DOD estimation in bistatic MIMO radar," *Signal Process.*, vol. 90, no. 9, pp. 2723–2730, Sep. 2010.

[73] M. Bengtsson and B. Ottersten, "Low-complexity estimators for distributed sources," *IEEE Trans. Signal Process.*, vol. 48, no. 8, pp. 2185–2194, Aug. 2000.

[74] H. Minn and N. Al-Dhahir, "Optimal training signals for MIMO OFDM channel estimation," *IEEE Trans. Wireless Commun.*, vol. 5, no. 5, pp. 1158–1168, May 2006.

[75] E. J. Candes, M. B. Wakin, and S. P. Boyd, "Enhancing sparsity by reweighted ℓ_1 minimization," *J. Fourier Anal. Appl*, vol. 14, no. 5-6, pp. 877–905, Dec. 2008.

[76] C. Herzet, C. Soussen, J. Idier, and R. Gribonval, "Exact recovery conditions for sparse representations with partial support information," *IEEE Trans. Inf. Theory*, vol. 59, no. 11, pp. 7509–7524, Nov. 2013.

[77] M. P. Friedlander, H. Mansour, R. Saab, and Ö. Yilmaz, "Recovering compressively sampled signals using partial support information," *IEEE Trans. Inf. Theory*, vol. 58, no. 2, pp. 1122–1134, Feb. 2012.

[78] S. Oymak, M. A. Khajehnejad, and B. Hassibi, "Weighted compressed sensing and rank minimization," in *Proc. IEEE Int. Conf. Acoust., Speech Signal Process. (ICASSP)*, May 2011, pp. 3736–3739.

[79] M. A. Khajehnejad, W. Xu, A. S. Avestimehr, and B. Hassibi, "Weighted ℓ_1 minimization for sparse recovery with prior information," in *Proc. IEEE Int. Symp. Inf. Theory (ISIT)*, Jun. 2009, pp. 483–487.

[80] N. Vaswani and W. Lu, "Modified-CS: Modifying compressive sensing for problems with partially known support," *IEEE Trans. Signal Process.*, vol. 58, no. 9, pp. 4595–4607, Sep. 2010.

[81] D. Needell, R. Saab, and T. Woolf, "Weighted ℓ_1-minimization for sparse recovery under arbitrary prior information," *arXiv preprint arXiv:1606.01295*, 2016.

[82] E. J. Candes, Y. C. Eldar, D. Needell, and P. Randall, "Compressed sensing with coherent and redundant dictionaries," *Appl. Computat. Harmonic Anal.*, vol. 31, no. 1, pp. 59–73, 2011.

[83] Z. Li, W. Xu, Y. Tian, Y. Wang, and J. Lin, "Compressed sensing reconstruction algorithms with prior information: logit weight simultaneous orthogonal matching pursuit," in *Proc. IEEE Veh. Tech. Conf. (VTC)*, May 2014, pp. 1–5.

[84] I. T. U. (ITU), "Propagation data and prediction methods for the planning of indoor radiocommunication systems and radio local area networks in the frequency range 900 MHz to 100 GHz," Tech. Rep. ITU-R P.1238-6, Oct. 2009.

[85] E. J. Violette, R. H. Espeland, R. O. DeBolt, and F. Schwering, "Millimeter-wave propagation at street level in an urban environment," *IEEE Trans. Geosci. Remote Sens.*, vol. 26, no. 3, pp. 368–380, May 1988.

[86] R. J. Weiler, M. Peter, T. Kühne, M. Wisotzki, and W. Keusgen, "Simultaneous millimeter-wave multi-band channel sounding in an urban access scenario," in *Proc. Eur. Conf. Antennas Propag. (EuCAP)*, Apr. 2015, pp. 1–5.

[87] A. S. Poon and M. Ho, "Indoor multiple-antenna channel characterization from 2 to 8 GHz," in *Proc. IEEE Int. Conf. Commun. (ICC)*, May 2003, pp. 3519–3523.

[88] S. Jaeckel, M. Peter, K. Sakaguchi, W. Keusgen, and J. Medbo, "5G channel models in mm-wave frequency bands," in *Proc. Eur. Wireless Conf. (EW)*, May 2016, pp. 1–6.

[89] A. Ö. Kaya, D. Calin, and H. Viswanathan. (2016, Apr.) 28 GHz and 3.5 GHz wireless channels: Fading, delay and angular dispersion.

[90] O. H. Koymen, A. Partyka, S. Subramanian, and J. Li, "Indoor mm-Wave channel measurements: Comparative study of 2.9 GHz and 29 GHz," in *Proc. IEEE Glob. Telecom. Conf. (GLOBECOM)*, Dec. 2015, pp. 1–6.

[91] M. K. Samimi and T. S. Rappaport, "3-D millimeter-wave statistical channel model for 5G wireless system design," *IEEE Trans. Microw. Theory Techn.*, vol. 64, no. 7, pp. 2207–2225, Jul. 2016.

[92] R. C. Qiu and I.-T. Lu, "Multipath resolving with frequency dependence for wide-band wireless channel modeling," *IEEE Trans. Veh. Technol.*, vol. 48, no. 1, pp. 273–285, Jan. 1999.

[93] K. Haneda, A. Richter, and A. F. Molisch, "Modeling the frequency dependence of ultra-wideband spatio-temporal indoor radio channels,"

IEEE Trans. Antennas Propag., vol. 60, no. 6, pp. 2940–2950, Jun. 2012.

[94] D. Dupleich, R. S. Thom, G. Steinb, J. Luo, E. Schulz, X. Lu, G. Wang *et al.*, "Simultaneous multi-band channel sounding at mm-Wave frequencies," in *Proc. Eur. Conf. Antennas Propag. (EuCAP)*, Apr. 2016, pp. 1–5.

[95] P. Kyösti, I. C. Llorente, A. Karstensen, W. Fan, and G. F. Pedersen, "Frequency dependency of channel parameters in urban LOS scenario for mmwave communications," in *Proc. Eur. Conf. Antennas Propag. (EuCAP)*, Apr. 2016, pp. 1–5.

[96] V. Va, J. Choi, T. Shimizu, G. Bansal, and R. W. Heath Jr, "Inverse multipath fingerprinting for millimeter wave V2I beam alignment," *arXiv preprint arXiv:1705.05942*, 2017.

[97] K. Haneda, J.-i. Takada, and T. Kobayashi, "Experimental investigation of frequency dependence in spatio-temporal propagation behaviour," in *Proc. Eur. Conf. Antennas Propag. (EuCAP)*, Nov. 2007, pp. 1–6.

[98] V. Nurmela, A. Karttunen, A. Roivainen, L. Raschkowski, T. Imai, J. Jarvelainen, J. Medbo, Jonas andVihriala, J. Meinila, K. Haneda *et al.*, "METIS channel models," Feb. 2015. [Online]. Available: https://www.metis2020.com/wp-content/uploads/METIS_D1.4_v3.pdf

[99] F. C. Commission, "FCC makes 150 megahertz of contiguous spectrum available for mobile broadband and other uses through innovative sharing policies." [Online]. Available: https://apps.fcc.gov/edocs_public/attachmatch/DOC-333083A1.pdf

[100] ——, "LMDS (Local Multipoint Distribution Service) Band Allocation: 28 & 31 GHz Band Plan." [Online]. Available: http://wireless.fcc.gov/auctions/data/bandplans/lmds.pdf

[101] ——, "Amendment of the commissions rules with regard to commercial operations in the 3550-3650 MHz band," *GN Docket*, no. 12-354, 2012.

[102] F. C. Commission *et al.*, "Fact sheet: spectrum frontiers rules identify, open up vast amounts of new high-band spectrum for next generation (5G) wireless broadband," 2016. [Online]. Available: https://apps.fcc.gov/edocs_public/attachmatch/DOC-340310A1.pdf

[103] B. Hassibi and B. M. Hochwald, "How much training is needed in multiple-antenna wireless links?" *IEEE Trans. Inf. Theory*, vol. 49, no. 4, pp. 951–963, 2003.

[104] M. Giordani, M. Polese, A. Roy, D. Castor, and M. Zorzi, "A Tutorial on Beam Management for 3GPP NR at mmWave Frequencies," *IEEE Commun. Surveys Tuts.*, vol. 21, no. 1, pp. 173–196, 2018.

[105] J. Mo and R. W. Heath Jr., "Capacity analysis of one-bit quantized MIMO systems with transmitter channel state information," *IEEE*

Trans. Signal Process., vol. 63, no. 20, pp. 5498–5512, 2015.

[106] B. K. Chalise, L. Haering, and A. Czylwik, "Robust uplink to downlink spatial covariance matrix transformation for downlink beamforming," in *Proc. IEEE Int. Conf. Commun. (ICC)*, vol. 5, Jun. 2004, pp. 3010–3014.

[107] K. Hugl, J. Laurila, and E. Bonek, "Downlink beamforming for frequency division duplex systems," in *Proc. IEEE Glob. Telecom. Conf. (GLOBECOM)*, vol. 4, Dec. 1999, pp. 2097–2101.

[108] L. Miretti, R. L. Cavalcante, and S. Stanczak, "FDD massive MIMO channel spatial covariance conversion using projection methods," *arXiv preprint arXiv:1804.04850*, 2018.

[109] R. Méndez-Rial, N. González-Prelcic, and R. W. Heath Jr., "Adaptive hybrid precoding and combining in mmWave multiuser MIMO systems based on compressed covariance estimation," in *Proc. IEEE Int. Workshop Comput. Adv. Multi-Sensor Adapt. Process. (CAMSAP)*, Dec. 2015, pp. 213–216.

[110] S. Park and R. W. Heath Jr., "Spatial channel covariance estimation for mmWave hybrid MIMO architecture," in *Proc. Asilomar Conf. Signals, Syst. Comput. (ASILOMAR)*, Nov. 2016, pp. 1424–1428.

[111] H. Ji, Y. Kim, J. Lee, E. Onggosanusi, Y. Nam, J. Zhang, B. Lee, and B. Shim, "Overview of full-dimension MIMO in LTE-advanced pro,"

IEEE Commun. Mag., vol. 55, no. 2, pp. 176–184, 2017.

[112] E. Bjornson, D. Hammarwall, and B. Ottersten, "Exploiting quantized channel norm feedback through conditional statistics in arbitrarily correlated MIMO systems," *IEEE Trans. Signal Process.*, vol. 57, no. 10, pp. 4027–4041, 2009.

[113] N. Czink, G. Matz, D. Seethaler, and F. Hlawatsch, "Improved MMSE estimation of correlated MIMO channels using a structured correlation estimator," in *Proc. IEEE Int. Workshop Signal Process. Adv. Wireless Commun. (SPAWC)*, Jun. 2005, pp. 595–599.

[114] A. Forenza, D. J. Love, and R. W. Heath Jr., "Simplified spatial correlation models for clustered MIMO channels with different array configurations," *IEEE Trans. Veh. Technol.*, vol. 56, no. 4, pp. 1924–1934, Jul. 2007.

[115] M. Wax and T. Kailath, "Detection of signals by information theoretic criteria," *IEEE Trans. Acoust., Speech, Signal Process.*, vol. 33, no. 2, pp. 387–392, Apr. 1985.

[116] H. Akaike, "A new look at the statistical model identification," *IEEE Trans. Autom. Control*, vol. 19, no. 6, pp. 716–723, Dec. 1974.

[117] R. O. Schmidt, "Multiple emitter location and signal parameter estimation," *IEEE Trans. Antennas Propag.*, vol. 34, no. 3, pp. 276–280, Mar. 1986.

[118] D. D. Arianandа and G. Leus, "Direction of arrival estimation for more correlated sources than active sensors," *Signal Process.*, vol. 93, no. 12, pp. 3435–3448, Dec. 2013.

[119] B. Ottersten, P. Stoica, and R. Roy, "Covariance matching estimation techniques for array signal processing applications," *Digital Signal Process.*, vol. 8, no. 3, pp. 185–210, Jul. 1998.

[120] T. Trump and B. Ottersten, "Estimation of nominal direction of arrival and angular spread using an array of sensors," *Signal Process.*, vol. 50, no. 1, pp. 57–69, Apr. 1996.

[121] M. D. Zoltowski, G. M. Kautz, and S. D. Silverstein, "Beamspace Root-MUSIC," *IEEE Trans. Signal Process.*, vol. 41, no. 1, pp. 344–364, Jan. 1993.

[122] A. J. Barabell, "Improving the resolution performance of eigenstructure-based direction-finding algorithms," in *Proc. IEEE Int. Conf. Acoust., Speech Signal Process. (ICASSP)*, vol. 8, Apr. 1983, pp. 336–339.

[123] D. Romero, D. D. Arianandа, Z. Tian, and G. Leus, "Compressive covariance sensing: Structure-based compressive sensing beyond sparsity," *IEEE Signal Process. Mag.*, vol. 33, no. 1, pp. 78–93, 2016.

[124] J. M. Bioucas-Dias, D. Cohen, and Y. C. Eldar, "Covalsa: Covariance estimation from compressive measurements using alternating minimiza-

tion," in *Proc. Eur. Signal Process. Conf. (EUSIPCO)*, Sep. 2014, pp. 999–1003.

[125] J. Rodriguez-Fernandez, R. Lopez-Valcarce, and N. González-Prelcic, "Hybrid precoding and combining for frequency-selective mmWave MIMO Systems with per-antenna power constraints," *arXiv preprint arXiv:1812.02760*, 2018.

[126] A. M. Sayeed, "Deconstructing multiantenna fading channels," *IEEE Trans. Signal Process.*, vol. 50, no. 10, pp. 2563–2579, Oct. 2002.

[127] K. Venugopal, N. González-Prelcic, and R. W. Heath Jr., "Optimality of frequency flat precoding in frequency selective millimeter wave channels," *IEEE Wireless Commun. Lett.*, vol. 6, no. 3, pp. 330–333, 2017.

[128] R. Vershynin, "Introduction to the non-asymptotic analysis of random matrices," *arXiv preprint arXiv:1011.3027*, 2010.

[129] Y. Li, C. Tao, G. Seco-Granados, A. Mezghani, A. L. Swindlehurst, and L. Liu, "Channel estimation and performance analysis of one-bit massive MIMO systems," *IEEE Trans. Signal Process.*, vol. 65, no. 15, pp. 4075–4089, 2017.

[130] A. F. Molisch, V. V. Ratnam, S. Han, Z. Li, S. L. H. Nguyen, L. Li, and K. Haneda, "Hybrid beamforming for massive MIMO: A survey," *IEEE Commun. Mag.*, vol. 55, no. 9, pp. 134–141, 2017.

[131] A. Klautau, N. González-Prelcic, and R. W. Heath, "LIDAR Data for Deep Learning-Based mmWave Beam-Selection," *IEEE Wireless Commun. Lett.*, vol. 8, no. 3, pp. 909–912, 2019.

[132] M. Brambilla, M. Nicoli, S. Savaresi, and U. Spagnolini, "Inertial Sensor Aided mmWave Beam Tracking to Support Cooperative Autonomous Driving," *arXiv preprint arXiv:1903.11849*, 2019.

[133] Z. Chen, Z. Cao, X. He, Y. Jin, J. Li, and P. Chen, "DoA and DoD Estimation and Hybrid Beamforming for Radar-Aided mmWave MIMO Vehicular Communication Systems," *Electron.*, vol. 7, no. 3, p. 40, 2018.

[134] G. R. Muns, K. V. Mishra, C. B. Guerra, Y. C. Eldar, and K. R. Chowdhury, "Beam alignment and tracking for autonomous vehicular communication using IEEE 802.11 ad-based radar," *arXiv preprint arXiv:1712.02453*, 2017.

[135] C. Jiao, Z. Zhang, C. Zhong, X. Chen, and Z. Feng, "Millimeter Wave Communication With Active Ambient Perception," *IEEE Trans. Wireless Commun.*, vol. 18, no. 5, pp. 2751–2764, 2019.

[136] 3GPP, "Study on evaluation methodology of new Vehicle-to-Everything V2X use cases for LTE and NR," 3rd Generation Partnership Project (3GPP), TR 37.885, Sep. 2018, version 15.1.0. [Online]. Available: http://www.3gpp.org/DynaReport/37885.htm

[137] M. Padgett, "Here's how the 2019 audi a8 will become the first level 3 self-driving car*," Jul 2017. [Online]. Available: https://www.motorauthority.com/news/1111528_heres-how-the-2019-audi-a8-will-become-the-first-level-3-self-driving-car

[138] "INRAS Radarbook," http://www.inras.at/en/products/radarbook.html.

[139] P. P. Vaidyanathan and P. Pal, "Sparse sensing with co-prime samplers and arrays," *IEEE Trans. Signal Process.*, vol. 59, no. 2, pp. 573–586, 2010.

[140] S. Suleymanov, "Design and Implementation of an FMCW Radar Signal Processing Module for Automotive Applications," Master's thesis, University of Twente, 2016.

[141] J. Hinz and U. Zölzer, "A MIMO FMCW radar approach to HFSWR," *Adv. Radio Sci.*, vol. 9, no. C. 4-2, pp. 159–163, 2011.

[142] V. Katkovnik, M.-S. Lee, and Y.-H. Kim, "High-resolution signal processing for a switch antenna array FMCW radar with a single channel receiver," in *Proc. IEEE Sensor Array Multichannel Signal Process. Wksp*, 2002, pp. 543–547.

[143] S. J. Orfanidis, *Electromagnetic waves and antennas*, 2016. [Online]. Available: http://eceweb1.rutgers.edu/~orfanidi/ewa/

[144] Y.-C. Liang and F. P. Chin, "Downlink channel covariance matrix (DCCM) estimation and its applications in wireless DS-CDMA sys-

tems," *IEEE J. Sel. Areas Commun.*, vol. 19, no. 2, pp. 222–232, Feb. 2001.

[145] M. B. Khalilsarai, S. Haghighatshoar, X. Yi, and G. Caire, "FDD Massive MIMO via UL/DL Channel Covariance Extrapolation and Active Channel Sparsification," *IEEE Trans. Commun.*, vol. 18, no. 1, pp. 121–135, 2018.

[146] "Wireless Insite," http://www.remcom.com/wireless-insite.

[147] I. T. U. (ITU), "Effects of building materials and structures on radiowave propagation above about 100 MHz," Tech. Rep. ITU-R P.2040-1, Jul. 2015.

[148] E. S. Li and K. Sarabandi, "Low grazing incidence millimeter-wave scattering models and measurements for various road surfaces," *IEEE Trans. Antennas Propag.*, vol. 47, no. 5, pp. 851–861, 1999.

[149] Remcom, "5G mmWave Channel Modeling with Diffuse Scattering in an Office Environment."

[150] J. Pascual-García, J.-M. Molina-García-Pardo, M.-T. Martínez-Inglés, J.-V. Rodríguez, and N. Saurín-Serrano, "On the importance of diffuse scattering model parameterization in indoor wireless channels at mm-wave frequencies," *IEEE Access*, vol. 4, pp. 688–701, 2016.

[151] J. Lofberg, "YALMIP: A toolbox for modeling and optimization in MATLAB," in *Proc. IEEE Int. Conf. Robot. Autom.*, 2004, pp. 284–289.

[152] A. Mosek, "The MOSEK optimization toolbox for MATLAB," 2019, release 9.0.94.

[153] S. Hur, S. Baek, B. Kim, Y. Chang, A. F. Molisch, T. S. Rappaport, K. Haneda, and J. Park, "Proposal on millimeter-wave channel modeling for 5G cellular system," *IEEE J. Sel. Areas Commun.*, vol. 10, no. 3, pp. 454–469, 2016.

[154] 3GPP, "Study on channel model for frequencies from 0.5 to 100 GHz," 3rd Generation Partnership Project (3GPP), TR 38.901, Dec. 2017, version 14.3.0. [Online]. Available: http://www.3gpp.org/DynaReport/38901.htm

[155] J. Mo, P. Schniter, and R. W. Heath, "Channel estimation in broadband millimeter wave MIMO systems with few-bit ADCs," *IEEE Trans. Signal Process.*, vol. 66, no. 5, pp. 1141–1154, 2017.

[156] F. Jin and S. Cao, "Automotive Radar Interference Mitigation Using Adaptive Noise Canceller," *IEEE Trans. Veh. Technol.*, vol. 68, no. 4, pp. 3747–3754, 2019.

[157] A. Ma, Y. Zhou, C. Rush, D. Baron, and D. Needell, "An approximate message passing framework for side information," *IEEE Trans. Signal Process.*, vol. 67, no. 7, pp. 1875–1888, 2019.

Vita

Anum Ali received the B.S. degree in electrical engineering from the COMSATS Institute of Information Technology (CIIT), Islamabad, Pakistan, in 2011, and the M.S. degree in electrical engineering from the King Fahd University of Petroleum and Minerals, Dhahran, Saudi Arabia, in 2014. He is currently pursuing the Ph.D. degree in electrical engineering with the Wireless Networking and Communication Group, Department of Electrical and Computer Engineering, The University of Texas at Austin, Austin, TX, USA. From 2011 to 2012 and 2014 to 2015, he held research positions with CIIT and King Abdullah University of Science and Technology, Thuwal, Saudi Arabia, respectively. He has held visiting positions with the California Institute of Technology, Pasadena, CA, USA, in 2015, and Aalborg University, Aalborg, Denmark, in 2017. In 2016, 2017 and 2018, he held internship positions with Intel Corporation, Santa Clara, CA, USA, Qualcomm, Bridgewater, NJ, USA, and Nokia Bell Labs, Naperville, IL, USA. He received the Institute Gold Medal Award from CIIT, Islamabad, Pakistan, for his B.S. degree.

Email address: anumali@utexas.edu

This dissertation was typeset with LaTeX[†] by the author.

[†]LaTeX is a document preparation system developed by Leslie Lamport as a special version of Donald Knuth's TeX Program.